Azerbaijan Journal of Physics

Fizika

www.physics.gov.az

Azerbaijan Journal of Physics

FIZIKA
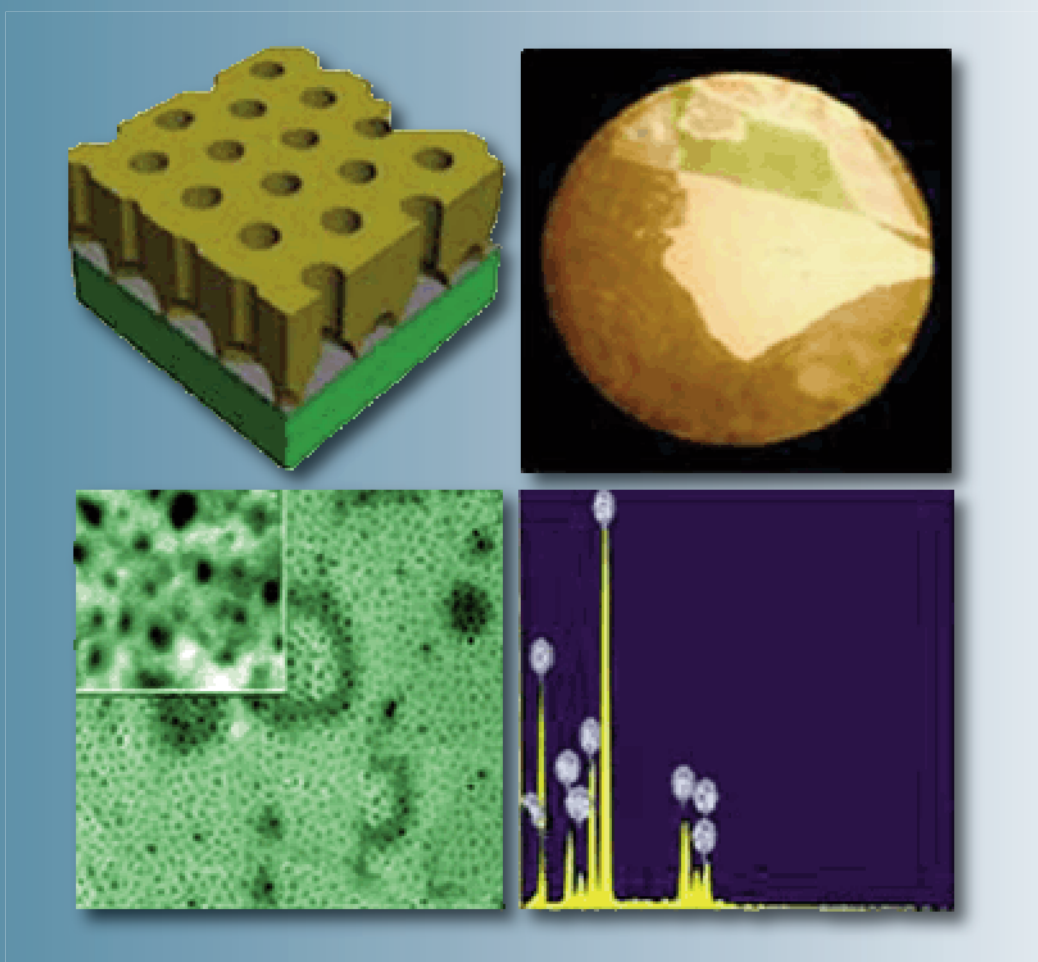
G.M.Abdullayev Institute of Physics
Azerbaijan National Academy of Sciences
Department of Physical, Mathematical and Technical Sciences

MATHEMATICA IN INTEGRATION OF SL(3,C) SELF-DUALITY EQUATIONS

M.A. MUKHTAROV

Institute of Mathematics and Mechanics
370602, Baku, F.Agaev str. 9, Azerbaijan

New solutions of the Yang-Mill's self-duality equation are constructed by means of discrete symmetry transformations and MATHEMATICA software for the algebra SL(3,C). The obtained solutions are expressed in terms of determinants of special type matrixes.

1. Over the last few years self-dual Yang-Mills equation has attracted a fair amount or attention. It has been shown [1-8] that a large number of one, two and (1+2)-dimensional integrable models such as Korteweg-de Vries, N-waves, Ernst, Kadomtsev-Petviashvili, Toda lattice, nonlinear Schrodinger equations and many others can be obtained from the four-dimensional self-dual Yang-Mills equation by symmetry reduction and by imposing the constraints on Yang-Mills potentials.

The universality of the self-dual Yang-Mills (SDYM) model as an integrable system has been confirmed in the paper [9] where the general scheme of the reduction of the Belavin-Zakharov Lax pair for self-duality [10] has been represented over an arbitrary subgroup from the conformal group of transformations of R_4-space. As the result of this reduction one has the Lax pair representation for the corresponding differential equations of a lower dimension.

The problem of constructing of the instanton solutions in the explicit form for semisimple Lie algebra, rank of which is greater than two, remains also important for the present time.

The effective group-theoretical methods have been developed by the author together with Prof. A.N. Leznov of construction of the exact solutions of the Yang-Mill's self-duality equations.

The algebraic perturbation method, known in the scientific literature as Leznov-Mukhtarov method, the Riemann problem method and a method of discrete transformations have allowed to obtain for the first time new classes of exact decisions of self-duality equations of for an arbitrary semisimple algebras [11-17].

2. In section we present the discrete symmetry transformation method of solution the self-duality equation.

Self-dual equations are the systems of equations for the parameters of a group element G considering as the functions of four independent arguments $z, \overline{z}, y, \overline{y}$.

$$\left(G_{\overline{z}}G^{-1}\right)_z + \left(G_{\overline{y}}G^{-1}\right)_y = 0 \quad , \qquad (2.1)$$

where $G_t = \partial_t G$.

The system of equations (2.1) can be partially solved

$$G_{\overline{z}}G^{-1} = +f_y \quad , \quad G_{\overline{y}}G^{-1} = -f_z \quad ,$$

where the element f takes values in the algebra of corresponding group.

System of equations on f has the following form

$$f_{z\overline{z}} + f_{y\overline{y}} + [f_z, f_y] = 0 \qquad (2.2)$$

Following [12], for the case of a semisimple Lie algebra and for an element f being a solution of (2.2), the following statement takes place:

There exists such an element S taking values in a gauge group that

$$S^{-1}\frac{\partial S}{\partial y} = \frac{1}{\tilde{f}_-}\left[\frac{\partial \tilde{f}}{\partial y}, X_M\right] - \frac{\partial}{\partial \overline{z}}\frac{1}{\tilde{f}_-}X_M$$

$$(2.3)$$

$$S^{-1}\frac{\partial S}{\partial z} = \frac{1}{\tilde{f}_-}\left[\frac{\partial \tilde{f}}{\partial z}, X_M\right] + \frac{\partial}{\partial \overline{y}}\frac{1}{\tilde{f}_-}X_M$$

Here X_N is the element of the algebra corresponding to its maximal root divided by its norm, i.e.,

$$\left[X_M^+, X^-\right] = H, \left[H, X^\pm\right] = \pm 2X^\pm \quad ,$$

$-\tilde{f}_-$ - is the coefficient function in the decomposition of $\tilde{f}$ of the element corresponding to the minimal root of the algebra, $\tilde{f} = \sigma f \sigma^{-1}$ and where σ is an automorfism of the algebra, changing the positive and negative roots.

In the case of algebra SL(3,C) we'll consider the case of three dimensional representation of algebra and the following form of $\sigma = \begin{pmatrix} 0 & 0 & 1 \\ 0 & 1 & 0 \\ -1 & 0 & 0 \end{pmatrix}$.

The discrete symmetry transformation, producing new solutions from the known ones, is as follows:

$$\frac{\partial F}{\partial y} = S\frac{\partial \tilde{f}}{\partial y}S^{-1} + \frac{\partial S}{\partial \overline{z}}S^{-1} \quad , \frac{\partial F}{\partial z} = S\frac{\partial \tilde{f}}{\partial z}S^{-1} - \frac{\partial S}{\partial \overline{y}}S^{-1} \qquad (2.4)$$

3. Let's represent the explicit formulae for transformation of the self-duality equations in the case of SL(3,C) algebra

$$f = \alpha_1 X_1^+ + \alpha_2 X_2^+ + \alpha_{1,2} X_{1,2}^+ + \tau_1 h_1 + \tau_2 h_2 + a_1 X_1^- + a_2 X_2^- + a_{1,2} X_{1,2}^- , \qquad (3.1)$$

In connection with the general scheme, first of all, it is necessary to find the solution of the equations (2.4) for the SL(3,C) valued function S for given f, solution of self-duality equation (2.2).

From (2.3) it is clear that S is upper triangular matrix and can be represented in the following form:

$$S = exp\, \beta_1 X_1^+ \, exp\, \beta_{1,2} X_{1,2}^+ \, exp\, \beta_2 X_2^+ \, exp\, \beta_0 H , \qquad (3.2)$$

where $H = h_1 + h_2$.

After substitution of the last representation of S into (2.4) , we have at every step of the recurrent procedure the following relations

$$\beta_0 = ln\, \alpha_{1,2} , \quad \beta_1 = \alpha_2 , \quad \beta_2 = \alpha_1$$
$$(\beta_{1,2})_y = (\alpha_{1,2})_{\bar{z}} - (\delta_1 + \delta_2)_y \alpha_{1,2} - (\alpha_1)_y \alpha_2 \qquad (3.3)$$
$$(\beta_{1,2})_z = -(\alpha_{1,2})_{\bar{y}} - (\delta_1 + \delta_2)_z \alpha_{1,2} - (\alpha_1)_z \alpha_2$$

As the initial solution we'll take the explicit solution f belonging to the algebra of upper triangular matrixes:

$$f = \alpha_1 X_1^+ + \alpha_2 X_2^+ + \alpha_{1,2} X_{1,2}^+ + \tau_1 h_1 + \tau_2 h_2 \qquad (3.4)$$

The component form of self-duality equations for this case is following

$$\Box \tau_i = 0 , \Box \alpha_i = \{\delta_i, \alpha_i\}_{y,z} \quad , \quad i=1,2,$$
$$\Box \alpha_{1,2} = \{\delta_1 + \delta_2, \alpha_{1,2}\}_{y,z} , \qquad (3.5)$$

where $\Box = \dfrac{\partial^2}{\partial z \partial \bar{z}} + \dfrac{\partial^2}{\partial y \partial \bar{y}} ; \delta_1 = 2\tau_1 - \tau_2 , \delta_2 = 2\tau_2 - \tau_1$ and figure brackets of two functions g_1 and g_2 denotes :

$$\{g_1, g_2\}_{y,z} = \frac{\partial g_1}{\partial y} \frac{\partial g_2}{\partial z} - \frac{\partial g_2}{\partial y} \frac{\partial g_1}{\partial z} .$$

The general solution of system (3.5) takes the form

$$\tau_i = \oint_c \tau_i(\lambda) d\lambda \quad , \quad \alpha_i = \oint_c \alpha_i(\lambda) exp\,(-\bar{\delta}_i(\lambda)) d\lambda ,$$

$$\bar{\delta}_i(\lambda) = \oint_c \frac{d\lambda' \delta_i(\lambda')) d\lambda'}{\lambda - \lambda'} \quad , \quad i = 1,2 \quad ,$$

$$\alpha_{1,2} = \oint_c \alpha_{1,2}(\lambda) exp\,(-\bar{\delta}_1(\lambda) - \bar{\delta}_2(\lambda)) d\lambda + \oint_c \alpha_1(\lambda) exp\,(-\delta_1(\lambda)) d\lambda \oint_c \frac{d\lambda' \alpha_2(\lambda') exp\,(-\delta_2(\lambda'))}{\lambda - \lambda'} \quad (3.6)$$

Here the circle integration goes over the complex parameter λ and all integrated functions are arbitrary functions of three independent variables $(y + \lambda \bar{z}, z - \lambda \bar{y}, \lambda)$.

By the direct check one can be convinced that (3.6) are the solutions of equations (3.5).

Let's represent two types of Backlund transformation by means of which one can construct new types of solutions of equations (3.5) from the known solution (3.6). For solutions of first two equations of (3.5) this two Backlund transformations are the same:

$$(\alpha_i^k)_{\bar{z}} - (\delta_i)_y \alpha_i^k = (\alpha_i^{k+1})_y$$
$$- (\alpha_i^k)_{\bar{y}} - (\delta_i)_z \alpha_i^k = (\alpha_i^{k+1})_z \quad , i = 1,2 \qquad (3.7)$$

For solutions of the third equation of the system (3.5) they are different:

$$(\alpha_{1,2}^{0,k})_{\bar{z}} - (\delta_1 + \delta_2)_y \alpha_{1,2}^{0,k} - (\alpha_1^k)_y \alpha_2^k = (\alpha_{1,2}^{0,k+1})_y$$

$$- (\alpha_{1,2}^{0,k})_{\bar{y}} - (\delta_1 + \delta_2)_z \alpha_{1,2}^{0,k} - (\alpha_1^k)_z \alpha_2^k = (\alpha_{1,2}^{0,k+1})_z \tag{3.8}$$

and

$$(\alpha_{1,2}^{k,0})_{\bar{z}} - (\delta_1 + \delta_2)_y \alpha_{1,2}^{k,0} + \alpha_1^k (\alpha_2^k)_y = (\alpha_{1,2}^{k+1,0})_y$$

$$- (\alpha_{1,2}^{k,0})_{\bar{y}} - (\delta_1 + \delta_2)_z \alpha_{1,2}^{k,0} + \alpha_1^k (\alpha_2^k)_z = (\alpha_{1,2}^{k+1,0})_z \tag{3.9}$$

Note that starting, zero step of upper transformations procedure coincides with initial solutions (3.6).
Let's return to the solution of the equation (3.3) at the first step of the recurrent procedure.

Comparing (3.3) and (3.9) we came to the conclusion that $\beta_{1,2} = \alpha_{1,2}^{0,1}$.

Finally, knowing all components of matrix S and using (3.9) we can express the solution

$$F = F_1^+ X_1^+ + F_2^+ X_2^+ + F_{1,2}^+ X_{1,2}^+ + F_1^0 h_1 + F_2^0 h_2 + F_1^- X_1^- + F_2^- X_2^- + F_{1,2}^- X_{1,2}^-$$

of self-duality equations at the first step of the recurrent procedure in terms of chains (3.7)-(3.9):

$$F_1^0 = \tau_1 + \frac{\alpha_{1,2}^{1,0}}{\alpha_{1,2}^{0,0}} , \quad F_2^0 = \tau_2 + \frac{\alpha_{1,2}^{0,1}}{\alpha_{1,2}^{0,0}}$$

$$F_{1,2}^- = \frac{1}{\alpha_{1,2}^{0,0}} , \quad F_1^- = \frac{\alpha_2^0}{\alpha_{1,2}^{0,0}} , \quad F_2^- = -\frac{\alpha_1^0}{\alpha_{1,2}^{0,0}}$$

$$F_1^+ = -\frac{1}{\alpha_{1,2}^{0,0}} \begin{vmatrix} \alpha_1^0 & \alpha_1^1 \\ \alpha_{1,2}^{0,0} & \alpha_{1,2}^{1,0} \end{vmatrix} , \quad F_2^+ = -\frac{1}{\alpha_{1,2}^{0,0}} \begin{vmatrix} \alpha_2^0 & \alpha_2^1 \\ \alpha_{1,2}^{0,0} & \alpha_{1,2}^{0,1} \end{vmatrix}$$

$$F_{1,2}^+ = \frac{1}{\alpha_{1,2}^{0,0}} \begin{vmatrix} \alpha_{1,2}^{0,0} & \alpha_{1,2}^{0,1} \\ \alpha_{1,2}^{1,0} & \alpha_{1,2}^{1,1} \end{vmatrix}$$

Using the self-duality equations of the for the group-valued element

$$G_{\bar{z}} G^{-1} = +f_y , \quad G_{\bar{y}} G^{-1} = -f_z$$

the relations can be rewritten as

$$\theta_i (S_n \sigma g_n)_{x_i} (S_n \sigma g_n)^{-1} = (f_{n+1})_{x_i} ,$$

So we see that the group valued elements g_{n+1} and g_n are connected by the relation

$$g_{n+1} = S_n \sigma g_n \tag{3.10}$$

Let's represent the explicit formulae of the recurrent procedure of obtaining the group-valued element solutions.
At every step, as it shown in [5], S is upper triangular matrix and can be represented in the following form:

$$S_n = exp(\beta_1)_n X_1^+ exp(\beta_{1,2})_n X_{1,2}^+ exp(\beta_2)_n X_2^+ exp(\beta_0)_n H \tag{3.11}$$

where $H = h_1 + h_2$ and for g_n we use the following parameterization:

$$g_n = exp(\eta_1^+)_n X_1^+ exp(\eta_{1,2}^+)_n X_{1,2}^+ exp(\eta_2^+)_n X_2^+ exp((t_1)_n h_1 + (t_2)_n h_2) \times$$

$$\times exp(\eta_2^-)_n X_2^- exp(\eta_{1,2}^-)_n X_{1,2}^- exp(\eta_1^-)_n X_1^- \tag{3.12}$$

with

$$g_0 = exp(\eta_1^+)_0 X_1^+ exp(\eta_{1,2}^+)_0 X_{1,2}^+ exp(\eta_2^+)_0 X_2^+ exp((t_1)_0 h_1 + (t_2)_0 h_2)$$

as an initial solution.

Hereafter, $X_1^\pm$, $X_2^\pm$, $X_{1,2}^\pm$, h_1, h_2 are the generators of SL(3,C) algebra.

Following the general scheme from [5] we have at
(0)-step:

$$(t_i)_0 = \tau_i^{-1} \equiv v_i , (\eta_i^+)_0 = \alpha_i^{-1}, i = 1,2 , (\eta_{1,2}^+)_0 = \alpha_{1,2}^{-1,0} \quad ;$$

The further calculation we deliver to Mathematica program:

$$X_1^+ = \begin{pmatrix} 0 & 1 & 0 \\ 0 & 0 & 0 \\ 0 & 0 & 0 \end{pmatrix}; \quad X_2^+ = \begin{pmatrix} 0 & 0 & 0 \\ 0 & 0 & 1 \\ 0 & 0 & 0 \end{pmatrix}; \quad X_{1,2}^+ = \begin{pmatrix} 0 & 0 & 1 \\ 0 & 0 & 0 \\ 0 & 0 & 0 \end{pmatrix};$$

$$X_1^- = \begin{pmatrix} 0 & 0 & 0 \\ 1 & 0 & 0 \\ 0 & 0 & 0 \end{pmatrix}; \quad X_2^- = \begin{pmatrix} 0 & 0 & 0 \\ 0 & 0 & 0 \\ 0 & 1 & 0 \end{pmatrix}; \quad X_{1,2}^- = \begin{pmatrix} 0 & 0 & 0 \\ 0 & 0 & 0 \\ 1 & 0 & 0 \end{pmatrix};$$

$$h_1 = \begin{pmatrix} 1 & 0 & 0 \\ 0 & -1 & 0 \\ 0 & 0 & 0 \end{pmatrix}; \quad h_2 = \begin{pmatrix} 0 & 0 & 0 \\ 0 & 1 & 0 \\ 0 & 0 & -1 \end{pmatrix}; \quad w = \begin{pmatrix} 0 & 0 & 1 \\ 0 & 1 & 0 \\ -1 & 0 & 0 \end{pmatrix};$$

$G_0 = \text{MatrixExp}[n_1\, X_1^+].\text{MatrixExp}[n_{1,2}\, X_{1,2}^+].\text{MatrixExp}[n_2\, X_2^+].\text{MatrixExp}[r_1\, h_1].$
  $\text{MatrixExp}[r_2\, h_2];$

$S_1 = \text{MatrixExp}[b_1\, X_1^+].\text{MatrixExp}[b_{1,2}\, X_{1,2}^+].\text{MatrixExp}[b_2\, X_2^+].\text{MatrixExp}[b_0\, (h_1 + h_2)];$

$G_1 = S_1.w.G_0;$

$\text{MatrixForm}[G_1]$

$$\text{Null}^4 \begin{pmatrix} -e^{-b_0+r_1}(b_1 b_2 + b_{1,2}) & e^{-r_1+r_2}b_1 - e^{-b_0-r_1+r_2}n_1(b_1 b_2+b_{1,2}) & e^{b_0-r_2}+e^{-r_2}b_1 n_2 - e^{-b_0-r_2}(b_1 b_2+b_{1,2})(n_1 n_2+n_{1,2}) \\ -e^{-b_0+r_1}b_2 & e^{-r_1+r_2}-e^{-b_0-r_1+r_2}b_2 n_1 & e^{-r_2}n_2-e^{-b_0-r_2}b_2(n_1 n_2+n_{1,2}) \\ -e^{-b_0+r_1} & -e^{-b_0-r_1+r_2}n_1 & -e^{-b_0-r_2}(n_1 n_2+n_{1,2}) \end{pmatrix}$$

$G_1 /. (b_1 b_2 + b_{1,2}) \to a_{1,2}[1,0] /. n_1 n_2 + n_{1,2} \to a_{1,2}[0,-1] /. b_0 \to \text{Log}[a_{1,2}[0,0]] /.$
  $b_1 \to a_1[0]$
  $/. b_2 \to a_2[0] /. n_1 \to a_1[-1] /. n_2 \to a_2[-1]$

$$\left\{\left\{-e^{-\text{Log}[a_{1,2}[0,0]]+r_1}a_{1,2}[1,0], e^{-r_1+r_2}a_1[0]-e^{-\text{Log}[a_{1,2}[0,0]]-r_1+r_2}a_1[-1]a_{1,2}[1,0],\right.\right.$$
$$e^{\text{Log}[a_{1,2}[0,0]]-r_2}+e^{-r_2}a_1[0]a_2[-1]-e^{-\text{Log}[a_{1,2}[0,0]]-r_2}a_{1,2}[0,-1]a_{1,2}[1,0]\},$$
$$\left\{-e^{-\text{Log}[a_{1,2}[0,0]]+r_1}a_2[0], e^{-r_1+r_2}-e^{-\text{Log}[a_{1,2}[0,0]]-r_1+r_2}a_1[-1]a_2[0],\right.$$
$$e^{-r_2}a_2[-1]-e^{-\text{Log}[a_{1,2}[0,0]]-r_2}a_2[0]a_{1,2}[0,-1]\},$$
$$\left\{-e^{-\text{Log}[a_{1,2}[0,0]]+r_1}, -e^{-\text{Log}[a_{1,2}[0,0]]-r_1+r_2}a_1[-1], -e^{-\text{Log}[a_{1,2}[0,0]]-r_2}a_{1,2}[0,-1]\right\}\right\}$$

$G_1 = \text{FullSimplify}[\%]$

6

$$\left\{\left\{-\frac{e^{r_1}\,a_{1,2}[1,0]}{a_{1,2}[0,0]},\; \frac{e^{-r_1+r_2}\,(a_1[0]\,a_{1,2}[0,0]-a_1[-1]\,a_{1,2}[1,0])}{a_{1,2}[0,0]},\right.\right.$$

$$\left.\frac{e^{-r_2}\,(a_1[0]\,a_2[-1]\,a_{1,2}[0,0]+a_{1,2}[0,0]^2-a_{1,2}[0,-1]\,a_{1,2}[1,0])}{a_{1,2}[0,0]}\right\},\left\{-\frac{e^{r_1}\,a_2[0]}{a_{1,2}[0,0]},\right.$$

$$\left.\frac{e^{-r_1+r_2}\,(-a_1[-1]\,a_2[0]+a_{1,2}[0,0])}{a_{1,2}[0,0]},\; \frac{e^{-r_2}\,(-a_2[0]\,a_{1,2}[0,-1]+a_2[-1]\,a_{1,2}[0,0])}{a_{1,2}[0,0]}\right\},$$

$$\left.\left\{-\frac{e^{r_1}}{a_{1,2}[0,0]},\; -\frac{e^{-r_1+r_2}\,a_1[-1]}{a_{1,2}[0,0]},\; -\frac{e^{-r_2}\,a_{1,2}[0,-1]}{a_{1,2}[0,0]}\right\}\right\}$$

.

$$G_1 = \text{FullSimplify}\big[\% \,/.\, a_1[0]\,a_2[-1] \rightarrow a_{1,2}[1,-1]-a_{1,2}[0,0]$$

$$/.\, a_1[-1]\,a_2[0] \rightarrow a_{1,2}[0,0]-a_{1,2}[-1,1]\big]$$

$$\left\{\left\{-\frac{e^{r_1}\,a_{1,2}[1,0]}{a_{1,2}[0,0]},\; \frac{e^{-r_1+r_2}\,(a_1[0]\,a_{1,2}[0,0]-a_1[-1]\,a_{1,2}[1,0])}{a_{1,2}[0,0]},\right.\right.$$

$$\left.\frac{e^{-r_2}\,(a_{1,2}[0,0]\,a_{1,2}[1,-1]-a_{1,2}[0,-1]\,a_{1,2}[1,0])}{a_{1,2}[0,0]}\right\},$$

$$\left\{-\frac{e^{r_1}\,a_2[0]}{a_{1,2}[0,0]},\; \frac{e^{-r_1+r_2}\,a_{1,2}[-1,1]}{a_{1,2}[0,0]},\; \frac{e^{-r_2}\,(-a_2[0]\,a_{1,2}[0,-1]+a_2[-1]\,a_{1,2}[0,0])}{a_{1,2}[0,0]}\right\},$$

$$\left.\left\{-\frac{e^{r_1}}{a_{1,2}[0,0]},\; -\frac{e^{-r_1+r_2}\,a_1[-1]}{a_{1,2}[0,0]},\; -\frac{e^{-r_2}\,a_{1,2}[0,-1]}{a_{1,2}[0,0]}\right\}\right\}$$

$$T_2[1] = G_1[[3,3]];$$

$$T_1[1] = \text{Mnors}[G_1][[3,3]];$$

$$\alpha_2[1] = G_1[[2,3]]/T_2[1];$$

$$\beta_2[1] = G_1[[3,2]]/T_2[1];$$

$$\beta_1[1] = \text{Mnors}[G_1][[3,2]]/T_1[1];$$

$$\alpha_1[1] = \text{Mnors}[G_1][[2,3]]/T_1[1];$$

$$\alpha_{1,2}[1] = -\text{Mnors}[G_1][[1,3]]/T_1[1];$$

$$\beta_{1,2}[1] = -\text{Mnors}[G_1][[3,1]]/T_1[1];$$

$$\text{FullSimplify}[T_2[1]]$$

$$-\frac{e^{-r_2}\,a_{1,2}[0,-1]}{a_{1,2}[0,0]}$$

7

FullSimplify[T₁[1]]

$$\frac{e^{-r_1}\left(-\left(a_1[-1]\,a_2[0]+a_{1,2}[-1,1]\right)a_{1,2}[0,-1]+a_1[-1]\,a_2[-1]\,a_{1,2}[0,0]\right)}{a_{1,2}[0,0]^2}$$

T₁[1] = FullSimplify[% /. a₁[-1] a₂[0] → a_{1,2}[0, 0] - a_{1,2}[-1, 1]
       /. a₁[-1] a₂[-1] → a_{1,2}[0, -1] - a_{1,2}[-1, 0]]

$$-\frac{e^{-r_1}\,a_{1,2}[-1,0]}{a_{1,2}[0,0]}$$

FullSimplify[β_1[1]]

$$\frac{e^{2\,r_1-r_2}\,a_2[-1]\,a_{1,2}[0,0]}{-\left(a_1[-1]\,a_2[0]+a_{1,2}[-1,1]\right)a_{1,2}[0,-1]+a_1[-1]\,a_2[-1]\,a_{1,2}[0,0]}$$

β_1[1] = FullSimplify[% /. a₁[-1] a₂[0] → a_{1,2}[0, 0] - a_{1,2}[-1, 1]
       /. a₁[-1] a₂[-1] → a_{1,2}[0, -1] - a_{1,2}[-1, 0]]

$$-\frac{e^{2\,r_1-r_2}\,a_2[-1]}{a_{1,2}[-1,0]}$$

FullSimplify[$\beta_{1,2}$[1]]

$$\frac{e^{r_1+r_2}\left(a_1[-1]\,a_2[0]+a_{1,2}[-1,1]\right)}{\left(a_1[-1]\,a_2[0]+a_{1,2}[-1,1]\right)a_{1,2}[0,-1]-a_1[-1]\,a_2[-1]\,a_{1,2}[0,0]}$$

$\beta_{1,2}$[1] = FullSimplify[% /. a₁[-1] a₂[0] → a_{1,2}[0, 0] - a_{1,2}[-1, 1]
       /. a₁[-1] a₂[-1] → a_{1,2}[0, -1] - a_{1,2}[-1, 0]]

$$\frac{e^{r_1+r_2}}{a_{1,2}[-1,0]}$$

FullSimplify[β_2[1]]

$$\frac{e^{-r_1+2\,r_2}\,a_1[-1]}{a_{1,2}[0,-1]}$$

FullSimplify[α_1[1]]

$$\frac{a_{1,2}[0,0]\left(-a_1[0]\,a_{1,2}[0,-1]+a_1[-1]\,a_{1,2}[1,-1]\right)}{-\left(a_1[-1]\,a_2[0]+a_{1,2}[-1,1]\right)a_{1,2}[0,-1]+a_1[-1]\,a_2[-1]\,a_{1,2}[0,0]}$$

$\alpha_1[1] = \text{FullSimplify}[\% \,/.\, a_1[-1]\,a_2[0] \to a_{1,2}[0,0]-a_{1,2}[-1,1]$

$\quad /.\, a_1[-1]\,a_2[-1] \to a_{1,2}[0,-1]-a_{1,2}[-1,0]]$

$$\frac{a_1[0]\,a_{1,2}[0,-1]-a_1[-1]\,a_{1,2}[1,-1]}{a_{1,2}[-1,0]}$$

$\text{FullSimplify}[\alpha_2[1]]$

$$a_2[0] - \frac{a_2[-1]\,a_{1,2}[0,0]}{a_{1,2}[0,-1]}$$

$\text{FullSimplify}[\alpha_{1,2}[1]]$

$$\frac{a_{1,2}[0,0]\left(a_1[0]\left(a_2[0]\,a_{1,2}[0,-1]-a_2[-1]\,a_{1,2}[0,0]\right)+a_{1,2}[-1,1]\,a_{1,2}[1,-1]\right)}{-\left(a_1[-1]\,a_2[0]+a_{1,2}[-1,1]\right)a_{1,2}[0,-1]+a_1[-1]\,a_2[-1]\,a_{1,2}[0,0]}+a_{1,2}[1,0]$$

$\alpha_{1,2}[1] = \text{FullSimplify}[\% \,/.\, a_1[-1]\,a_2[0] \to a_{1,2}[0,0]-a_{1,2}[-1,1]$

$\quad /.\, a_1[-1]\,a_2[-1] \to a_{1,2}[0,-1]-a_{1,2}[-1,0]]$

$$\frac{a_1[0]\left(-a_2[0]\,a_{1,2}[0,-1]+a_2[-1]\,a_{1,2}[0,0]\right)-a_{1,2}[-1,1]\,a_{1,2}[1,-1]}{a_{1,2}[-1,0]}+a_{1,2}[1,0]$$

$\text{Expand}[\%]$

$$-\frac{a_1[0]\,a_2[0]\,a_{1,2}[0,-1]}{a_{1,2}[-1,0]}+\frac{a_1[0]\,a_2[-1]\,a_{1,2}[0,0]}{a_{1,2}[-1,0]}-\frac{a_{1,2}[-1,1]\,a_{1,2}[1,-1]}{a_{1,2}[-1,0]}+a_{1,2}[1,0]$$

$\alpha_{1,2}[1] = \text{FullSimplify}[\% \,/.\, a_{1,2}[1,0] \to a_1[0]\,a_2[0]+a_{1,2}[0,1] \,/.$

$\quad /.\, a_{1,2}[1,-1] \to a_1[0]\,a_2[-1]+a_{1,2}[0,0] \,/.\, a_{1,2}[0,-1] \to a_1[-1]\,a_2[-1]+a_{1,2}[-1,0]]$

$$\frac{1}{a_{1,2}[-1,0]}\left(-a_1[0]\,a_2[-1]\left(a_1[-1]\,a_2[0]+a_{1,2}[-1,1]\right)+\right.$$

$$\left(a_1[0]\,a_2[-1]-a_{1,2}[-1,1]\right)a_{1,2}[0,0]+a_{1,2}[-1,0]\,a_{1,2}[0,1]\right)$$

$\alpha_{1,2}[1] = \text{FullSimplify}[\% \,/.\, a_1[-1]\,a_2[0] \to a_{1,2}[0,0]-a_{1,2}[-1,1]]$

$$-\frac{a_{1,2}[-1,1]\,a_{1,2}[0,0]}{a_{1,2}[-1,0]}+a_{1,2}[0,1]$$

The second step.

$$B_1 = \frac{-a_1[0]\, a_{1,2}[1,0] + a_1[1]\, a_{1,2}[0,0]}{a_{1,2}[0,0]}; \quad B_2 = \frac{-a_2[0]\, a_{1,2}[0,1] + a_2[1]\, a_{1,2}[0,0]}{a_{1,2}[0,0]};$$

$$B_0 = \text{Log}\left[\frac{-a_{1,2}[1,1]\, a_{1,2}[0,0] + a_{1,2}[1,0]\, a_{1,2}[0,1]}{a_{1,2}[0,0]}\right];$$

$$B_{1,2} = \frac{1}{(a_{1,2}[0,0])^{\wedge}2}\, a_{1,2}[0,0]\,(a_{1,2}[1,2]\, a_{1,2}[0,0] - a_{1,2}[1,1]\, a_{1,2}[0,1])\, a_{1,2}[0,1]$$

$$(a_{1,2}[1,1]\, a_{1,2}[0,0] - a_{1,2}[1,0]\, a_{1,2}[0,1]);$$

$$S_2 = \text{MatrixExp}[B_1\, X_1^{\dagger}]\,\text{MatrixExp}[B_{1,2}\, X_{1,2}^{\dagger}]\,\text{MatrixExp}[B_2\, X_2^{\dagger}]\,\text{MatrixExp}[B_0\,(h_1 + h_2)];$$

$$G_2 = S_2.w.G_1;\ T_2[2] = G_2[[3,3]];\ T_1[2] = \text{Mnors}[G_2][[3,3]];$$

$$\alpha_2[2] = G_2[[2,3]]/T_2[2];\ \beta_2[2] = G_2[[3,2]]/T_2[2];\ \beta_1[2] = \text{Mnors}[G_2][[3,2]]/T_1[2];$$

$$\alpha_1[2] = \text{Mnors}[G_2][[2,3]]/T_1[2];\ \alpha_{1,2}[2] = -\text{Mnors}[G_2][[1,3]]/T_1[2];$$

$$\beta_{1,2}[2] = -\text{Mnors}[G_2][[3,1]]/T_1[2]\quad \text{FullSimplify}[T_2[2]]$$

$$\frac{e^{-r_2}\,(a_{1,2}[0,0]\, a_{1,2}[1,-1] - a_{1,2}[0,-1]\, a_{1,2}[1,0])}{-a_{1,2}[0,1]\, a_{1,2}[1,0] + a_{1,2}[0,0]\, a_{1,2}[1,1]}$$

FullSimplify[$T_1[2]$]

$$\left(e^{-r_1}\,\big(a_{1,2}[0,0]\,(a_1[0]\,(a_2[0]\, a_{1,2}[0,-1] - a_2[-1]\, a_{1,2}[0,0]) + a_{1,2}[-1,1]\, a_{1,2}[1,-1]) - \right.$$
$$\left.((a_1[-1]\, a_2[0] + a_{1,2}[-1,1])\, a_{1,2}[0,-1] - a_1[-1]\, a_2[-1]\, a_{1,2}[0,0])\, a_{1,2}[1,0])\big)\right/$$
$$\left(a_{1,2}[0,0]\,(-a_{1,2}[0,1]\, a_{1,2}[1,0] + a_{1,2}[0,0]\, a_{1,2}[1,1])\right)$$

$$T_1[1] = \text{FullSimplify}\big[\%44\ /.\ a_{1,2}[1,-1] \rightarrow a_{1,2}[0,0] + a_1[0]\, a_2[-1]$$
$$/.\ a_{1,2}[0,-1] \rightarrow a_{1,2}[-1,0] + a_1[-1]\, a_2[-1]\ /.\ a_1[-1]\, a_2[0] \rightarrow a_{1,2}[0,0] - a_{1,2}[-1,1]\big]$$

$$\left(e^{-r_1}\,\big(a_1[-1]\, a_1[0]\, a_2[-1]\, a_2[0] + a_1[0]\,(a_2[0]\, a_{1,2}[-1,0] + a_2[-1]\,(a_{1,2}[-1,1] - a_{1,2}[0,0])) + \right.$$
$$\left.a_{1,2}[-1,1]\, a_{1,2}[0,0] - a_{1,2}[-1,0]\, a_{1,2}[1,0])\big)\right/\left(-a_{1,2}[0,1]\, a_{1,2}[1,0] + a_{1,2}[0,0]\, a_{1,2}[1,1]\right)$$

$$\text{ch1} = (a_1[-1]\, a_1[0]\, a_2[-1]\, a_2[0] + a_1[0]\,(a_2[0]\, a_{1,2}[-1,0] + a_2[-1]\,(a_{1,2}[-1,1] - a_{1,2}[0,0])) +$$
$$a_{1,2}[-1,1]\, a_{1,2}[0,0] - a_{1,2}[-1,0]\, a_{1,2}[1,0]);$$

$$\text{FullSimplify}[\text{ch1}\ /.\ a_{1,2}[1,0] \rightarrow a_{1,2}[0,1] + a_1[0]\, a_2[0]\ /.\ a_1[-1]\, a_2[0] \rightarrow a_{1,2}[0,0] - a_{1,2}[-1,1]]$$

$$a_{1,2}[-1,1]\, a_{1,2}[0,0] - a_{1,2}[-1,0]\, a_{1,2}[0,1]$$

$T_2[2] =$

$e^{-r_1} (a_{1,2}[-1, 1] \, a_{1,2}[0,0] - a_{1,2}[-1,0] \, a_{1,2}[0, 1]) /$

$\quad (-a_{1,2}[0, 1] \, a_{1,2}[1,0] + a_{1,2}[0, 0] \, a_{1,2}[1,1])$

$$\frac{e^{-r_1} (a_{1,2}[-1, 1] \, a_{1,2}[0, 0] - a_{1,2}[-1, 0] \, a_{1,2}[0, 1])}{-a_{1,2}[0, 1] \, a_{1,2}[1, 0] + a_{1,2}[0, 0] \, a_{1,2}[1, 1]}$$

$\text{FullSimplify}[\beta_1[2]]$

$e^{2 r_1 - r_2} \, a_{1,2}[0, 0] \, (a_2[0] \, a_{1,2}[1, -1] - a_2[-1] \, a_{1,2}[1, 0])) /$

$(a_{1,2}[0, 0] \, (a_1[0] \, (-a_2[0] \, a_{1,2}[0, -1] + a_2[-1] \, a_{1,2}[0, 0]) - a_{1,2}[-1, 1] \, a_{1,2}[1, -1]) +$

$\quad ((a_1[-1] \, a_2[0] + a_{1,2}[-1, 1]) \, a_{1,2}[0, -1] - a_1[-1] \, a_2[-1] \, a_{1,2}[0, 0]) \, a_{1,2}[1, 0])$

$Zn1 = (a_{1,2}[0, 0] \, (a_1[0] \, (-a_2[0] \, a_{1,2}[0, -1] + a_2[-1] \, a_{1,2}[0, 0]) - a_{1,2}[-1, 1] \, a_{1,2}[1, -1]) +$

$\quad ((a_1[-1] \, a_2[0] + a_{1,2}[-1, 1]) \, a_{1,2}[0, -1] - a_1[-1] \, a_2[-1] \, a_{1,2}[0, 0]) \, a_{1,2}[1, 0]);$

$\text{FullSimplify}[$

$\quad Zn1 \, /. \, a_{1,2}[1, -1] \rightarrow a_{1,2}[0, 0] + a_1[0] \, a_2[-1]$

$\qquad /. \, a_{1,2}[0, -1] \rightarrow a_{1,2}[-1, 0] + a_1[-1] \, a_2[-1] \, /. \, a_1[-1] \, a_2[0] \rightarrow a_{1,2}[0, 0] - a_{1,2}[-1, 1] \, /.$

$\quad a_{1,2}[1, 0] \rightarrow a_{1,2}[0, 1] + a_1[0] \, a_2[0]]$

$a_{1,2}[0, 0] \, (-a_1[0] \, a_2[-1] \, (a_1[-1] \, a_2[0] + a_{1,2}[-1, 1]) +$

$\quad (a_1[0] \, a_2[-1] - a_{1,2}[-1, 1]) \, a_{1,2}[0, 0] + a_{1,2}[-1, 0] \, a_{1,2}[0, 1])$

$\text{FullSimplify}[\% \, /. \, a_1[-1] \, a_2[0] \rightarrow a_{1,2}[0, 0] - a_{1,2}[-1, 1]]$

$a_{1,2}[0, 0] \, (-a_{1,2}[-1, 1] \, a_{1,2}[0, 0] + a_{1,2}[-1, 0] \, a_{1,2}[0, 1])$

$\beta_1[2] = e^{2 r_1 - r_2} \, (a_2[0] \, a_{1,2}[1, -1] - a_2[-1] \, a_{1,2}[1, 0]) /$

$\quad (-a_{1,2}[-1, 1] \, a_{1,2}[0, 0] + a_{1,2}[-1, 0] \, a_{1,2}[0, 1]);$

$\text{FullSimplify}[\beta_2[2]]$

$$\frac{e^{-r_1 + 2 r_2} \, (a_1[0] \, a_{1,2}[0, 0] - a_1[-1] \, a_{1,2}[1, 0])}{a_{1,2}[0, 0] \, a_{1,2}[1, -1] - a_{1,2}[0, -1] \, a_{1,2}[1, 0]}$$

$\text{FullSimplify}[\beta_{1,2}[2]]$

11

$$\left(e^{r_1+r_2}\left(a_1[0]\,a_2[0]\,a_{1,2}[0,0] - \left(a_1[-1]\,a_2[0] + a_{1,2}[-1,1]\right)a_{1,2}[1,0]\right)\right)/$$
$$\left(a_{1,2}[0,0]\left(a_1[0]\left(a_2[0]\,a_{1,2}[0,-1] - a_2[-1]\,a_{1,2}[0,0]\right) + a_{1,2}[-1,1]\,a_{1,2}[1,-1]\right) - \right.$$
$$\left.\left(\left(a_1[-1]\,a_2[0] + a_{1,2}[-1,1]\right)a_{1,2}[0,-1] - a_1[-1]\,a_2[-1]\,a_{1,2}[0,0]\right)a_{1,2}[1,0]\right)$$

$$\text{FullSimplify}\!\left[\% \, /.\; a_{1,2}[1,-1] \to a_{1,2}[0,0] + a_1[0]\,a_2[-1]\right.$$
$$/.\; a_{1,2}[0,-1] \to a_{1,2}[-1,0] + a_1[-1]\,a_2[-1]\;/.\; a_{1,2}[1,0] \to a_{1,2}[0,1] + a_1[0]\,a_2[0]$$
$$\left./.\; a_1[-1]\,a_2[0] \to a_{1,2}[0,0] - a_{1,2}[-1,1]\right]$$

$$\left(e^{r_1+r_2}\,a_{1,2}[0,1]\right)/\left(-a_1[0]\,a_2[-1]\left(a_1[-1]\,a_2[0] + a_{1,2}[-1,1]\right) + \right.$$
$$\left.\left(a_1[0]\,a_2[-1] - a_{1,2}[-1,1]\right)a_{1,2}[0,0] + a_{1,2}[-1,0]\,a_{1,2}[0,1]\right)$$

$$\text{FullSimplify}\!\left[\% \, /.\; a_1[-1]\,a_2[0] \to a_{1,2}[0,0] - a_{1,2}[-1,1]\right]$$

$$\frac{e^{r_1+r_2}\,a_{1,2}[0,1]}{-a_{1,2}[-1,1]\,a_{1,2}[0,0] + a_{1,2}[-1,0]\,a_{1,2}[0,1]}$$

$$\beta_{1,2}[2] = \frac{e^{r_1+r_2}\,a_{1,2}[0,1]}{-a_{1,2}[-1,1]\,a_{1,2}[0,0] + a_{1,2}[-1,0]\,a_{1,2}[0,1]}$$

$$\frac{e^{r_1+r_2}\,a_{1,2}[0,1]}{-a_{1,2}[-1,1]\,a_{1,2}[0,0] + a_{1,2}[-1,0]\,a_{1,2}[0,1]}\;|$$

At that point we stop the procedure, but it is obvious that it can easily be continued for any step and the resulting formulas correspond to those from [15].

As it is seen from formulas for algebras of the rank higher than two, the number of corresponding Backlund transformations of the initial problem solutions will be equal to the rank of the algebra. Thus, it is necessary only to overcome the routine calculations using Mathematica 4-0 software.

---

[1] *R.S. Ward, Phil. Trans.* R. Soc. Lond.A315, 451 (1985); Lect. Notes Phys., 1987, 280, 106; Lond. Math. Soc. Lect. Notes Ser., 1990, 156, 246.

[2] *L.J. Mason and G.A. J.Sparling.* Phys. Lett., 1989, A137, 29; J. Geom. and Phys., 1992, 8, 243.

[3] *S. Chakravarty, M.J. Ablowitz and P.A. Clarkson.* Phys. Rev. Lett., 1990, 1085.

[4] *I. Bakas and D.A. Depireux.* Mod. Phys. Lett., 1991, A6, 399.

[5] *M.J. Ablowitz, S. Chakravarty and L.A. Takhtajan.* Comm. Math. Phys., 1993, 158, 1289.

[6] *T.A. Ivanova and A.D. Popov.* Phys. Lett., 1992, A170, 293.

[7] *L.J. Mason and N.M.J. Woodhouse.* Nonlinearity 1, 1988, 73; 1993, 6, 569.

[8] *M. Kovalyov, M. Legare and L. Gagnon.* J. Math. Phys., 1993, 34, 3425.

[9] *M. Legare and A.D. Popov.* Pis'ma Zh. Eksp. Teor. Fiz., 1994, 59, 845.

[10] *A.A. Belavin and V.E. Zakharov.* Phys. Lett., 1978, B73, 53.

[11] *A.N. Leznov and M.A. Mukhtarov.* J. Math. Phys., 1987, 28 (11), 2574; Prepr. IHEP, 1987, 87-90. Prepr. ICTP 163, Trieste, Italy, 1990; J. Sov. Lazer Research, 13 (4), 284, 1992.

[12] *A.N. Leznov.* IHEP preprint-92/87, 1990.

[13] *A.N. Leznov, M.A.Mukhtarov and W.J.Zakrzewski.* Tr. J. of Physics 1995, 19, 416.

HIGH SENSITIVE p-Cd$_x$Hg$_{1-x}$Te (x=0.23-0.3) BASED PHOTOCONDUCTOR WITH SURFACE CONVERSION LAYER

N.J. ISMAYILOV, E.K. HUSEYNOV, A.A. ALIYEV, I.S. HASANOV, Sh.M. GULIYEV, Sh.O. EMINOV

Institute of Physics, National Academy of Sciences of Azerbaijan,
H. Javid Avenue, 33, AZ-1143, Baku, Azerbaijan
ismailovnamik@yahoo.com

The experimental results of study for photoelectric property of p-Cd$_x$Hg$_{1-x}$Te (x=0.24-0.3) photoconductors with conversion surface layer created by plasma treatment are presented. It is shown, that the potential barrier between p- and n-layers is reason of the sensitivity and response time τ_s enhancement of this photoconductors at T=80K. The sensitivity and response time τ_s enhance inverse proportional to background illumination level. The sensitivity $R_{vi}(\lambda_m)$=4·10^5 V/W and τ_s=(0.8-1)10^{-5}s are obtained for sensitive area 1x1 mm^2 for a 60^0 field of view and T=80K.

Keywords: infrared detector, photoconductivity, responsivity, response time.
PACS: 73.50.Pz, 73.50.Gr, 73.61.Ga, 73.40.Gv

1. INTRODUCTION

The limit performance of photoconductor mostly determined by the lifetime of excess carriers, the value of which, in turn, depends on the mechanisms of their recombination in bulk and on the surface of the semiconductor.

The performance of Hg$_{1-x}$Cd$_x$Te infrared photoconductors is strongly dependent on surface condition because of they has a highly reactive surface [1, 2]. Surface recombination reduces the total number of steady state excess carriers by effectively reducing the average recombination time. A surface band bending in the semiconductor under certain conditions can lead to decrease the surface recombination and significantly increase its responsivity [3]. Surface-controlled photoconductivity has been demonstrated by Kinch [4] on photoconductive element ~20 μm thick, using n-type Hg$_{1-x}$Cd$_x$Te with x = 0.2 and x = 0.3. In this MIS structure, the photosignal enhancement for x=0.3 composition is observed at 77K on changing the gate voltage from accumulation to depletion condition. However, for x= 0.2 composition, photosignal decreases more than an order of magnitude. This may be relates with high density of surface states and low surface mobility [5].

Another effect, that limits responsivity, is sweep-out of minority carriers [6, 7] related with bipolarity of photoconductivity. At some applied voltage, when minority carriers can drift to ohmic contacts in a time short compared to recombination time, they are removed at an ohmic contact and the density of excess curriers in bulk reduces. This results in limiting the maximum applied voltage and reduction of responsivity.

However, in two-layer photoconductor (PC) in which the thin photoconductive layer is created on another layer with revers conductivity and separate from it by p-n junction, the both effects can be eliminated. In this case, like in p-n junction, the influence of surface recombination can be significantly reduced and as shown in [8], the presence of the quasi-neutral regions practically does not affect the responsivity of the structure and photoconductivity is monopolar. Therefore, it is interesting experimentally to study of such two-layer structure based on Hg$_{1-x}$Cd$_x$Te and to establish the condition of achievement its high responsivity.

This paper presents the results of an experimental study of a thin n-type layer photoconductivity obtained by plasma treatment on the surface of p-Hg$_{1-x}$Cd$_x$Te (x=0.24-0.3) bulk. It is considered the plasma etching has a softer effect on the material, since midget ion energy (order of tens of eV or less) avoids the generation of radiation-induced defects [9]. This method allows obtain very high quality layers of n-type conductivity with the high charge carrier mobility and is used for the manufacture of photodiodes and photoconductors [9, 10].

2. METHOD OF EXPERIMENT

For sample preparation we used vacancy-doped and Cu, Au doped p-type conductivity Hg$_{1-x}$Cd$_x$Te (x = 0.23-0.3) single crystals with N$_A$- N$_D$ = (0.5-2) ·10^{16} cm^{-3} и μ$_p$= (4-6)·10^2 cm^2/B·s at T=80K. The Hg$_{1-x}$Cd$_x$Te slab was bonding using low- temperature epoxy on the substrate and thinned to of 0.1-0.3mm. The sample surface was mechanical polishing and then etching in a 4% solution of bromine in methanol and washing with methanol. The dimensions of the sensitive area were 5x1 mm and 1x1 mm. As an ohmic contact to p-type chemical deposition of gold, and to the n-type the indium by vacuum thermal deposition was used. To avoid damages during wire bonding the metallisation continued on substrate as it is shown in fig.1. ZnS with the thickness of about 0.5 microns was used as passivation layer.

Plasma etching was carried out immediately after chemical etching in a vacuum chamber at T = 300 K with a current density of high-frequency discharge (40 MHz) plasma 6-10 μA/cm^{-2} for 1-2 min. We assume the profile of the distribution of charge carriers in the depth, as it is well known [9,10], has a form which is characteristic for the n+-n-p structure (fig.2,).To determine the concentration of free electrons in the n-layer specifically mesa structured photodiode was prepared.
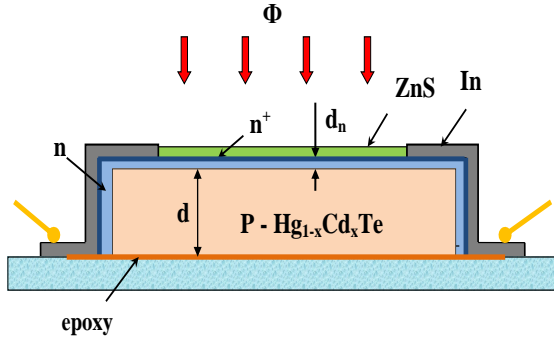
N.J. ISMAYILOV, E.K. HUSEYNOV, A.A. ALIYEV, I.S. HASANOV, Sh.M. GULIYEV, Sh.O. EMINOV
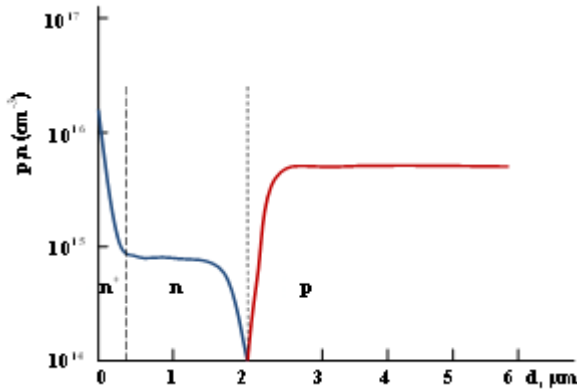
Fig.1. Schematic illustration of investigated photoconductor.

Fig.2. Impurity profile in the transverse cross section of two-layer photoconductor   and corresponding it energy diagram in p- $Hg_{1-x}Cd_xTe$.

From C-V measurement is found that the n-layer is characterized by carrier concentration with an order of magnitude lower than the p-region of the sample, and the barrier height φ_b = 0.2-0.16 eV, depending on the composition and concentration of charge carriers. Photovoltage produced by background radiation reaches the value of 110 me, which indicates on high quality of the n^+-np junction.

Necessary for the analyses of photo effect the concentration and mobility of the majority charge carriers were determined based on measurements of the Hall effect and conductivity. Bulk lifetime τ_v was determined by the method of compensation of PEM effect with photoconductivity [8]. Measurement of the photoconductivity spectra was carried out using a grating monochromator at 1.2 kHz modulation frequency of radiation from globar. Surface lifetime τ_s determined from the decay of photoconductivity signal in pulsed illumination of the GaAs LED. To measure the absolute value of the photoconductivity signal the radiation from a blackbody with T = 500 K and calibrated amplifier with a gain of 10^5 was used.

2.   RESULTS AND DISCUSSION

The analysis of results we carry out by comparison the photoelectric properties of uniform p-type PC with that of two-layer PC fabricated by the formation on its surface a thin layer of n-type conductivity. In fig.3 it is

shown the spectral dependence of the photoconductivity of the samples before and after the formation of n-layer at T = 80K. As it can be seen from the figure, the spectral dependence of two-layer PC increases in short-wavelength region, whereas the maximum sensitivity is shifted somewhat toward shorter wavelengths in comparison with the p-type PC. Its surface response time τ_s decrease in comparison with the value of p-type PC. Despite this, the signal response of two- layer PC under total flux of the background radiation increases in 40-80 times. This is achieved mainly due to a significant increase of the bias voltage up to Joule heating, while for p-type PC the photo signal U_s saturates at bias voltage U_b =0,16-0.9 V due to extraction effect of excess carriers (fig.4). With reducing of background flux, using a cooled diaphragm, the surface response time τ_s and thus photo signal increase more than tenfold, as it is shown in the fig.4.
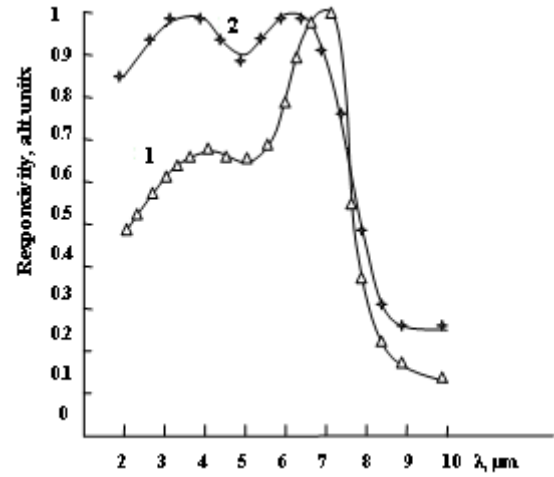

Fig.3. The spectral dependence of the sensitivity of the p-$Hg_{1-x}Cd_xTe$ photoconductors before (1) and after (2) forming of a surface layer of n-type conductivity for x = 0.24 (a) at T= 80 K.
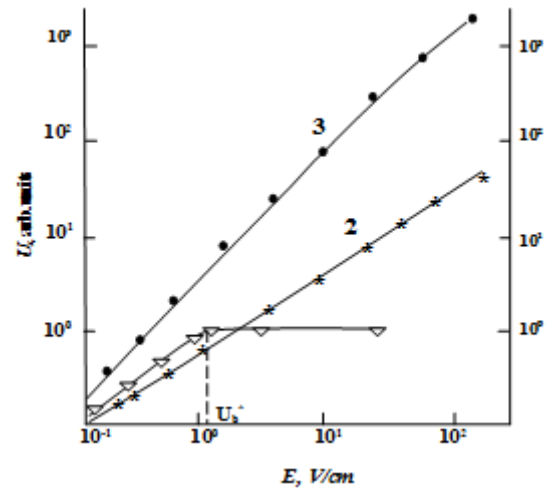

Fig.4. The dependence of response signal on applied voltage for p- $Hg_{1-x}Cd_xTe$ (x=0.28) PC (1,3) with p_0=8·10^{-15}cm^{-3}, τ_n=1,2 μs (1) and two-layer PC (2,3) under background radiation flux $\Phi_{b\,,cm}{}^{-2}c^{-1}$: 10^{16}(2), 10^{14} (3) and T= 80 K.

The observed features are due to the presence of the p-n junction space charge region (SCR) in the interface region (fig.5). Field of SCR spatially separates generated electron-hole pairs and act as a potential barrier φ_b for their recombination. The electrons generated by incident photon flux Φ within SCR and within the diffusion length of electron L_n from it in the p-region are accumulated at the boundary n-layer with SCR and cause compensation of acceptor's charge in it, while photo-holes on the boundary of SCR and quasi-neutral p-type region. The width of SCR a in this case is decreasing, while the quasi-neutral region of n-layer d_n is increasing. Thus, the conductivity modulation of n-layer is done only by photoelectrons and therefore, the photoconductivity is unipolar.

The recombination rate of excess curriers determined by the response time constant $\tau_b=R_dC_d$, where R_d, C_d are differential resistance and a barrier capacity of the p-n junction, respectively. Under thermal equilibrium time constant is controlled by the dominant dark current source that is by the diffusion, depletion region, surface or tunnel current. Assuming the dominant mechanism is diffusion, response time may be determined by the formula [8] below:

$$\tau_b = \frac{kT}{2\varphi_b'} \frac{N_d N_a}{N_a + N_d} \frac{a}{a + L} \frac{1}{g_b + v} , \qquad (1)$$

where k is Boltzmann's constant, T is absolute temperature, N_a, N_d are concentrations of acceptors and donors in the p and n-layers, respectively, φ_b^r is the potential barrier under background radiation, v is the effective rate of heat generation in the quasi-neutral regions, $g_b = \eta a \Phi_b$ is the rate of generation of carriers background radiation Φ_b is photon flux density of the background radiation, η is quantum efficiency, α is radiation absorption coefficient.

For the calculation of the voltage spectral responsivity of two-layer PC the expression obtained in [8] should be used:

$$R_{vi} = \frac{\eta\lambda(a+L)\alpha\tau U_n}{hcAN_d}\left[d_n + \frac{a}{2}\left(\frac{\pi \cdot kT}{\varphi_b}\frac{N_a}{N_a + N_d}\right)^{1/2}\right]^{-1} \quad (3)$$

where d_n is the thickness of n-layer, λ-wavelength of the incident radiation, h-Planck's constant, c-is the speed of light, A is the area of the sensitive area, U_n is applied voltage.

The observed features of the spectral characteristics of responsivity are inherent to photodiodes and are well described by the formula $\eta = \eta_0\left(1 - e^{-\alpha d_n}/(1+\alpha L)\right)$ [13], where η_o – is the internal quantum efficiency. Here, to explain the response enhancement in the short wave region, we must prior to take account, that surface recombination is reduced by transvers field on the surface provided by n$^+$-n accumulation layer [14]. If surface mobility of charge curriers is the same as in the bulk, so signal response enhancement at $hv>1,4Eg$ occurs due to increasing of η_o, as we assume.

With decreasing of d less than the bipolar diffusion length L, begins to affect recombination of excess carriers on the back and front surfaces of the sample. Therefore, the optimal thickness of the experimental samples is taken $d \leq L$.

For uniform p-type PC the responsivity is expressed as [12]:

$$R_{vp} = \frac{\eta\lambda(\mu_n\tau_n + \mu_p\tau_p)\cdot U_p^*}{hc\cdot l\cdot w\cdot d \cdot(\mu_n n + \mu_p p)} \qquad (4)$$

here μ_n, μ_p –mobility of electrons and holes, and τ_n, τ_p-their lifetimes, respectively, $\eta = \eta_0\left(1 - e^{-\alpha d}\right)$-for uniform photoconductors [14].

Since $\mu_n\tau_n \gg \mu_p\tau_p$, then in case of $\mu_n n \ll \mu_p p$, we have:

$$R_{vp} = \frac{\eta\lambda b\tau_n U_p^*}{hc\cdot l\cdot w\cdot d \cdot p} , \qquad (5)$$

where $b=\mu_n/\mu_h$, from (3) and (5) we have a ratio for the maximum of responsivity:

$$\frac{R_n}{R_p} = \frac{p\cdot d}{b\cdot n_n \cdot d_n}\frac{\tau_b}{\tau_n}\frac{U_n}{U_p^*} \qquad (6)$$

Numerically evaluating this relationship, we note that in our case $p \cdot d / n_n d_n \approx 10^3$, and $\tau_b/\tau_n \ll 1$. The high intensity of the background radiation results in a significant lowering of the potential barrier height ($\Delta\varphi_b \gg kT/q$), as a result of the rate of recombination of excess carriers in the SCR can exceed the rate of them recombination on the surface and in the bulk. In this case, τ_b is less than the bulk lifetime τ_n. Calculation based on the formula (2) gives $\tau_b = (4-8)\cdot 10^{-8}$ s, which is 10-30 times less than τ_n for vacancy-doped and specially doped samples.
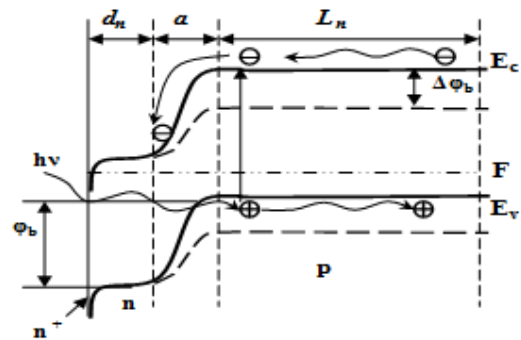

Fig.5. Energy diagram in p- Hg$_{1-x}$Cd$_x$Te .

Nevertheless, as result of $R_n(\lambda_m)/R_p(\lambda_m) \gg 1$. In accordance with formula (2), τ_b increases inversely proportional to the intensity of the background radiation. In this case, responsivity should also to grow, which is observed experimentally.
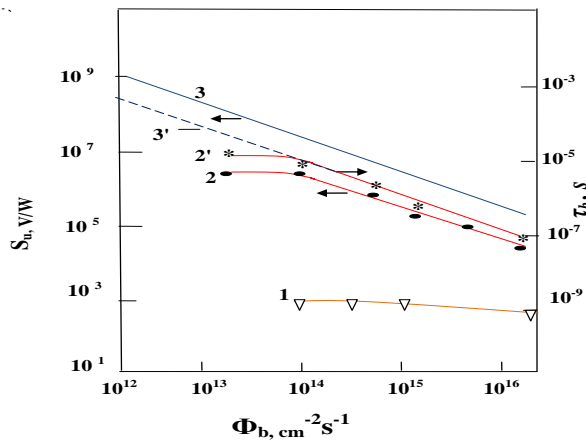
Fig.6. Dependence of responsivity (1,2,3) and response time τ_b (2′,3′) on the background radiation flux for $Hg_{1-x}Cd_xTe$ photoconductors with x = 0.28 and sensitive area 1x1 mm^2 at T=80 K. (1) corresponds to the measured responsivity of uniform p-type PC with τ_n=1,2 μs , (2,2′) calculated and (3,3′) values for two-layer PC.

The measured and calculated responsivity and response time versus the background radiation flux for $Hg_{1-x}Cd_xTe$ photoconductor with $x = 0.28$ are shown in fig.6. As it is seen, the R_p is not varied, while R_n and τ_b increase with lowering of background radiation flux. However, for $\Phi_b < 10^{14}$ cm^{-2}s^{-1} the R_n and τ_b have constant

value. It is may be caused by surface leakage current due to non-passivated backside of sample that is limited R_d, hence τ_b and R_n. It is possible to achieve more high responsivity at low background radiation flux, probably, if to use epitaxial $Hg_{1-x}Cd_xTe$ film passivated by CdTe or graded layer. For $Hg_{1-x}Cd_xTe$ (x=0,28) two-layer PC with 1x1 mm^2 sensitive area at an field of view $\theta = 50°$ achieved the following parameters: $R_{vi}(\lambda_m)$=4·10^6 V/W, τ_s=(0.8-1)·10^{-5}s at $T = 80$K.

CONCLUSION

In a processing in the plasma of high-frequency discharge with surface of p- $Hg_{1-x}Cd_xTe$ ($x = 0.23-0.3$), converted layers with thickness of 2-3 μm ave been obtained. The layers were characterized by a low concentration of charge carriers in comparison with their concentration in the p-region and form a high quality n + - n-p junction. Due to the recombination potential barrier, this way obtained two-layer photoconductor have a high responsivity, which increases as the level of background radiation decreases. High responsivity, ease of manufacture and suitability for the production of lower-quality p-type material, allow us to consider it as an alternative to other types of photodetectors based on $Hg_{1-x}Cd_xTe$.

_____

[1] *M.B. Reine, K.R. Maschhoff, S.P. Tobin, P.W. Norton, J.A.Mroczkowki and E.E.Krueger.* Semicond. Sci.Technol. 1993, **8**. 788.

[2] *Y. Nemirovsky and G. Bahir.* J.Vac.Sci.Technol. 1993, **A7**,450.

[3] *M.A. Kinch.* Semiconductors and semimetals, 1981, **18**, 313.

[4] *M.A. Kinch.* J.Vac.Sci.Technol. **21,** 215 (1982).

[5] *E.K. Huseynov, N.D. Ismayilov.* Sov. Phys.-Semicond,1995, **29**, 1790 .

[6] *M.R. Jonson.* J.Appl.Phys. 1972,**43**, 3090.

[7] *S.P. Emmons and K.L, Ashley.* Apll.Phys.Lett., 1972, **20**, 241,.

[8] *L.N. Neustroyev, V.V. Osipov.* Sov. Phys.-Semicond**.** 1981, **15**, 1062 .

[9] *K.D. Mynbaev, V.I. Ivanov-Omskiy.* Semiconductors, 2003, **37**, 1127.

[10] *R. Pal, V. Mittal, R.K. Sharma, P.K. Basu.* Defence Sci., 2009, **4**,395,.

[11] *Yu.I. Ravich.* Photomagnetic effect in semiconductors and its application. M. Sov.Radio, (1967).

[12] Solid state imaging. Edited by *P.G. Jespers, F. Van de Wiele and M.H. White.* Noordhoff-Leyden. 1976.

[13] *R. Singh and V. Mittal.* Defence Science, 2003, **53**, 281.

PHASE TRANSITION IN ISING MAGNETIC HEXAGONAL NANOWIRES: EFFECTIVE- FIELD THEORY APPROACH

V.A. TANRIVERDIYEV, V.S. TAGIYEV, G.G. KERIMOVA

Institute of Physics of the National Academy of Sciences of Azerbaijan, Baku Az -1143, Baku, H.Javid ave.33, E-mail: Vahid_tanriverdi @yahoo.com

By means of the effective-field theory with correlations, the critical behavior of hexagonal magnetic nanowire is considered. The transition temperature T_c for   a spin-1/2 hexagonal Ising nanowires are calculated as a function of exchange constant by the transfer matrix method. The effects of surface modification are also studied numerically.

Keywords: Nanowires, effective-field theory, phase transition.
PACS: 75.70. Ak

1.   INTRODUCTION

In resent years, the number of theoretical and experimental investigations of various structures in the nanometer scale, such as nanowires, nanotubes, nanofilms, nanoparticles, nanobelts etc. have increased [1-4]. Studying the properties of these nanostructures provides considerable insight for possible applications. One of the potentially interesting aspects of nanophysics is related to magnetic phenomena. Nano-scale materials can be used in biomedical applications, nonlinear optics, magnetic recording media and electronic devices, sensors, environmental remediation and etc [5-7]. Resent advances in the microprocessing technology enable us to fabricate magnetic materials with various sample structures on nanometer scale. For example, Ebels and Wigen have created arrays of very long ferromagnetic nanowires of Ni, permalloy and Co, with diameters in the range of 35 to 500 nm and have carried out ferromagnetic resonance studies of their samples [8] .

Different types of theoretical techniques, such as Green functions method, mean-field theory, effective field theory (EFT) with correlations, Monte   Carlo simulations, transfer matrix formalism, recurrence relations technique have been used for the investigations of magnetic properties of nanomaterial [9-11].   On the other hand, various geometric configurations can be modeled as having a chosen shape and size cross section with a finite number spins arranged [12-13].

In comparison with bulk systems one finds unexpected and interesting properties in the various layered structures.   The critical behavior of magnetic films and superlattice have been examined, either experimentally or theoretically [10-11].   It is well known that the bulk transition temperature is approximately proportional to the exchange coupling. The atoms at the surface are in different environment, and exchange constant between them may differ from those in the bulk. From the works devoted to the magnetic properties of surfaces, we can see that a magnetically ordered surface can coexist with a magnetically disordered bulk phase [14-15].

In this paper, we are concerned with phase transition in hexagonal magnetic nanowire (HMN).   We study them within the framework of the effective-field theory approach. In Section 2, we present the model of HMN and derive the equation that determines the transition temperatures. The equation is general one for arbitrary exchange interaction. Numerical results and discussion are given in section 3.

2.   MODEL AND FORMALISM

The schematic representation of hexagonal magnetic nanowire (HMN) model with core/shell structure is shown in fig.1.
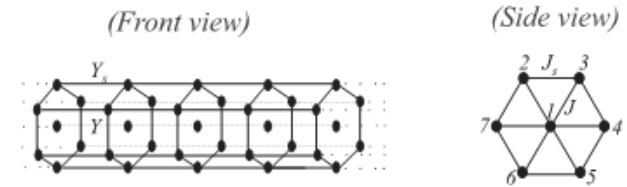

Fig. 1. Model of hexagonal ferromagnetic nanowires. The nanowires are infinite in the direction perpendicular to the axes z.

The exchange constant between two nearest-neighbor magnetic atoms at the surface shell and the core is denoted by J , and J_s is exchange constants between spins at the surface shell in intralayer. On the other hand each magnetic atom connects to the two nearest-neighbor magnetic atoms along the wire, and   corresponding exchange constants between spins at the surface shell and the core are Y_s and Y , respectively.

The Ising Hamiltonian of the system can be written in the form

$$H = -\sum_{\substack{n,\tau,\tau', \\ (\tau \neq \tau')}} J_{n,n}^{\tau,\tau'} (S_n^\tau S_n^{\tau'}) - \sum_{n,\tau} \left(Y_{n,n-1}^{\tau,\tau} (S_n^\tau S_{n-1}^\tau) + Y_{n,n+1}^{\tau,\tau} (S_n^\tau S_{n+1}^\tau) \right) \tag{1}$$

where the first term describes exchange interactions inside atomic layer, the second term describes exchange interactions between neighboring atomic layers. The external magnetic field is neglected for simplicity. Here, n is the index of atomic layer, τ describes the position of a lattice site in this layer. The axis z of the coordinate system is along the nanowires under study.

To evaluate the mean spin $m_n^\tau = \langle S_n^\tau \rangle$ $(\tau = 1, 2,...7)$, we start with the exact Callen identity [16],

$$m_n^{(\tau)} = \left\langle \tanh\left[\left(\sum_{\tau'} J_{n,n}^{\tau,\tau'} m_n^{(\tau')} + Y_{n,n+1}^{\tau,\tau} m_{n+1}^{(\tau)} + Y_{n,n-1}^{\tau,\tau} m_{n-1}^{(\tau)}\right)\Big/ kT\right]\right\rangle \tag{2}$$

where k is Boltzman constant and T is temperature. According to the framework of EFT, the average atomic magnetization m_C at the core and magnetization m_s at the shell surface are given

$$m_c = \left[\cosh(YD) + m_c \sinh(YD)\right]^2 \cdot \left[\cosh(JD) + m_s \sinh h(JD)\right]^6 \tanh(\beta x)\Big|_{x=0} \tag{3a}$$

$$m_s = \left[\cosh(Y_s D) + m_s \sinh h(Y_s D)\right]^2 \left[\cosh(J_s D) + m_s \sinh h(J_s D)\right]^2 \left[\cosh h(JD) + m_c \sinh h(JD)\right]\tanh(\beta x)\Big|_{x=0} \tag{3b}$$

where $\beta = 1/kT$, $D = \partial/\partial x$ is differential operator and satisfies the relation

$$\exp(\alpha D) f(x) = f(x + \alpha) \tag{4}$$

As the temperature becomes higher than the critical temperature T_c the whole system becomes demagnetized and the average atomic magnetization approaches zero. Near the critical temperature T_c mean spins $m_{C(S)}$ become small. Consequently, all terms of the order higher than linear in eqs. (3) can be neglected and eqs.(3) can be rewritten as follows:

$$m_c = \left[\cosh^2(YD) + m_c \sinh(2YD)\right] \cdot \left[\cosh^6(JD) + 3\cosh^4(JD)\sinh(2JD)m_s\right]\tanh(\beta x)\Big|_{x=0} \tag{5a}$$

$$m_s = \left[\cosh^2(Y_s D) + m_s \sinh(2Y_s D)\right] \cdot \left[\cosh^2(J_s D) + m_s \sinh(2J_s D)\right] \cdot \left[\cosh(JD) + m_c \sinh(JD)\right]\tanh(\beta x)\Big|_{x=0} \tag{5b}$$

The set of equations (5) reduces to the secular equation

$$\begin{vmatrix} 1 - \lambda_1 & -\lambda_2 \\ -\gamma_2 & 1 - \gamma_1 \end{vmatrix} = 0 \tag{6}$$

where the coefficients have the following form:

$$\lambda_1 = \left[20\tanh(2Y\beta) + 15\{\tanh(2Y - 2J)\beta + \tanh(2Y + 2J)\beta\} + 6\{\tanh(2Y - 4J)\beta + \tanh(2Y + 4J)\beta\} + \right.$$
$$\left. + \tanh(2Y - 6J)\beta + \tanh(2Y + 6J)\beta\right]/64$$

$$\lambda_2 = \left[30\tanh(2J\beta) + 24\tanh(4J\beta) + 6\tanh(6J\beta) + 15\{\tanh(2J - 2Y)\beta + \tanh(2J + 2Y)\beta\} + \right.$$
$$\left. + 12\{\tanh(4J - 2Y)\beta + \tanh(4J + 2Y)\beta\} + 3\{\tanh(6J - 2Y)\beta + \tanh(6J + 2Y)\beta\}\right]/64$$

$$\gamma_1 = \left[2\tanh(2Y_s - J)\beta + 2\tanh(2Y_s + J)\beta + \tanh(2Y_s - J - 2J_s)\beta + \tanh(2Y_s - J + 2J_s)\beta + \tanh(2Y_s + J - 2J_s)\beta + \right.$$
$$+ \tanh(2Y_s + J + 2J_s)\beta + 2\tanh(2J_s - J)\beta + 2\tanh(2J_s + J)\beta + \tanh(2J_s - J - 2Y_s)\beta + \tanh(2J_s - J + 2Y_s)\beta +$$
$$\left. + \tanh(2J_s + J - 2Y_s)\beta + \tanh(2J_s + J + 2Y_s)\beta\right]/8$$

$$\gamma_2 = \left[4\tanh(J\beta) + 2\tanh(J - 2Y_s)\beta + 2\tanh(J + 2Y_s)\beta + 2\tanh(J - 2J_s)\beta + 2\tanh h(J + 2J_s)\beta + \right.$$
$$\left. + \tanh(J - 2Y_s + 2J_s)\beta + \tanh(J + 2Y_s - 2J_s)\beta + \tanh(J - 2Y_s - 2J_s)\beta + \tanh(J + 2Y_s + 2J_s)\beta\right]/16$$

From the numerical calculation of secular equation (6) we can determine the transition temperature of the HMN as a function of exchange constants (fig. 2).
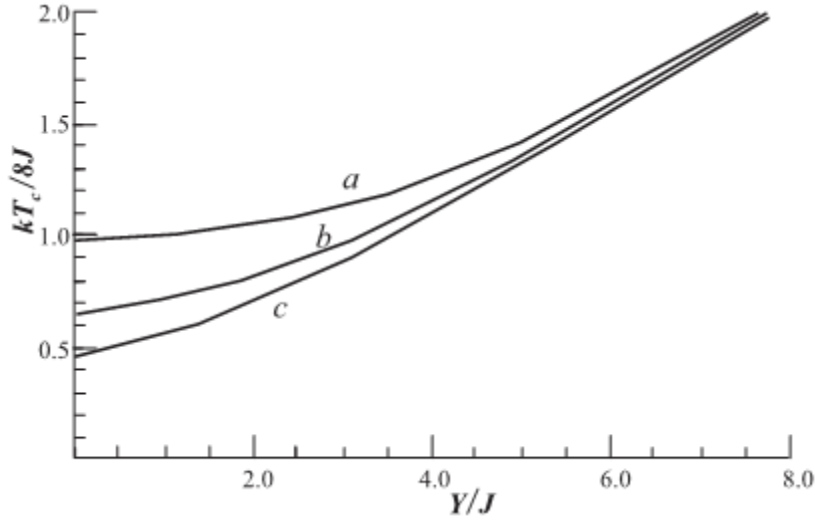

Fig. 2. Critical temperatures as a function of Y/J_a, and labeling curves corresponds to a $J_s/J = 2.5$, $Y_s/J = 1$; b, $J_s/J = 1$, $Y_s/J = 1$; c, $J_s/J = 0.1$, $Y_s/J = 1$.

3. CONCLUSION

The formalism of transition temperature derivation obtained above is universal and can be used for both ferromagnetic and antiferromagnetic cases. Hence, positive core-shell coupling ($J > 0$) and negative core-shell coupling ($J < 0$) correspond to ferromagnetic interfacial and antiferromagnetic one couplings, respectively. On the other hand, if $Y_s > 0 (Y > 0)$ the neighboring spins belonging to different layers on the shell surface (core) are parallel and they show ferromagnetic behavior.   If $Y_s < 0 (Y < 0)$ their behavior is antiferromagnetic.

As numerically illustration, in Fig. 2, we show the results for the ferromagnetic hexagonal nanowires. The transition temperature (in unit $T = 8J/k$) is plotted as function of Y/J. The curve labeled b, corresponds to the case at which all exchange constants are equal to each other. When J_s increases then the critical temperature increases (the curve labeled a), but when J_s decreases (the curve labeled c) then it against decreases. Analysis shows that when the J_s and Y_s change transition temperatures are same. The cause of this is connection of each surface spin to the two nearest-neighbor magnetic atoms both along the wire (Y_s) and intralayer (J_s).

_____

[1] *X.Y. Lu, H. Li, B. Wang.* Journal of the Mecanics and Physics of Solids 59 (2011) 1966-1977.
[2] *L. Wang, Y.F. Zhang.* Physica E 43 (2011) 889-892.
[3] *A.L. Gonzalez, P. Landeros, Alvaro S. Nunez.* J.Magn. Magn.Matter. 322, (2010) 530-535.
[4] *Z.K. Wang, M.H. Kuok, S.C. Ng, D J. Lockwood, M.G. Cottam, K. Nielsch, R. B. Wehrspohn, and U. Gösele.* Phys. Rev. Lett. v.89, n.2, (2002) 027201.
[5] *C. Alexiou, A. Schmidt, R. Klein, P. Hullin, C. Bergemann and W. Arnold.* (2002) J.Magn. Magn.Matter. 252, 363
[6] *G.V. Kurlyandskaya, M.L. Sanches, B. Hernando, V.M. Prida, P. Gorria and M. Tejedor.* (2003) Appl. Phys. Lett. 82, 3053.
[7] *Fert And L. Piraux.* (1999) J.Magn. Magn.Matter. 200, 338.

[8] *U. Ebels, J. -L. Duvail, P.E. Wigen, L. Piraux, L. D. Buda, and K. Ounadjela.* Phys. Rev. B 64, (2001)
[9] 144421.
[10] *V.V. Kruglyak, R.J. Hicken, A.N. Kuchko, V.Yu. Gorobets.* Journal of Applied Physics 98, (2005) 014304.
[11] *Y.M. Seidov and G.R. Shaulov.* J.Phys.: Condens. Matter 6 (1994) 9621.
[12] *T. Hai.* Journal of Magnetism and Magnetic Materials 97, (1991) 227-234.
[13] *T.M. Nguyen and M.G. Cottam.* Phys.Rev. B 71, (2005) 094406.
[14] *T.M. Nguyen and M.G. Cottam.* Journal of Magnetism and Magnetic Materials 272-276, (2004) 1672.

[15] *D. Weller, S.F. Alvarado, W. Gudat, K. Schröder, M. Campagna.* Physical review letters 54 (14), 1555

[16] *C. Rau, C. Jin, M. Robert.* J.Appl. Phys. 63 (1988) 3667.

[17] *H.B. Callen.* Phys.Lett. (1963) 4, 161.

[18] *O. A. Tretiakov and Ar. Abanov.* Phys. Rev. Lett. 105, (2010) 157201.

[19] *Ghaddar, F. Gloaguen, J. Gieraltowski.* Jornal of Physics: Conference Series 200, (2010) 072032.

[20] *H. Leblond, V. Veerakumar, M. Manna.* Physical Review B 75, (2007) 214413.

[21] *Chen Wen-Bing, Han Man-Gui, Zhou Hao, Ou Yu and Deng Long-Jiang.* Chinese Phys. B 19 (2010) 087502.

[22] *O. Dmytriiev, U. A. S. Al-Jarah, P. Gangmei, V. V. Kruglyak, R. J. Hicken, B. K. Mahato, B. Rana, M. Agrawal, A. Barman, M. Mátéfi-Tempfli, L. Piraux, and S. Mátéfi-Tempfli.* Phys. Rev. B 87, (2013) 174429.

[23] *Wei Yang, Chunxiang Cui, Qiaozhi Liu, Bin Cao, Lian Liu, Yajin Zhang.* Journal of Crystal Growth Volume 399, (2014) Pages 1–6.

[24] *V.V. Kruglyak, R.J. Hicken, A.N. Kuchko, V.Yu. Gorobets.* Journal of Applied Physics 98, (2005) 014304.

[25] *T.M. Nguyen and M.G. Cottam.* Phys.Rev. B 71, (2005) 094406.

[26] *T.M. Nguyen and M.G. Cottam.* Journal of Magnetism and Magnetic Materials 272-276, (2004) 1672.

[27] *Y.M. Seidov and G.R. Shaulov.* J.Phys.: Condens. Matter 6 (1994) 9621.

[28] *T. Hai.* Journal of Magnetism and Magnetic Materials 97, (1991) 227-234.

[29] *Xiao-Guang Wang, Shao-Hua Pan, Guo-Zhen Yang.* Solid State Commun. 113 (2000) 59-62.

[30] *R.E. Camley and D.R. Tilley.* Phys.Rev.B 37 (1988) 3413.

HIGGS BOSON PRODUCTION IN LEPTON COLLISIONS

S.K. ABDULLAYEV, M.Sh. GOJAYEV, F.A. SADDIGH

Baku State University, Az-1148, Z. Khalilov str., 23
s_abdullayev@mail.ru, m_qocayev@mail.ru, f_seddig@yahoo.com

In the framework of Standard Model the process of scalar Higgs boson production in e^-e^+-collisions has been investigated: $e^-e^+ \Rightarrow He^-e^+$. It is shown that, the annihilation (scattering) diagram is defined by only four helicity amplitudes $F_{LL}^{(a)}, F_{LR}^{(a)}, F_{RL}^{(a)}, F_{RR}^{(a)}$ ($F_{LR}^{(b)}, F_{RL}^{(b)}, F_{LL}^{(b)}, F_{RR}^{(b)}$). A compact expressions for the cross sections of the Higgs-strahlung and *ZZ* fusion mechanisms, including the interference terms, have been derived. Finally extensive numerical applications to $e^-e^+ \Rightarrow He^-e^+$ reaction in the 500 *GeV* energy domain are presented.

Keywords: Higgs boson, left and right coupling constants, Weinberg's parameter, Higgs-strahlung mechanism, *ZZ* fusion mechanism.
PACS: 12.15.-y; 12.15.Mm; 14.70.Hp.

INTRODUCTION

The Standard Model *(SM)* to describe the strong and electroweak interactions between quarks and leptons, is based on the gauge symmetry group $SU(3)_C \times SU(2)_L \times U(1)_Y$. A cornerstone of the *SM* is the mechanism of spontaneous electroweak symmetry breaking. An *SU*(2) doublet of complex scalar field is introduced and its neutral component develops a non-zero vacuum expectation value. As a consequence, the electroweak $SU(2)_L \times U(1)_Y$ symmetry is spontaneously broken to the electromagnetic *U*(1)_Q symmetry. Three of the four degrees of freedom of the doublet scalar field are absorbed by the $W^\pm$ and *Z* weak vector bosons to form their longitudinal polarizations and to acquire masses. The remaining degree of freedom corresponds to a scalar particle, the Higgs boson.

The high-precision measurements carried out at SLC, LEP, Tevatron and established that the couplings of quarks and leptons to the electroweak gauge bosons and the trilinear couplings among vector bosons agree with those predicted by the SM. The only sector of the model which has not yet been probed in a satisfactory way is the scalar sector. Some experiments are carried out for the discovery of Higgs boson in different experimental labs. Finally in LHC new information are received concerning the existence of Higgs boson with the mass of 125 GeV [1-3]. So the channels which give rise to Higgs bosons have got more attensions [2-11].

In this work the annihilation of $e^-e^+(\mu^-\mu^+)$-pair with longitudinal polarization is studied for the sake of production of Higgs boson and $e^-e^+(\mu^-\mu^+)$ pairs:

$$e^- + e^+ \Rightarrow H + e^- + e^+. \qquad (1)$$

1. The Higgs-strahlung mechanism.

The Feynman diagrams for the process (1) are shown in Fig. 1 (the momentum and helicity of the particles are shown in parentheses). First diagram is the Higgs-strahlung diagram i.e. e^-e^+-pairs first annihilate to Z^0 boson and Z^0 in turn transforms to e^-e^+-pair while emitting Higgs boson.

The helicity is conserved at high energy. The conservation of helicity imply that e^- and e^+ colliding at the same vertex to have opposite helicities: $e_L^- e_R^+$ or $e_R^- e_L^+$. So, four helicity amplitudes will correspond to the diagram a): $F_{LL}^{(a)}$, $F_{LR}^{(a)}$ $F_{RL}^{(a)}$ and $F_{RR}^{(a)}$ (first and second indices indicate the initial and final helicity of electron). These helicity amplitudes are given by following expressions:

$$F_{LL}^{(a)} = D_Z(s) D_Z(xs)\, g_L^2, \qquad F_{LR}^{(a)} = D_Z(s) D_Z(xs) g_L g_R$$
$$F_{RL}^{(a)} = D_Z(s) D_Z(xs)\, g_R g_L \qquad F_{RR}^{(a)} = D_Z(s) D_Z(xs)\, g_R^2. \qquad (2)$$

Here

$$g_L = -\frac{1}{2} + \sin^2\theta_w,\ g_R = \sin^2\theta_w \qquad (3)$$

are the left and right coupling constants for interaction of electron with Z^0 boson, θ_w is the Weinberg angle,

$$D_Z(s) = (s - M_Z^2)^{-1}, \quad D_Z(xs) = (sx - H_Z^2 + iM_Z\Gamma_Z)^{-1},$$

$$(4)$$

$\sqrt{s}$ is the total energy of $e^- e^+$-pair in the center of mass system, M_Z and Γ_Z are the mass and total width of Z boson,

$$x = 1 - \frac{2\omega}{\sqrt{s}} + \frac{M_H^2}{s}, \tag{5}$$

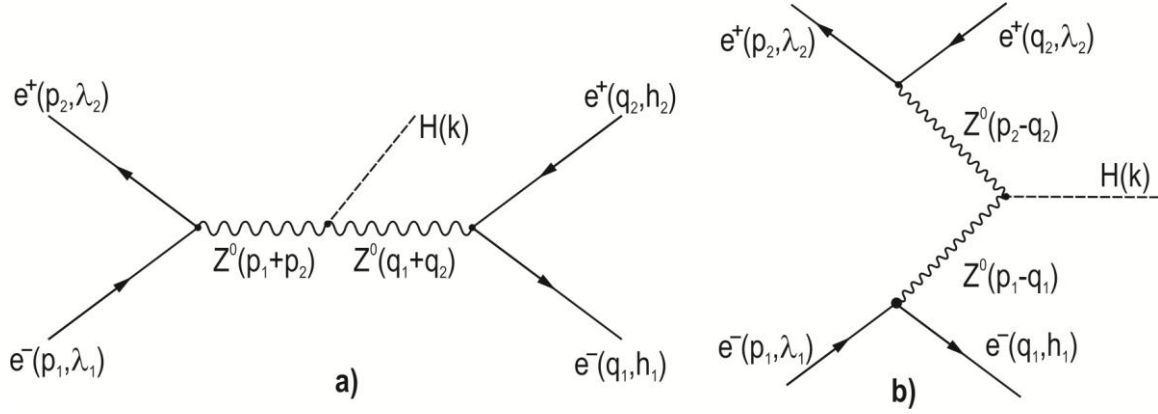ω and M_H are the energy and mass of Higgs boson.

Fig. 1. The Feynman diagrams for $e^- e^+ \Rightarrow H e^- e^+$.

The transition amplitude for the diagram a) we can write as:

$$M_a(e^- e^+ \Rightarrow H e^- e^+) = \left(\frac{e}{2\sin\theta_w \cdot \cos\theta_w}\right)^3 \times$$

$$\times M_Z\{F_{LL}^{(a)}[\overline{\upsilon}(p_2,\lambda_2)\gamma_\mu(1+\gamma_5)u(p_1,\lambda_1)][\overline{u}(q_1,h_1)\gamma_\mu(1+\gamma_5)\upsilon(q_2,h_2)] +$$

$$+ F_{LR}^{(a)}[\overline{\upsilon}(p_2,\lambda_2)\gamma_\mu(1+\gamma_5)u(p_1,\lambda_1)][\overline{u}(q_1,h_1)\gamma_\mu(1-\gamma_5)\upsilon(q_2,h_2)] +$$

$$+ F_{RL}^{(a)}[\overline{\upsilon}(p_2,\lambda_2)\gamma_\mu(1-\gamma_5)u(p_1,\lambda_1)][\overline{u}(q_1,h_1)\gamma_\mu(1+\gamma_5)\upsilon(q_2,h_2)] +$$

$$+ F_{RR}^{(a)}[\overline{\upsilon}(p_2,\lambda_2)\gamma_\mu(1-\gamma_5)u(p_1,\lambda_1)][\overline{u}(q_1,h_1)\gamma_\mu(1-\gamma_5)\upsilon(q_2,h_2)]\}. \tag{6}$$

Let's first calculate the square of amplitude

$$M_a(e^- e^+ \Rightarrow H e^- e^+)_I = \left(\frac{e}{2\sin\theta_w \cdot \cos\theta_w}\right)^3 \cdot M_Z \cdot F_{LL}^{(a)} \times$$

$$\times [\overline{\upsilon}(p_2,\lambda_2)\gamma_\mu(1+\gamma_5)u(p_1,\lambda_1)][\overline{u}(q_1,h_1)\gamma_\mu(1+\gamma_5)\upsilon(q_2,h_2)], \tag{7}$$

$$\left|M_a(e^- e^+ \Rightarrow H e^- e^+)_I\right|^2 = \left(\frac{e^2}{4x_w(1-x_w)}\right)^3 M_Z^2 \left|F_{LL}^{(a)}\right|^2 \cdot T_{\mu\nu}^{(1)} \cdot T_{\mu\nu}^{(2)}, \tag{8}$$

where $x_w = \sin^2\theta_w$ is the Weinberg's parameter, $T_{\mu\nu}^{(1)}$ and $T_{\mu\nu}^{(2)}$ are the tensors of 4-momentum and spiralities

for initial and final pair of $e^- e^+$:

$$T_{\mu\nu}^{(1)} = tr[\upsilon(p_2,\lambda_2)\bar{\upsilon}(p_2,\lambda_2)\gamma_\mu(1+\gamma_5)u(p_1,\lambda_1)\bar{u}(p_1,\lambda_1)\gamma_\nu(1+\gamma_5)] =$$

$$= tr\left[\frac{1+\lambda_2\gamma_5}{2}\hat{p}_2\gamma_\mu(1+\gamma_5)\cdot\frac{1-\lambda_1\gamma_5}{2}\hat{p}_1\gamma_\nu(1+\gamma_5)\right] =$$

$$= 2(1-\lambda_1)(1+\lambda_2)[p_{1\mu}p_{2\nu} + p_{2\mu}p_{1\nu} - (p_1\cdot p_2)g_{\mu\nu} - i\varepsilon_{\mu\nu\rho\sigma}p_{1\rho}p_{2\sigma}], \tag{9}$$

$$T_{\mu\nu}^{(2)} = tr[u(q_1,h_1)\bar{u}(q_1,h_1)\gamma_\mu(1+\gamma_5)\upsilon(q_2,h_2)\bar{\upsilon}(q_2,h_2)\gamma_\nu(1+\gamma_5)] =$$

$$= tr\left[\frac{1-h_1\gamma_5}{2}\hat{q}_1\gamma_\mu(1+\gamma_5)\cdot\frac{1+h_2\gamma_5}{2}\hat{q}_2\gamma_\nu(1+\gamma_5)\right] =$$

$$= 2(1-h_1)(1+h_2)[q_{1\mu}q_{2\nu} + q_{2\mu}q_{1\nu} - (q_1\cdot q_2)g_{\mu\nu} + i\varepsilon_{\mu\nu\alpha\beta}q_{1\alpha}q_{2\beta}], \tag{10}$$

The product of tensors $T_{\mu\nu}^{(1)}$ and $T_{\mu\nu}^{(2)}$ is a simple expression:

$$T_{\mu\nu}^{(1)}\,T_{\mu\nu}^{(2)} = 2^4(1-\lambda_1)(1+\lambda_2)(1-h_1)(1+h_2)(p_1\cdot q_2)(p_2\cdot q_1). \tag{11}$$

The squared transition amplitude that we obtain is:

$$\left|M_a(e^-e^+\Rightarrow He^-e^+)_I\right|^2 = \frac{1}{4}\left(\frac{e^2}{x_w(1-x_w)}\right)^3 M_Z^2\left|F_{LL}^{(a)}\right|^2 \times$$

$$\times (1-\lambda_1)(1+\lambda_2)(1-h_1)(1+h_2)(p_1\cdot q_2)(p_2\cdot q_1).$$

Because conservation of helicity no interference will happen between the of different spirality amplitudes. So, we easily will be able to calculate the square of amplitude:

$$\left|M_a(e^-e^+\Rightarrow He^-e^+)\right|^2 = \frac{1}{4}\left(\frac{e^2}{x_w(1-x_w)}\right)^3 M_Z^2\{[(1-\lambda_1)(1+\lambda_2)(1-h_1)(1+h_2)\left|F_{LL}^{(a)}\right|^2 +$$

$$+ (1+\lambda_1)(1-\lambda_2)(1+h_1)(1-h_2)\left|F_{RR}^{(a)}\right|^2](p_1\cdot q_2)(p_2\cdot q_1) + [(1-\lambda_1)(1+\lambda_2)(1+h_1)\times$$

$$\times(1-h_2)\left|F_{LR}^{(a)}\right|^2 + (1+\lambda_1)(1-\lambda_2)(1-h_1)(1+h_2)\left|F_{RL}^{(a)}\right|^2](p_1\cdot q_1)(p_2\cdot q_2). \tag{12}$$

The integration over q_1 and q_2 is conveniently performed by the invariant method [7]. Let's write the scalar product of 4-momentum in the form

$$(p_1\cdot q_1)(p_2\cdot q_2) = p_{1\mu}p_{2\nu}\cdot q_{1\mu}q_{2\nu}.$$

Then the integral

$$I_{\mu\nu} = \int q_{1\mu}q_{2\nu}\frac{d\vec{q}_1}{\omega_1}\cdot\frac{d\vec{q}_2}{\omega_2}\delta(q-q_1-q_2) \tag{13}$$

can be write as $(q = p_1 + p_2 - k)$:

$$I_{\mu\nu} = \frac{\pi}{6}[q^2 g_{\mu\nu} + 2q_\mu q_\nu].$$

(14)

In the center of initial $e^- e^+$ mass frame we get the following expression for the $p_{1\mu} p_{2\nu}$ and $I_{\mu\nu}$ tensors product:

$$p_{1\mu} p_{2\nu} I_{\mu\nu} = \frac{\pi}{12} s^2 f(\omega,\theta),$$

(15)

where

$$f(\omega,\theta) = 2x + \frac{1}{s}(\omega^2 - M_H^2)\sin^2\theta,$$

(16)

θ is the angle between momentum of Higgs boson and initial electron. In the center of mass frame the cross section for the Higgs-strahlung process $e^- e^+ \to He^- e^+$ is equal to ($k_H = \sqrt{\omega^2 - M_H^2}$ is the momentum of Higgs boson);

$$\frac{d\sigma_a(e^- e^+ \Rightarrow He^- e^+)}{d\omega d\cos\theta} = \frac{\alpha^3 M_Z^2}{192\, x_w^3 (1-x_w)^3} k_H s f(\omega,\theta) \times$$

$$\times \left\{ (1-\lambda_1)(1+\lambda_2)\left[(1-h_1)(1+h_2)\left|F_{LL}^{(a)}\right|^2 + (1+h_1)(1-h_2)\left|F_{LR}^{(a)}\right|^2 \right] + \right.$$

$$\left. + (1+\lambda_1)(1-\lambda_2)\left[(1-h_1)(1+h_2)\left|F_{RL}^{(a)}\right|^2 + (1+h_1)(1-h_2)\left|F_{RR}^{(a)}\right|^2 \right] \right\}.$$

(17)

We see from (17) that there are four helicity processes for the Higgs-strahlung diagram a):

1) initial and final electrons are polarized left $(\lambda_1 = h_1 = -1)$ while positrons are right $(\lambda_2 = h_2 = +1)$:

$$\frac{d\sigma_a(e_L^- e_R^+ \to He_L^- e_R^+)}{d\omega d\cos\theta} = \frac{\alpha^3 M_Z^2}{12\, x_w^3 (1-x_w)^3} \cdot k_H s\left|F_{LL}^{(a)}\right|^2 f(\omega,\theta);$$

(18)

2) unitial and final electrons are polarized right $(\lambda_1 = h_1 = +1)$ while positrons are left $(\lambda_2 = h_2 = -1)$:

$$\frac{d\sigma_a(e_R^- e_L^+ \to He_R^- e_L^+)}{d\omega d\cos\theta} = \frac{\alpha^3 M_Z^2}{12\, x_w^3 (1-x_w)^3} \cdot k_H s\left|F_{RR}^{(a)}\right|^2 f(\omega,\theta);$$

(19)

3) unitial (final) electron is polarized left (right) while positron is right (left):

$$\frac{d\sigma_a(e_L^- e_R^+ \Rightarrow He_R^- e_L^+)}{d\omega d\cos\theta} = \frac{\alpha^3 M_Z^2}{12\, x_w^3 (1-x_w)^3} \cdot k_H s\left|F_{LR}^{(a)}\right|^2 f(\omega,\theta)$$

(20)

4) unitial (final) electron is polarized right (left) while positron is left (right):

$$\frac{d\sigma_a(e_R^- e_L^+ \Rightarrow He_L^- e_R^+)}{d\omega \cdot d\cos\theta} = \frac{\alpha^3 M_Z^2}{12\, x_w^3 (1-x_w)^3} \cdot k_H s\left|F_{RL}^{(a)}\right|^2 f(\omega,\theta).$$

(21)

When the initial $e^- e^+$-pair are polarized longitudinally the differential cross section for Higgs-strahlung process will be written by the following form (the summation is carried over the final electron and positron spiralities):

$$\frac{d\sigma_a(\lambda_1,\lambda_2)}{d\omega d\cos\theta} = \frac{\alpha^3 M_Z^2 k_H s}{48\, x_w^3 (1-x_w)^3} \cdot \frac{g_L^2 + g_R^2}{(s-M_Z^2)^2} \cdot \frac{f(\omega,\theta)}{(xs-M_Z^2)^2 + M_Z^2 \Gamma_Z^2} \times$$

$$\times [(1-\lambda_1)(1+\lambda_2) g_L^2 + (1+\lambda_1)(1-\lambda_2) g_R^2]. \tag{22}$$

2. The ZZ fusion mechanism.

The cross section that will be observed experimentally for the process $e^- e^+ \to He^- e^+$ will not be due to the Higgs-strahlung process only, but part of it will come from the ZZ fusion process $e^- + e^+ \to$ $\to Z^* + Z^* + e^- + e^+ \to H + e^- + e^+$. We now analyze the diagram b) corresponding ZZ bosons fusion. The transition amplitude of this diagram is given by:

$$M_b(e^- e^+ \Rightarrow He^- e^+) = -\left(\frac{e}{2\sin\theta_w \cdot \cos\theta_w}\right)^3 \times$$

$$\times M_Z \{ F_{LL}^{(b)} [\bar{u}(q_1,h_1)\gamma_\mu(1+\gamma_5)u(p_1,\lambda_1)] \times$$

$$\times [\bar{\upsilon}(p_2,\lambda_2)\gamma_\mu(1-\gamma_5)\upsilon(q_2,h_2)] + F_{RR}^{(b)}[\bar{u}(q_1,h_1)\gamma_\mu(1-\gamma_5)u(p_1,\lambda_1)] \times$$

$$\times [\bar{\upsilon}(p_2,\lambda_2)\gamma_\mu(1+\gamma_5)\upsilon(q_2,h_2)] + F_{LR}^{(b)}[\bar{u}(q_1,h_1)\gamma_\mu(1+\gamma_5)u(p_1,\lambda_1)] \times$$

$$\times [\bar{\upsilon}(p_2,\lambda_2)\gamma_\mu(1+\gamma_5)\upsilon(q_2,h_2)] + F_{RL}^{(b)}[\bar{u}(q_1,h_1)\gamma_\mu(1-\gamma_5)u(p_1,\lambda_1)] \times$$

$$\times [\bar{\upsilon}(p_2,\lambda_2)\gamma_\mu(1-\gamma_5)\upsilon(q_2,h_2)] \}, \tag{23}$$

where

$$F_{LL}^{(b)} = F_{RR}^{(b)} = D_1 D_2 g_L g_R,$$
$$F_{LR}^{(b)} = D_1 D_2 g_L^2, \qquad F_{RL}^{(b)} = D_1 D_2 g_R^2 \tag{24}$$

are the helicity amplitudes for the ZZ fusion diagram, the first and second index indicate the spiralities of initial (or final) electron and positron, and

$$D_1 = [(p_1-q_1)^2 - M_Z^2]^{-1}, \; D_2 = [(p_2-q_2)^2 - M_Z^2]^{-1}. \tag{25}$$

Let's calculate the square of amplitude

$$M_b(e^- e^+ \Rightarrow He^- e^+)_{II} = -\left(\frac{e}{2\sin\theta_w \cdot \cos\theta_w}\right)^3 M_Z F_{RR}^{(b)} \times$$

$$\times [\bar{u}(q_1,h_1)\gamma_\mu(1-\gamma_5)u(p_1,\lambda_1)] \cdot [\bar{\upsilon}(p_2,\lambda_2)\gamma_\mu(1+\gamma_5)\upsilon(q_2,h_2)].$$

$$\left| M_b(e^- e^+ \to He^- e^+)_{II} \right|^2 = \left(\frac{e^2}{4 x_w(1-x_w)}\right)^3 M_Z^2 (F_{RR}^{(b)})^2 X_{\mu\nu}^{(1)} X_{\mu\nu}^{(2)}, \tag{26}$$

where $X_{\mu\nu}^{(1)}$ and $X_{\mu\nu}^{(2)}$ are the tensors:

$$X_{\mu\nu}^{(1)} = tr[u(q_1, h_1)\bar{u}(q_1, h_1)\gamma_\mu(1-\gamma_5)u(p_1, \lambda_1)\bar{u}(p_1, \lambda_1)\gamma_\nu(1-\gamma_5)] =$$

$$= tr\left[\frac{1-h_1\gamma_5}{2}\hat{q}_1\gamma_\mu(1-\gamma_5)\cdot\frac{1-\lambda_1\gamma_5}{2}\hat{p}_1\gamma_\nu(1-\gamma_5)\right] =$$

$$= 2(1+\lambda_1)(1+h_1)[q_{1\mu}p_{1\nu} + p_{1\mu}q_{1\nu} - (p_1\cdot q_1)g_{\mu\nu} - i\varepsilon_{\mu\nu\rho\sigma}q_{1\rho}p_{2\sigma}],$$

$$X_{\mu\nu}^{(2)} = tr[\upsilon(p_2, \lambda_2)\bar{\upsilon}(p_2, \lambda_2)\gamma_\mu(1+\gamma_5)\upsilon(q_2, h_2)\bar{\upsilon}(q_2, h_2)\gamma_\nu(1+\gamma_5)] =$$

$$= tr\left[\frac{1+\lambda_2\gamma_5}{2}\gamma_\mu(1+\gamma_5)\cdot\frac{1+h_2\gamma_5}{2}\gamma_\nu(1+\gamma_5)\right] =$$

$$= 2(1+\lambda_2)(1+h_2)[p_{2\mu}q_{2\nu} + q_{2\mu}p_{2\nu} - (p_2\cdot q_2)g_{\mu\nu} + i\varepsilon_{\mu\nu\alpha\beta}p_{2\alpha}q_{2\beta}].$$

The product of tensors $X_{\mu\nu}^{(1)}$ and $X_{\mu\nu}^{(2)}$ gives:

$$X_{\mu\nu}^{(1)} X_{\mu\nu}^{(2)} = 2^4(1+\lambda_1)(1+\lambda_2)(1+h_1)(1+h_2)(p_1\cdot p_2)(q_1\cdot q_2).$$

The expression for the squared matrix amplitude is:

$$\left|M_b(e^-e^+ \Rightarrow He^-e^+)_{II}\right|^2 = \frac{1}{4}\cdot\left(\frac{e^2}{x_w(1-x_w)}\right)^3 M_Z^2 \times$$

$$\times\left|F_{RR}^{(b)}\right|^2(1+\lambda_1)(1+\lambda_2)(1+h_1)(1+h_2)(p_1\cdot p_2)(q_1\cdot q_2). \tag{27}$$

The integration over q_1 and q_2 is conveniently performed in the rest frame of the final leptons: $\vec{q}_1 + \vec{q}_2 = 0$ (see Fig. 2). In this frame we obtains:

$$d\sigma_a(e^-e^+ \Rightarrow He^-e^+)_{II} = \frac{1}{16s(2\pi)^5}\cdot\frac{d\vec{k}}{\omega}\int\left|M_b(e^-e^+ \Rightarrow He^-e^+)_{II}\right|^2 \times$$

$$\times\delta(p_1 + p_2 - k - q_1 - q_2)\frac{d\vec{q}_1}{\omega_1}\frac{d\vec{q}_2}{\omega_2} = \frac{1}{16s}\cdot\frac{1}{(2\pi)^4}k_H d\omega d\cos\theta\times$$

$$\times\int\left|M_b(e^-e^+ \Rightarrow He^-e^+)_{II}\right|^2\delta(E_1 + E_2 - \omega - 2\omega_1)d\omega_1 d\cos\theta_1 d\varphi_1 =$$

$$= \frac{1}{32s}\cdot\frac{1}{(2\pi)^4}k_H d\omega d\cos\theta\int_{-1}^{1}d\cos\theta_1\int_{0}^{2\pi}d\varphi_1\left|M_b(e^-e^+ \Rightarrow He^-e^+)_{II}\right|^2, \tag{28}$$

where $\left|M_b(e^-e^+ \Rightarrow He^-e^+)_{II}\right|^2$ can be written in the form:

$$\left|M_b(e^-e^+ \Rightarrow He^-e^+)_{II}\right|^2 = \frac{1}{4}\cdot\left(\frac{4\pi\alpha}{x_w(-x_w)}\right)^3 M_Z^2\cdot\frac{g_L^2 g_R^2}{[2(p_1\cdot q_1) + M_Z^2]^2}\times$$

$$\times\frac{s[s + M_H^2 - 2(k\cdot p_1) - (k\cdot p_2)]}{[s + M_H^2 - 2(k\cdot p_2) - 2(p_2\cdot q_1)]^2}(1+\lambda_1)(1+\lambda_2)(1+h_1)(1+h_2). \tag{29}$$

$\left| M_b(e^-e^+ \Rightarrow He^-e^+)_{II} \right|^2$ depend on φ_1 only through $(p_2 \cdot q_1)$:

$$(p_1 \cdot q_1) = \frac{1}{4}[s - 2(k \cdot p_1)](1 - \cos\theta_1),$$

$$(p_2 \cdot q_1) = \frac{1}{4}[s - 2(k \cdot p_2)](1 - \cos\theta_1 \cos\chi - \sin\theta_1 \sin\chi \cos\varphi_1),$$

where

$$\cos\chi = 1 - \frac{2s[s + M_H^2 - 2(k \cdot p_1) - 2(k \cdot p_2)]}{[s - 2(k \cdot p_1)][s - 2(k \cdot p_2)]}.$$

The integration over φ_1 and $\cos\theta_1$ can be analytically performed:

$$\frac{d\sigma_b(e^-e^+ \Rightarrow He^-e^+)}{d\omega d\cos\theta} = \frac{\alpha^3 M_Z^2}{4 x_w^3 (1 - x_w)^3} \cdot \frac{k_H}{s} \cdot \frac{1}{s_1 s_2 r} \{[(1 - \lambda_1)(1 + \lambda_2) \times$$

$$\cdot (1 - h_1)(1 + h_2)g_L^4 + (1 + \lambda_1)(1 - \lambda_2)(1 + h_1)(1 - h_2)g_R^4] \times$$

$$\times [4(1 + x_1)(1 + x_2)F_1 - F_2] + [(1 - \lambda_1)(1 - \lambda_2)(1 - h_1)(1 - h_2) +$$

$$+ (1 + \lambda_1)(1 + \lambda_2)(1 + h_1)(1 + h_2)] \cdot g_L^2 g_R^2 2(1 - \cos\chi)F_1\}, \qquad (30)$$
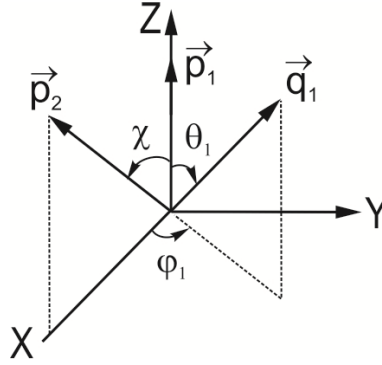

Fig. 2. The rest frame of the final leptons.

$$F_1 = \frac{1}{2x_1(1 + x_1)} + \frac{1}{2x_2(1 + x_2)} - \frac{6\sin^2\chi}{r} + \left(\frac{3t_1 t_2}{r} - \cos\chi\right)\frac{L}{\sqrt{r}}, \qquad (31)$$

$$F_2 = \frac{t_1}{x_2} + \frac{t_2}{x_1} + (t_1 + t_2 + \sin^2\chi)\frac{L}{\sqrt{r}}, \qquad (32)$$

$$s_1 = \sqrt{s}(\sqrt{s} - \omega + k_H \cos\theta), \quad s_2 = \sqrt{s}(\sqrt{s} - \omega - k_H \cos\theta),$$

$$t_1 = 1 + 2x_1 + \cos\chi(1 + 2x_2), \quad t_2 = 1 + 2x_2 + \cos\chi(1 + 2x_1),$$

$$\cos\chi = 1 - \frac{2xs}{xs + k_H^2 \sin^2\theta}, \quad \sin^2\chi = 1 - \cos^2\chi,$$

$$r = (1 + 2x_1)^2 + (1 + 2x_2)^2 + 2\cos\chi(1 + 2x_1)(1 + 2x_2) - \sin^2\chi,$$

$$L = \ln\frac{(1 + 2x_1)(1 + 2x_2) + \cos\chi + \sqrt{r}}{(1 + 2x_1)(1 + 2x_2) + \cos\chi - \sqrt{r}}, \quad x_1 = \frac{M_Z^2}{s_1}, \quad x_2 = \frac{M_Z^2}{s_2}.$$

We see clearly from (23) and (30) that there are four helicity processes for the *ZZ* fusion diagram b):

1) electrons are polarized left $(\lambda_1 = h_1 = -1)$ while positrons right $(\lambda_2 = h_2 = +1)$:

$$\frac{d\sigma_b(e_L^- e_R^+ \Rightarrow He_L^- e_R^+)}{d\omega d\cos\theta} = \frac{4\alpha^3 M_Z^2}{x_w^3(1-x_w)^3} \cdot \frac{k_H}{s} \cdot \frac{g_L^4}{s_1 s_2 r}[4(1+x_1)(1+x_2)F_1 - F_2]; \quad (33)$$

2) electrons are polarized right $(\lambda_1 = h_1 = +1)$ while positrons left $(\lambda_2 = h_2 = -1)$:

$$\frac{d\sigma_b(e_R^- e_L^+ \Rightarrow He_R^- e_L^+)}{d\omega d\cos\theta} = \frac{4\alpha^3 M_Z^2}{x_w^3(1-x_w)^3} \cdot \frac{k_H}{s} \cdot \frac{g_R^4}{s_1 s_2 r}[4(1+x_1)(1+x_2)F_1 - F_2]; \quad (34)$$

3) electrons and positrons are polarized left:

$$\frac{d\sigma_b(e_L^- e_L^+ \Rightarrow He_L^- e_L^+)}{d\omega d\cos\theta} = \frac{4\alpha^3 M_Z^2}{x_w^3(1-x_w)^3} \cdot \frac{k_H}{s} \cdot \frac{2g_L^2 g_R^2}{s_1 s_2 r} \cdot 2(1-\cos\chi)F_1; \quad (35)$$

4) electrons and positrons are polarized right:

$$\frac{d\sigma_b(e_R^- e_R^+ \Rightarrow He_R^- e_R^+)}{d\omega d\cos\theta} = \frac{4\alpha^3 M_Z^2}{x_w^3(1-x_w)^3} \cdot \frac{k_H}{s} \cdot \frac{2g_L^2 g_R^2}{s_1 s_2 r} \cdot 2(1-\cos\chi)F_1. \quad (36)$$

When the initial $e^- e^+$-pair is polarized longitudinally the differential cross section for the ZZ fusion process will be written as

$$\frac{d\sigma_b(\lambda_1,\lambda_2)}{d\omega d\cos\theta} = \frac{\alpha^3 M_Z^2}{x_w^3(1-x_w)^3} \cdot \frac{k_H}{s} \cdot \frac{1}{s_1 s_2 r} \times$$

$$\times \{[(1-\lambda_1)(1+\lambda_2)g_L^4 + (1+\lambda_1)(1-\lambda_2)g_R^4][4(1+x_1)(1+x_2)F_1 - F_2] +$$

$$+ [(1-\lambda_1)(1-\lambda_2) + (1+\lambda_1)(1+\lambda_2)]g_L^2 g_R^2 \cdot 2(1-\cos\chi)F_1\} \quad (37)$$

3. The interference between a) and b) diagrams.

It is interesting that the interference with a) and b) diagrams occur only between spirality processes $e_L^- e_R^+ \to He_L^- e_R^+$ and $e_R^- e_l^+ \to He_R^- e_L^+$ and we then have:

$$\frac{d\sigma_I(e_L^- e_R^+ \Rightarrow He_L^- e_R^+)}{d\omega d\cos\theta} = \frac{\alpha^3 M_Z^2}{x_w^3(1-x_w)^3} \cdot \frac{k_H}{s} \cdot \frac{2g_L^4}{(s-M_Z^2)[(xs-M_Z^2)^2 + M_Z^2\Gamma_Z^2]} \cdot g_I, \quad (38)$$

$$\frac{d\sigma_I(e_R^- e_L^+ \Rightarrow He_R^- e_L^+)}{d\omega d\cos\theta} = \frac{\alpha^3 M_Z^2}{x_w^3(1-x_w)^3} \cdot \frac{k_H}{s} \cdot \frac{2g_R^4}{(s-M_Z^2)[(xs-M_Z^2)^2 + M_Z^2\Gamma_Z^2]} \cdot g_I, \quad (39)$$

$$\frac{d\sigma_I(\lambda_1,\lambda_2)}{d\omega d\cos\theta} = \frac{\alpha^3 M_Z^2}{4x_w^3(1-x_w)^3} \cdot \frac{k_H}{s} \cdot \frac{2(xs-M_Z^2)}{(s-M_Z^2)[(xs-M_Z^2)^2 + M_Z^2\Gamma_Z^2]} \times$$

$$\times [(1-\lambda_1)(1+\lambda_2)g_L^4 + (1+\lambda_1)(1-\lambda_2)g_R^4] \cdot g_I, \quad (40)$$

where

$$g_I = 2 - 2(1+x_1)\ln\frac{1+x_1}{x_1} - 2(1+x_2)\ln\frac{1+x_2}{x_2} + 4(1+x_1)(1+x_2)\frac{L}{\sqrt{r}}. \quad (41)$$

CONCLUSION

The overall cross section for the process $e^-e^+ \Rightarrow He^-e^+$ receives contributions G_s from Higgs-strahlung, $G_Z^{(\pm)}$ from ZZ fusion, and G_I from the interference term between fusion and Higgs-strahlung:

$$\frac{d\sigma_0(e^-e^+ \Rightarrow He^-e^+)}{d\omega d\cos\theta} = \frac{\alpha^3 M_Z^2}{4x_w^3(1-x_w)^3} \cdot \frac{k_H}{s}[G_s + G_Z^{(+)} + G_Z^{(-)} + G_I], \qquad (42)$$

with

$$G_s = \frac{1}{12} \cdot \frac{(g_L^2 + g_R^2)s(2xs + k_H^2 \sin^2\theta)}{(s - M_Z^2)^2[(xs - M_Z^2)^2 + M_Z^2\Gamma_Z^2]},$$

$$G_Z^{(+)} = \frac{g_L^4 + g_R^4}{s_1 s_2 r}[4(1 + x_1)(1 + x_2)F_1 - F_2],$$

$$G_Z^{(-)} = \frac{2g_L^2 g_R^2}{s_1 s_2 r} \cdot 2(1 - \cos\chi)F_1, \qquad (43)$$

$$G_I = \frac{1}{2} \cdot \frac{(g_L^4 + g_R^4)(xs - M_Z^2)}{(s - M_Z^2)[(xs - M_Z^2)^2 + M_Z^2\Gamma_Z^2]} \cdot g_I.$$

Denoting by $d\sigma_{LR}$, $d\sigma_{RL}$, $d\sigma_{LL}$ and $d\sigma_{RR}$ the cross sections for $e_L^-e_R^+$, $e_R^-e_L^+$, $e_L^-e_L^+$ and $e_R^-e_R^+$ polarized, respectively, we obtains:

$$\frac{d\sigma_{LR}}{d\omega d\cos\theta} = \frac{\alpha^3 M_Z^2}{x_w^3(1-x_w)^3} \cdot \frac{k_H}{s}\left[\frac{g_L^2}{g_L^2 + g_R^2}G_s + \frac{g_L^4}{g_L^4 + g_R^4}(G_Z^{(+)} + G_I)\right],$$

$$\frac{d\sigma_{RL}}{d\omega d\cos\theta} = \frac{\alpha^3 M_Z^2}{x_w^3(1-x_w)^3} \cdot \frac{k_H}{s}\left[\frac{g_R^2}{g_L^2 + g_R^2}G_s + \frac{g_R^4}{g_L^4 + g_R^4}(G_Z^{(+)} + G_I)\right], \qquad (44)$$

$$\frac{d\sigma_{LL}}{d\omega d\cos\theta} = \frac{d\sigma_{RR}}{d\omega d\cos\theta} = \frac{\alpha^3 M_Z^2}{x_w^3(1-x_w)^3} \cdot \frac{k_H}{s} \cdot 2G_Z^{(-)}.$$

Since $g_R \approx -g_L$, the difference between $d\sigma_{LR}$ and $d\sigma_{RL}$ is however, strongly suppressed and we obtains;

$$\frac{d\sigma_{LR}}{d\omega d\cos\theta} = \frac{d\sigma_{RL}}{d\omega d\cos\theta} = \frac{\alpha^3 M_Z^2}{x_w^3(1-x_w)^3} \cdot \frac{k_H}{s} \cdot 2(G_s + G_Z^{(+)} + G_Z^{(-)}). \qquad (45)$$

The distributions of Higgs boson over angles is depicted in Fig.3 at the energy $\sqrt{s} = 500\ GeV$, Weinberg parameter $x_w = 0.232$, $M_H = 125 GeV$ and $\omega = 250 GeV$. We see from the Fig. 3a that as the angle of outgoing Higgs boson increase, the cross section also increase and reaches to its maximum at the value $\theta = 90^0$. By further increase of angle, the cross section starts to decrease.

In the ZZ fusion mechanism, as the angle of Higgs bosons increase, the cross section is decrease and reaches to its maximum at the value $\theta = 25^0$, by further increase of angle the cross section is decrease and reaches to its minimum at the angle 150°. Bu further increase of angle the cross section, also increase (see Fig. 3b).

One can that ZZ fusion cross section is dominant at a lower and at higher angles (the interference term is a very small in the over regions).
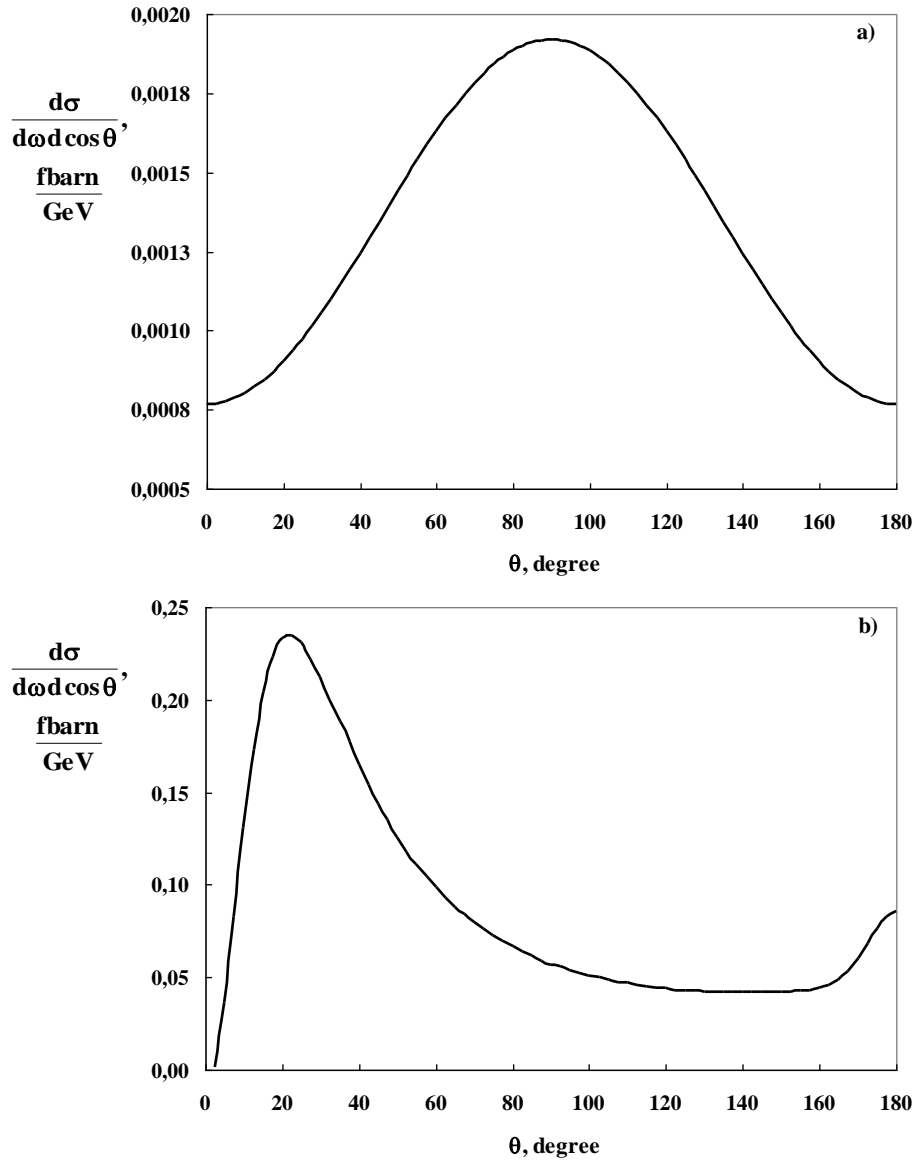
$$\frac{d\sigma}{d\omega\, d\cos\theta}, \quad \frac{fbarn}{GeV}$$

Fig. 3. The distributions of Higgs boson over angles for $\sqrt{s} = 500\ GeV$, $M_H = 125 GeV$, $\omega = 250 GeV$. The two components: Higgs-strahlung (Fig. 3a), ZZ fusion (Fig.3b).

_____

[1] ATLAS Collaboration. Observation of a new particle in the search for the Standard Model Higgs boson with the ATLAS detector at the LHC. Phys. Letters, B176, p. 1-29, 2012.

[2] ATLAS Collaboration. Phys. Review, D86, 032003-1-31, 2012.

[3] *Lenzi Bruno.* Measurement of properties of the Higgs boson in bosonic decay channels using the ATLAS detector. Proceedings of the Second Annual LHCP, ATL-PHYS-PROC-2014-135.

[4] *W.J. Marciano, C. Zhang, S. Willenbrock.* Higgs Decay to two photons, arXiv: 1109. 5304, v 2, 2011.

[5] *M. Sifman, A. Vainshtein, M.B. Voloshin., V. Zakharov.* Higgs decay into two Photons through the W-boson Loop; arXiv: 1109. 1785 v 3, 2011.

[6] *J. Ellis, M.K. Gaillard.* Nanopoulos D.V. A. Historical Profile of the Higgs boson; arXiv: 1201,

6045 v 1 , 2012.

[7] *S.Q. Abdullayev, M.Sh. Gojayev, F.A. Saddigh.* Azerbaijan Journal of Physics, Fizika, v. XX, N 2, p. 29-35, 2014.

[8] *Florian de D., G. Ferrera, M. Grazzini, D. Tommasini.* Transverse-momentum resummation: Higgs boson production at the Tevatron and the LHC; arXiv: 1109.2109 v 1, 2011;

[9] *W. Kilian, M. Kramer, P.M. Zerwas.* Higgs-strahlung and Ww fusion in $e^+ e^-$-collisions. DESY 95-216, hep-ph/9512355, D-22603 Hamburg/FRG, 1995.

[10] *G. Altarelli, B. Mele, F. Pitolli.* Nuclear Physics, B 287, p.205-224, 1987.

[11] *A. Djouadi.* The Anatomy of Electro-Weak Symmetry Breaking, tome I: The Higgs boson in the Standard Model; arXiv: hep-ph/050317 v2, 2005.

POLYMORPHOUS TRANSFORMATIONS AND THERMAL EXPANSION OF CRYSTAL LATTICE PARAMETERS OF SEPARATE MODIFICATIONS IN Ag$_{1.5}$Cu$_{0.5}$Se AND Ag$_{0.4}$Cu$_{1.6}$Se

U.G. ASADOV, A.G. BABAYEV, G.F. GANIZADE, B.I. ALIYEV

G.B. Abdullayev Institute of Physics of Azerbaijan NAS, Baku
AZ-1143, H. Javid, 131
E-mail: yusifasadov@rambler.ru

Ag$_{1.5}$Cu$_{0.5}$Se and Ag$_{0.4}$Cu$_{1.6}$Se are synthesized and the polymorphous transformations in them are investigated by method of high-temperature roentgenography. It is shown that FCC modification single crystals Ag$_{1.5}$Cu$_{0.5}$Se at temperature decrease lower 488K decompose on Ag$_2$Se and AgCuSe and Ag$_{0.4}$Cu$_{1.6}$Se lower than 540K decompose on Cu$_2$Se and AgCuSe.

The transformations in both compositions are reversible ones. From temperature dependence of lattice parameters of existing modifications the thermal expansion coefficients by main crystallographic directions are calculated.

Keywords: polymorphous transformations, roentgenography
PACS: 62.20.Fe, 61.50.Ks

INTRODUCTION

AgCuSe compound forms at ratio Cu$_2$Se:Ag$_2$Se=1:1 by peritectic reaction at temperature 1033K [1]. In [2] AgCuSe crystal structure is defined as tetragonal one with lattice parameters a=4.083 Å, c=6.300 Å, Z=2, sp.gr.D_{4h}^7 – *Pnmm*. Further, in [3] AgCuSe crystal structure is defined as rhombic one which is tetragonal lattice superstructure. The rhombic lattice parameter is equal to five parameters <u>b</u> of tetragonal lattice.

Ag atoms are in planes perpendicular to <u>c</u> axis in AgCuSe rhombic structure [3]. Four Ag atoms on distance 2.96Å and six Se atoms on distance 2.61Å (4Se), 3.59Å (1Se) and 3.64Å (1Se) locate round each of them. Se atoms form the prolate tetrahedrons in centers of which Cu atoms locate. The distance of Se-Se=3.03Å, Cu-Se=2.06-2.50Å and the smallest distance of Cu-Ag=2.98Å .

It is shown [4] that rhombic modification at 504K transforms into high-temperature FCC one with lattice parameter a=6.0823 Å. In given work the polymorphous transformations in AgCuSe single crystals are studied by method of high-temperature roentgenography and stability temperature intervals of existing modification stability are obtained.

The equilibrium temperature in triple compound AgCuSe, i.e. $^1/_2$(Cu$_2$Se, Ag$_2$Se) between modifications on 96K higher than one in Cu$_2$Se, Ag$_2$Se binary compounds.

It is important to note that lattice parameter values of low-temperature rhombic modification of AgCuSe approximately corresponds to lattice parameters of low-temperature rhombic modification of Cu$_2$Se. In Cu$_2$Se crystal structure Cu atoms are statistically distributed in tetrahedral voids formed by Se atoms, in AgCuSe structure Ag atoms locate in planes perpendicular to c axis and Cu atoms as well as in Cu$_2$Se locate in tetrahedron center formed by Se atoms. These structural differences and product additional bonds Cu-Ag and Ag-Se are also the reason of transformation temperature increase in AgCuSe (T$_{tr}$=504K) in comparison with Cu$_2$Se (T$_{tr}$=407K) and Ag$_2$Se (T$_{tr}$=408K).

Cu$_2$Se compound on Cu-Se state diagram exists in region 38,4 at.% Se [5,6]. The density of Cu$_2$Se is ρ=6.749 gr/cm^3 and melting point is T$_m$=1386K [7].

The rhombic structure with lattice parameters a=4.118Å, b=7.032Å, c=20.381Å (T$_{exp}$=293K) for low-temperature Cu$_2$Se is supposed in [7].

$\alpha \rightleftharpoons \beta$ transformations in Cu$_2$Se single crystals are investigated by roentgenographic and microscopic methods in [8-9]. It is established that low-temperature modification crystallizes in rhombic structure with lattice parameters a=4.119±0.001 Å, b=7.028±0.002 Å, c=20.394±0.003Å that confirms the investigation results of authors [7]. It is shown [8,9] that low-temperature rhombic modification at 407K transform into FCC one with lattice parameter a=5.840Å, Z=4, sp.gr. $\mathbf{O_h^5}$-Fm3m, ρ=6.838 gr/cm^3. The transformations are reversible ones and take place by single crystal – single crystal type.

As it is mentioned in [5,6] the silver with selenium form the one compound Ag$_2$Se which consists of 26.79 weight% Se. The scientific data on crystal structure of low-temperature modification of α-Ag$_2$Se are contradictory ones. The cubic structure in [10], the tetragonal structure in [11,12], the rhombic structure in [13,15], the monoclinic structure in [16,17] and triclinic structure in [18,19] are supposed for low-temperature modification.

The crystal structure of low-temperature modification is more detailed considered in [20,21]. The rhombic structure with lattice parameters a=7.05Å, b=7.85Å, c=4.33Å, Z=4, sp.gr.P222$_1$ is established in [20] by electronographic method for low-temperature modification of α-Ag$_2$Se. The rhombic structure with lattice parameters a=4.333Å, b=7.062Å, c=7.764Å, Z=4, sp.gr.P2$_1$2$_1$2$_1$ for low-temperature modification of Ag$_2$Se is supposed in [21]. In rhombic lattice Ag(I) is in tetrahedral surrounding of Se atoms and Ag(II) is in triangle surrounding of Se atoms. In sp.gr. P222$_1$ the damping conditions give the restricions only to reflection by (00l) type where *l=2n* and in sp.gr. P2$_1$2$_1$2$_1$ the damping conditions are the following ones: *(hkl)* is unrestricted, *(h00)-h=2n, (0k0)-κ=2n, (00l)-l=2n.* According to [21] data the

lattice parameter of high-temperature VCC modification is a=4.983Å, Z=2, sp.gr. O_h^5-Fm3m. The polymorphous transformations in Ag_2Se are investigated in detail and results are published in [24,25].

The structural changes at polymorphous transformations in compositions $Ag_{1.5}Cu_{0.5}Se$ and $Ag_{0.4}Cu_{1.6}Se$ where the cation number of Ag and Cu in AgCuSe are changed are studied in present work by method of high-temperature roentgenography.

EXPERIMENTAL PART

The synthesis of $Ag_{1.5}Cu_{0.5}Se$ and $Ag_{0.4}Cu_{1.6}Se$.

The synthesis conditions don't differ from AgCuSe ones [26]. By roentgen-phase analysis, it is shown that at room temperature the both compositions are two-phase ones. $Ag_{1.5}Cu_{0.5}Se$ consists of AgCuSe and Ag_2Se, $Ag_{0.4}Cu_{1.6}Se$ consists of AgCuSe and Cu_2Se, i.e. in both cases the high-temperature cubic phase decomposes in two phases at temperature lower than equilibrium one. By this reason, it is no possible to grow the low-temperature phases of these single crystals. The synthesized ingot in granular form is put in pointed ampoule, which provides the selection of high-temperature modification germs. The ampoules are evacuated up to pressure 10^{-3} Pa and located in upper furnace band and heated up to 1400K after what they are put down through the temperature gradient band with velocity 2mm/h. It is important to note that ampoule temperature becomes lower than melting temperature, the high-temperature modification crystals form and grow.

The low-temperature modification crystals form and grow with temperature decrease from high-temperature modification crystals. The density difference inside the matrix single crystal is the one from main factors influencing on new modification single crystallinity at growth of single crystals of new modification. The polymorphous substances can be divided on following three groups on density difference: a) the density of growing modification ρ_g is less than matrix crystal density ρ_m, i.e. $\rho_g< \rho_m$; b) the density of growing modification is bigger than matrix crystal density, i.e. $\rho_g > \rho_m$; c) the densities of growing crystal and matrix crystal are either equal or insignificantly differ, i.e. $\rho_g=\rho_m$, $\rho_g \geq \rho_m$ or $\rho_g\leq \rho_m$.

The matrix crystal deforms in transformation process at $\rho_g< \rho_m$, often cracks and each formed crack becomes the source of formation of many crystallization centers. As a result, the single crystal of high-temperature modification transforms into polycrystal of low-temperature phase. In $\rho_g > \rho_m$ case the contact between growing crystal and crystal-medium weakens and the distance of surface interface becomes bigger than interatomic distance. Moreover, the new phase crystal growth stops. The transformation process continues because of formation of more and more new germs. In this case, the single crystal also transforms into polycrystal. From such polycrystal, it is impossible to grow up the new crystal. In case $\rho_g \geq \rho_m$, $\rho_g\leq \rho_m$ and $\rho_g= \rho_m$ the two transformation types single crystal⇌single crystal and single crystal⇌polycrystal

are usually observed. Here single crystal⇌ polycrystal takes place at transformation with formation of many crystallization centers and because of matrix crystal imperfection. The single crystal of given modification can be obtained from such polycrystal.

The high-temperature diffractometric investigations of $Ag_{1.5}Cu_{0.5}Se$ and $Ag_{0.4}Cu_{1.6}Se$ compounds.

The high-temperature investigations are carried out on diffractometer ДРОН-3М (CuK_α radiation, λ_α=1.5418Å and Ni is filter) with attachment URVT-2000, providing the vacuum 10^{-2} Pa. The condition of recording resolution is ~0.1°. The error of angle of reflection definition doesn't succeed $\Delta\theta=\pm0.02°$.

1. $Ag_{1.5}Cu_{0.5}Se$.

27 diffraction reflections (table 1) are fixed at room temperature from $Ag_{1.5}Cu_{0.5}Se$ sample in the form of plane having sizes 4×5×1mm in angle interval $10\leq2\theta\leq90°$ at room temperature. For detail indexing of $Ag_{1.5}Cu_{0.5}Se$ diffraction data the experimental values of interplanar spacings d_i are compared with ones calculated on the base of crystal lattice parameters of AgCuSe, Ag_2Se and Cu_2Se low-temperature modifications.

As it is seen from table 1 experimental interplanar spacings d_i of $Ag_{1.5}Cu_{0.5}Se$ except of d=2.4812Å and d=1.8625Å satisfactory coincide with calculated values of interplanar spacings of Ag_2Se with parameters a=4.333Å, b=7.062Å, c=7.764Å. The above mentioned two interplanar spacings and also the series of others are indicated on the base of lattice parameters of rhombic modification of AgCuSe where a=4.105Å, b=20.350 Å, c=6.310A. In diffraction patterns, the change doesn't take place in temperature interval 293-423 K. At 423K in previous angle interval 14 reflections are fixed which also save diphase states. At temperature 488±1K all reflections disappear and in previous angle interval the four new reflections with (*200*), (220), (311) and (400) indexes are fixed which belong to high-temperature FCC modifications with lattice parameter a=6.107Å.

The temperature dependences of lattice parameter dependences of existing phases of $Ag_{1.5}Cu_{0.5}Se$ are given in fig.1. As it is seen from fig.1 the parameter values <u>a</u>, <u>c</u> of Ag_2Se and <u>a</u> of AgCuSe increase linearly in dependence on temperature and parameter <u>b</u> of Ag_2Se, parameters <u>b</u> and <u>c</u> of AgCuSe deviate from linearity.

2. $Ag_{0.4}Cu_{1.6}Se$.

The sample by 2×4×6 mm size is cut from $Ag_{0.4}Cu_{1.6}Se$ composition at room temperature. 18 sharp diffraction reflections (table 2) are fixed from this sample in angle interval $10°\leq26\leq110°$. As it is seen from table 2, 15 from 18 reflections are indicated on the base of AgCuSe rhombic modification parameters and 11 from 15 are indicated on the base of Cu_2Se rhombic modification parameters. It is followed that $Ag_{0.4}Cu_{1.6}Se$ composition is diphase one as well as $Ag_{1.5}Cu_{0.5}Se$ composition at room temperature.

Table 1.

$Ag_{1.5}Cu_{0.5}Se$ diffractogram calculation described at different temperatures.
Radiation CuK_α (λ_α=1,5418Å), Ni is filter, mode: 35 кV, 10 mA.

T_{exp},К	θ	I/I_0	D_{exp}, Å	Ag₂Se		AgCuSe		Crystal lattice parameters
				D_{calc}, Å	h к l	D_{calc}, Å	h к l	
1	2	3	4	5	6	7	8	9
295	11°27'	30	3.882	3.8820	002			
	11°46'	20	3.781	3.7836	101			
	13°22'	20	3.336	3.3351	111			
	13°52'	10	3.217	3.2142	021			
	16°22'	30	2.737	2.7372	120			
	16°45'	90	2.675	2.6758	112			Ag₂Se
	17°09'	90	2.614	2.6121	022			Orthorhombic
	17°23'	100	2.581	2.5815	121			a=4.333 Å
	18°06'	60	2.481	-	-	2.4828	112	b=7.062 Å
	18°30'	40	2.430	2.4300	013			c=7.764 Å
	20°09'	30	2.238	2.2370	122			Z=4
	21°20'	80	2.119	2.1194	113			sp.gr. P2₁2₁2₁
	21°51'	20	2.071	2.0712	210			ρ=8.237 gr/cm³
	21°53'	30	2.068	2.0685	130			
	22°31'	30	2.013	2.0128	032	2.0120	220	AgCuSe
	22°39'	45	2.002	2.0012	211			Orthorhombic
	24°27'	20	1.863	-	-	1.8640	113	a=4.105 Å
	25°03'	5	1.821	1.8255	132	1.8223	241	b=20.350 Å
	25°33'	10	1.787	1.7875	041	1.7875	063	c=6.310 Å
	26°39'	10	1.719	1.7182	114	1.7205	202	Z=10
	29°39'	10	1.558	1.5615	231	1.5589	024	sp.gr. P4/nmm
	31°45'	15	1.465	1.4618	105	1.4625	0.10.3	ρ=7.885 gr/cm³
	32°57'	10	1.417	1.4163	214	1.4113	243	
	33°54'	20	1.382	1.3823	143	1.3847	154	
	38°21'	10	1.242	1.2424	215	1.2468	0.10.4	
	39°35'	20	1.210	1.2099	243	1.2042	115	
	40°16'	20	1.193	1.1920	153	1.1911	2.10.3	
373	11°25'	30	3.893	3.8934	002			
	11°44'	20	3.791	3.7905	101			
	13°20'	20	3.343	3.3426	111			Ag₂Se
	13°50'	10	3.224	3.2241	021			Orthorhombic
	16°20'	30	2.744	2.7441	120			a=4.3396 Å
	16°42'	90	2.682	2.6822	112			b=7.0844 Å
	17°06'	90	2.622	2.6198	022			c=7.7868 Å
	17°20'	100	2.587	2.5880	121			Z=4
	18°03'	60	2.488	-	-	2.4838	112	ρ =8.175 gr/cm³
	18°28'	40	2.434	2.4376	013			
	20°07'	30	2.241	2.2428	122			
	21°18'	80	2.122	2.1253	113			
	21°49'	20	2.074	2.0748	210			
	21°51'	30	2.071	2.0743	130			

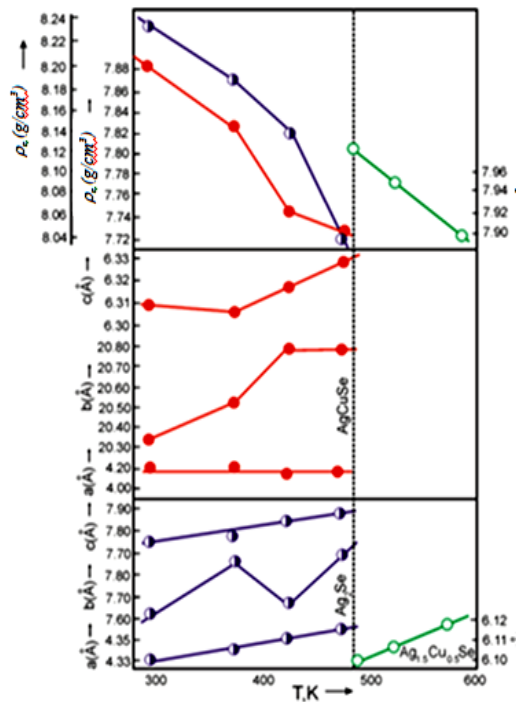| 1	2	3	4	5	6	7	8	9
	22°28'	30	2.017	2.0191	032	2.0150	220	
	22°37'	45	2.004	2.0048	211	-	-	
	24°24'	20	1.866	-	-	1.8640	113	
	25°00'	5	1.824	1.8306	132	1.8257	241	AgCuSe
	25°51'	10	1.768	1.7625	400	-	-	Orthorhombic
	26°36'	10	1.722	1.7229	114	1.7216	202	a=4.1100 Å
373	29°34'	10	1.562	1.5652	231	1.5585	024	b=20.4808 Å
	31°42'	20	1.467	1.4658	105	1.4669	0.10.3	c=6.3069 Å
	32°55'	10	1.417	1.4196	214	1.4120	243	Z=10
	33°52'	20	1.384	1.3864	143	1.3834	154	ρ =7.829 gr/cm^3
	38°18'	10	1.244	1.2455	215	1.2481	0.10.4	
	39°32'	20	1.211	1.2130	243	1.2037	115	
	40°14'	20	1.196	1.1956	153	1.1936	2.10.3	
	14°08'	20	3.157	-	-	3.1585	002	Ag$_2$Se
	15°20'	60	2.915	-	-	2.9148	150	Orthorhombic
	17°03'	80	2.629	2.6288	022	-	-	a=4.3540 Å
	18°06'	70	2.482	-	-	2.4815	112	5=7.0675 Å
	18°16'	80	2.459	2.4589	013	-	-	c=7.8688 Å
	21°07'	90	2.140	2.1408	113	2.1423	152	Z=4
	21°45'	20	2.081	2.0806	210	-	-	ρ =8.119 gr/cm^3
423	22°25'	60	2.021	2.0211	032	-	-	AgCuSe
	22°33'	100	2.0-10	2.0113	211	-	-	Orthorhombic
	24°21'	20	1.870	-	-	1.8644	113	a=4.0850 Å
	26°21'	10	1.737	1.7376	114	-	-	b=20.7973 Å
	29°31'	10	1.565	1.5667	231	1.5614	024	c=6.3170 Å
	31°24'	10	1.480	1.4799	105	1.4797	0.10.3	Z=10
	35°38'	10	1.323	1.3233	321	1.3233	2.10.2	ρ =7.744 gr/cm^3
	14°07'	20	3.165	-	-	3.1647	002	Ag$_2$Se
	15°18'	60	2.921	-	-	2.9161	150	Orthorhombic
	17°00'	80	2.637	2.6361	022	2.6481	151	a=4.3643 Å
	18°04'	70	2.486	-	-	2.4853	112	b=7.0781 Å
	18°14'	80	2.464	2.4678	013	-	-	c=7.8995 Å
	21°05'	80	2.143	2.1482	113	2.1447	152	Z=4, ρ=8.019gr/cm^3
473	21°42'	20	2.085	2.0851	210	-	-	AgCuSe
	22°22'	60	2.026	2.0257	032	-	-	Orthorhombic
	22°31'	100	2.013	2.0161	211	-	-	a=4.0902 Å
	24°18'	20	1.874	-	-	1.8676	113	b=20.7928 Å
	26°19'	10	1.739	1.7437.	114	-	-	c=6.3296 Å
	29°28'	10	1.567	1.5702	231	1.5642	024	Z=10
	31°22'	10	1.481	1.4856	105	1.4810	0.10.3	ρ=7.721 gr/cm^3
	35°36'	10	1.324	1.3268	321	1.3243	2.10.2	
	14°38'	60	3.053	3.0534	200			HCC
523	20°55'	80	2.159	2.1591	220			a=6.1068 Å
	24°45'	100	1.841	1.8413	311			Z=4, sp.gr.Fm3m
	30°19'	40	1.527	1.5267	400			ρ=7.95 gr/cm^3
	26°21'	60	3.058	3.0592	200			HCC
573	29°31'	80	2.164	2.1632	220			a=6.1184 Å
	31°24'	100	1.845	1.8448	311			Z=4, sp.gr.Fm3m
	35°38'	40	1.530	1.5296	400			ρ=7.90 gr/cm^3

Fig.1. The temperature dependence of crystal lattice
parameters and modification density of $Ag_{1.5}Cu_{0.5}Se$.
- • are a,b,c parameters of crystal lattice and density of $Ag_{1.5}Cu_{0.5}Se$
- ◖ are a,b,c parameters of crystal lattice and density of Ag_2Se
- ○ are a parameter and ρ_x density of FCC modification of $Ag_{1.5}Cu_{0.5}Se$.

The furnace is switched on after recording of diffraction reflections at room temperature not changing the sample orientation and every each 50K the control diffraction recordings are carried out. The sample temperature before the beginning of each recording is kept constant during 50 minutes. As it is seen from table 3 in temperature interval 293-523 K numbers and intensities of diffraction reflection changes don't change. At 573K all diffraction reflections disappear and in previous angle interval 7 new reflections belonging to high-temperature FCC modification with elementary cell parameter a=5.896 Å are fixed.

The equilibrium temperature between modifications is equal to 540±1K. The transformations are reversible ones and cubic modification decomposes on AgCuSe and Cu_2Se at temperature less than equilibrium one; both compositions have rhombic structure. The temperature dependences of lattice parameters of rhombic and FCC modifications of $Ag_{0.4}Cu_{1.6}Se$ are given in fig.2. As it is seen from fig.2. the parameters a and b of AgCuSe at 473 K deviate from linearity and parameter a of Cu_2Se strongly increases up to temperature 373K and further increases linearly up to transformation temperature. The parameter deviation from linearity of both rhombic phases mainly is connected with redistribution of

cation two types. The density temperature dependences of existing modifications are also shown in fig.2. The density difference presence of existing phases is the one of the instability reasons of compositions under consideration.
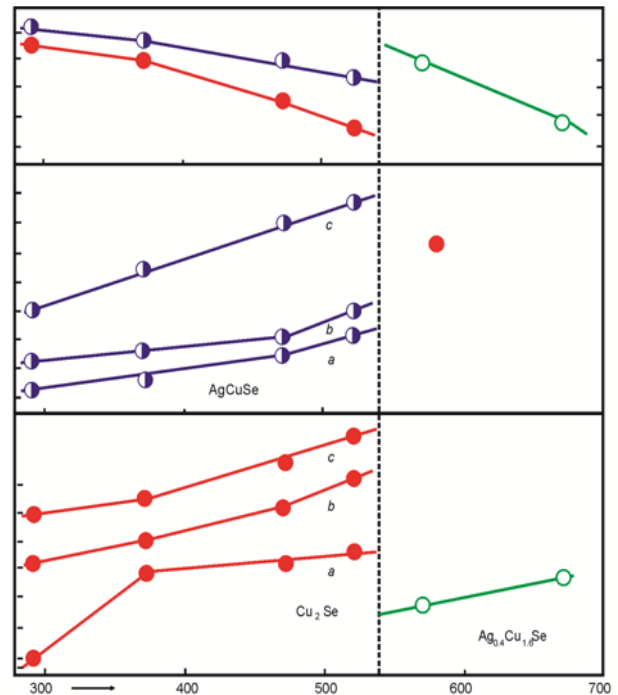

Fig.2. The temperature dependence of lattice parameters, volume and density of orthorhombic and FCC modifications of $Ag_{0.4}Cu_{1.6}Se$
- • are a,b,c parameters of crystal lattice and FCC modifications of AgCuSe
- ◖ are a,b,c parameters of crystal lattice and Cu_2Se density
- ○ are a parameter and ρ_x density of FCC modification of $Ag_{0.4}Cu_{1.6}Se$.

THERMAL EXPANSION OF LATTICE PARAMETERS OF POLYMORPHOUS MODIFICATIONS OF $Ag_{1.5}Cu_{0.5}Se$ AND $Ag_{0.4}Cu_{1.6}Se$.

The study of thermal expansion of pure chemical compounds by methods of high-temperature roentgenography is enough trivial task because the same questions are solved using dilatometric method by less difficulties and more accuracy. However, the possibility of investigation on micro-sample that is especially valuable at study of structural transformations is the advantage of high-temperature roentgenography method.

The study of thermal expansion anisotropy not only on single crystal samples but on polycrystalline ones and also the measurement of thermal expansion coefficient (TEC) in phase mixture can be carried out with the help of high-temperature roentgenography.

$Ag_{0.4}Cu_{1.6}Se$ diffractogram calculation described at different temperatures.
Radiation CuK_α (λ_α=1,5418 Å), Ni is filter, mode: 35 кV, 10 mA.

T_{exp},К	θ	I/I_0	D_{exp}, Å	CuAgSe		Cu$_2$Se		Crystal lattice parameters
				D_{calc}, Å	hкl	D_{calc}, Å	hкl	
1	2	3	4	5	6	7	8	9
	13°08'	60	3.3916	3.3917	060	-	-	AgCuSe
	15°28'	40	2.8916	2.8902	150	2.8939	024	Orthorhombic
	16°54'	50	2.6518	-	-	2.6512	121	a=4.102 Å
	18°05'	40	2.4836	2.4828	112	2.4881	123	b=0.362 Å
	20°19'	80	2.2203	2.2207	171	2.2158	033	c=6.292 Å
	21°12'	40	2.1296	2.1284	112	2.1295	034	Z=10
	22°15'	100	2.0362	2.0350	0.10.0	2.0371	130	sp.gr. P4/nmm
	24°39'	10	1.8484	-	-	1.8423	214	ρ=7.909 gr/cm
293	26°03'	90	1.7554	1.7560	260	1.7580	040	
	29°31'	10	1.5728	1.5739	173	1.5729	143	Cu$_2$Se
	30°40'	10	1.5122	-	-	1.5083	233	Oprthorhombic
	31°51'	30	1.4609	1.4625	0.10.3	-	-	a=4.137 Å
	35°09'	10	1.3390	1.3406	084,311	1.3370	240	b=7.022 Å
	39°57'	20	1.2006	1.2042	115,352	-	-	c=20.390 Å
	40°27'	20	1.1882	1.1876	135	1.1845	330	Z=12
	42°39'	10	1.1378	1.1309	333	1.1374	335	sp.gr. P222$_1$
	48°21'	10	1.0317	1.0323	314	-	-	ρ=6.930 gr/cm^3
	51°33'	10	0.9844	0.9823	460	0.9834	422	
	13°06'	60	3.4005	3.3993	060	-	-	AgCuSe
	15°26'	40	2.8959	2.8940	150	2.8939	024	Orthorhombic
	16°52'	50	2.6574	-	-	2.6512	121	a=4.106 Å
	18°03'	40	2.4884	2.4853	112	2.4881	123	b=20.389 Å
	20°16'	80	2.2255	2.2239	171	2.2158	033	c=6.295 Å
	21°19'	40	2.1202	-	112	2.1295	034	Z=10 sp.gr. P4/nmm
	22°13'	100	2.0389	2.0396	0.10.0	2.0371	130	ρ=7.886 gr/cm^3
	24°37'	10	1.8505	-	-	1.8423	214	
373	26°01'	90	1.7572	1.7571	260	1.7580	040	
	29°19'	10	1.5742	1.5760	173	1.5729	143	
	30°38'	10	1.5131	1.4651	0.10.3	1.5083	233	Cu$_2$Se
	31°49'	30	1.4623	-	-	-	-	Orthorhombic
	35°07'	10	1.3402	1.3428	084,311	1.3370	240	a=4.139 Å
	39°54'	20	1.2019	1.2056	115,352	-	-	b=7.029 Å
	40°25'	20	1.1891	1.1891	135	1.1845	330	c=20.434 Å
	42°36'	10	1.1389	1.1313	333	1.1374	335	Z=12 sp.gr. P222$_1$
	40°25'	10	1.0323	1.0329	314	-	-	ρ=6.904 gr/cm^3
	42°36'	10	0.9848	0.9840	460	0.9834	422	

1	2	3	4	5	6	7	8	9
	13°03'	60	3.4141	3.4088	060	-	-	AgCuSe
	15°23'	40	2.9058	2.9025	150	2.8939	024	Orthorhombic
	16°50'	50	2.6619	-	-	2.6512	121	a=4.114 Å
	18°00'	40	2.4948	2.4845	112	2.4881	123	b=20.421 Å
	20°14'	80	2.2293	2.2294	171	2.2158	033	c=6.300 Å
	21°16'	40	2.1254	-	112	2.1295	034	Z=10
	22°11'	100	2.0421	2.0453	0.10.0	2.0371	130	sp.gr. P4/nmm
	24°35'	10	1.8531	-	-	1.8423	214	ρ=7.851 gr/cm^3
	25°58'	90	1.7604	1.7631	260	1.7580	040	
	29°16'	10	1.5768	1.5758	173	1.5729	143	
473	30°35'	10	1.5154	-	-	1.5083	233	
	31°46'	30	1.4642	1.4652	0.10.3	-	-	Cu$_2$Se
	35°05'	10	1.3412	1.3411	084,311	1.3370	240	Orthorhombic, a=4.147 Å
	39°51'	20	1.2032	1.2030	115,352	-	-	b=7.042 Å
	40°22'	20	1.1911	1.1867	135	1.1845	330	c=20.572 Å
	42°34'	10	1.1395	1.1334	333	1.1374	335	Z=12 sp.gr. P222$_1$
	48°16'	10	1.0331	1.0338	314	-	-	ρ=6.832 gr/cm^3
	51°28'	10	0.9854	0.9854	460	0.9834	422	
	13°01'	60	3.4217	3.4221	060	-	-	AgCuSe Orthorhombic,
	15°21'	40	2.9124	2.9198	150	2.8939	024	a=4.121 Å
	16°49'	50	2.6647	-	-	2.6512	121	b=20.432 Å
	17°58'	40	2.4989	2.4942	112	2.4881	123	c=6.309 Å
	20°12'	80	2.2326	2.2398	171	2.2158	033	Z=10
	21°14'	40	2.1290	-	112 0.10.0	2.1295		sp.gr. P4/nmm
	22°10'	100	2.0432	2.0530	-	2.0371	130	ρ=7.822 gr/cm^3
				-	260	1.8423	214	
523	24°10'	10	1.8830	1.7630	173	1.7580	040	
	25°56'	90	1.7629	1.5809	-	1.5729	143	
	29°14'	10	1.5784	-	0.10.3	1.5083	233	Cu$_2$Se
	30°33'	10	1.5166	1.4695	084,311	-	-	Orthorhombic
	31°44'	30	1.4656	1.3443	115, 352	1.3370	240	, a=4.154 Å
	35°03'	10	1.3423	1.2057	135 333	1.1845	-	b=7.052 Å
	39°49'	20	1.2040	1.1895	314 460	1.1374	330	c=20.666 Å
	40°20'	20	1.1930	1.1403		0.9834	335	Z=12
	42°32'	10	1.1540	1.0392			-	sp.gr. P222$_1$
	47°07'	10	1.0521	0.9935			422	ρ=6.780 gr/cm^3
	50°11'	10	1.0036					
	15°10'	50	2.9469	2.9479	200			
	21°42'	30	2.0852	2.0845	220			FCC
	25°42'	45	1.7775	1.7777	311			a=5.8257 Å
573	26°56'	100	1.7021	1.7020	222			Z=4
	31°32'	60	1.4740	1.4740	400			sp.gr. Fm3m
	34°45'	40	1.3525	1.3526	331			ρ=7.258 g/cm^3
	35°47'	60	1.3182	1.3184	420			
	15°07'	50	2.9559	2.9516	200			
	21°39'	30	2.0897	2.0871	220			FCC
	25°40'	45	1.7795	1.7799	311			a=5.9063 Å
673	26°54'	100	1.7040	1.7041	222			Z=4
	31°30'	60	1.4754	1.4758	400			sp.gr. Fm3m
	34°42'	40	1.3541	1.3543	331			ρ=7.211 gr/cm^3
	35°45'	60	1.3196	1.3200	420			

TEC obtaining is made by differentiation (analytic or graphic) of equation for temperature dependence of parameters: $a=f(T)$ for cubic crystal lattice, $a=f(T)$ and $c=f(T)$ for hexagonal, tetragonal and rhombic ones, $a=f(T)$, $b=f(T)$, $c=f(T)$ for orthorhombic and etc. The crystal thermal expansion in given work is calculated from temperature dependence of elementary cell parameters in temperature interval enveloping all possible structural changes. The crystal elementary cell parameters change at increase of its temperature on ΔT. Let's designate the crystal elementary cell parameters by primed letters at change of its temperature on ΔT:

$$a'=a(1+\alpha_1\Delta T)$$
$$b'=b(1+\alpha_2\Delta T)$$
$$c'=c(1+\alpha_3\Delta T)$$

From these equations TEC by main crystallographic directions is as follows:

$$\alpha_{[100]} = \frac{a^1 - a}{a(T_2 - T_1)},$$

$$\alpha_{[010]} = \frac{b^1-b}{b(T_2-T_1)}, \quad \alpha_{[001]} = \frac{c^1-c}{c(T_2-T_1)}, \quad T_2>T_1.$$

Calculations of $Ag_{1.5}Cu_{0.5}Se$ diffractogram in temperature interval 295-573K enveloping all possible structural changes are given in table 1. TECs, which are given in table, are calculated from temperature dependence of lattice parameters of both rhombic and cubic phases. The anisotropy of thermal expansion on main crystallographic directions is the one of main reasons of temperature instability of crystal structure in which structure transformation with low symmetry into cubic structure having more high symmetry takes place and transformations are carried out by single crystal – polycrystal type. The crystal lattice parameters (table 2) of existing phases in composition $Ag_{0.4}Cu_{1.6}Se$ of thermal expansion coefficient calculated from temperature dependence are given in table 4. As it is seen from table 4, thermal expansion on crystallographic directions [100] and [010] is more strong than in [001] direction in AgCuSe structure. The strong anisotropy on main crystallographic directions is also one of the main reasons of temperature instability of crystal structure.

Table 3.

The thermal expansion coefficients of crystal $Ag_{1.5}Cu_{0.5}Se$ ($\times10^6K^{-1}$)

Modification	T, K	$\alpha_{[100]}$	$\alpha_{[010]}$	$\alpha_{[001]}$	$\bar{a} = \dfrac{\alpha_{[100]} + \alpha_{[010]} + \alpha_{[001]}}{3}$	$\beta = \alpha_{[100]} + \alpha_{[010]} + \alpha_{[001]}$
Ag_2Se	295-373	19.04	39.65	36.71	31.80	95.40
	295-473	37.28	5.99	103.83	49.03	147.10
	295-473	40.13	12.67	96.96	49.92	149.76
AgCuSe	295-373	15.23	80.34	-6.14	29.81	89.43
	295-423	37.48	169.08	8.53	71.70	215.09
	295-473	33.56	120.88	17.26	57.23	171.70
FCC	523-573	37.99			37.99	113.97

Table 4.

The thermal expansion of orthorhombic and FCC phase of $Ag_{0.4}Cu_{1.6}Se$ ($\times10^6K^1$) composition

Modification	T, K	$\alpha_{[100]}$	$\alpha_{[010]}$	$\alpha_{[001]}$	$\bar{a} = \dfrac{\alpha_{[100]} + \alpha_{[010]} + \alpha_{[001]}}{3}$	$\beta = \alpha_{[100]} + \alpha_{[010]} + \alpha_{[001]}$
Orthorhombic AgCuSe	293-373	20.194	47.791	1.610	23.198	69.595
	293-473	35.900	50.348	6.440	30.896	95.686
	293-523	91.311	67.723	-2.800	52.078	156.234
Orthorhombic Cu_2Se	293-373	6.043	12.460	26.974	15.159	45.477
	293-473	13.428	15.823	49.589	26.28	78.840
	293-523	1.866	19.809	58.852	32.10	96.519
FCC $Ag_{0.4}Cu_{1.6}Se$	573-673	17.979			17.979	53.937

CONCLUSION

In conclusion let's note that Ag cation number in $Ag_{1.5}Cu_{0.5}Se$ compositions is more than Cu one, that's why the high-temperature FCC modification decomposes on Ag_2Cu and AgCuSe ($T_0=488K$) at temperature lower equilibrium temperature. The Cu cation number in $Ag_{0.4}Cu_{1.6}Se$ composition is more than Ag one, that's why high-temperature FCC modification ($T_0=540K$) also decomposes on Cu_2Se and AgCuSe at temperature lower equilibrium temperature. The strong anisotropy of thermal expansion is also one of the main reasons of temperature instability of crystal structure in both compositions.

_____

[1] *M.N. Aqaev, Sh.M. Alekperova, M.I. Zarqarova.* DAN Azerb.SSR, 1971, t.27, №5, s.20. (In Russian).

[2] *I.W. Earley.* Amer. Mineralogist, 1950, 35, 5-6, p.337.

[3] *A.J. Frueh, G.K. Cramanske, C.H. Knight.* Z. Krist., 1957, v.108, p.389.

[4] *Sh.K. Kyazimov, G.Sh. Gasanov, Yu.G. Asadov.* DAN Azerb.SSR, 1986, t. 12, №11, s.33. (In Russian).

[5] *M. Hansen, K. Anderko.* Strukturi dvoynih splavov. M:, «Metallurgizdat», 1963, s.620. (In Russian).

[6] *F. Shank.* Strukturi dvoynih splavov. M:, «Metallurgizdat», 1973, s.759. (In Russian).

[7] *A.L.N. Stevels, F. Jellinek.* Rec. Truv. Chem., 1971, 90, №3, p.273.

[8] *Yu.G. Asadov*, G.A. Jabrailova. Neorganicheskie Materiali, 1972, t.8, №12, s.2208. (In Russian).

[9] *Yu.G. Asadov*, G.A. Jabrailova, V.I. Nasirov. Neorganicheskie Materiali, 1972, т.8, №12, с. 1144. (In Russian).

[10] *L.W. Constantinesch, A. Ichimesku.* Rev. Poum. Phys., 1973, V.18, № 10, p.1197.

[11] *A. Boettcher, S. Hanse, H. Treupel.* The Structures and Structural Changes in the Sulfides and Selenides of Silver and Copper. Z.Angew. Phys., 1955, v.7, p.478.

[12] *P. Junod.* Zones de Brillanin Lieksions Chimigues et Mude Conduction de Ag_2S et Ag_2Se. Helv., Phys. Acta, 1959, 32, p.581.

[13] *L.W. Constantinescu.* Thin Solid Films, 1983, 28, №l, p.73.

[14] *N. Nuruyev, R. Shafizade.* Neorganicheskie Materiali, 1972, 2, s.73. (In Russian).

[15] *K.P. Mamedov*. Kristallografiya, 1974, t. 19, v. 1, s. 174. (In Russian).

[16] *Do R. Ridder, S. Amelinckx.* Phys. Status Solidi, 1973, A18, p.99.

[17] *M.D. Banus.* Pressure dependence of the alpha-beta transition temperature silver selenides. Science, 1965, 147, p.732.

[18] *Y. Saito, M. Sato.* Thin Solid Films, 1981, 79, p.259.

[19] *J.R. Gunter, N. Uyeda, E. Suito* Crystal Growth, 1973, 33, p.337.

[20] *Th.L. Chjou, Z.G. Pinsker.* Kristallografiya, 1962, 7, s.66. (In Russian).

[21] *C.A. Wiegers.* Amer. Mineral., 1971, 56, p. 1882.

[22] Y. Beer, G. Buseh, C. Prohlich. Z.Naturforsch, 1962, 1701, p.886.

[23] *S.K. Sharma, C.A. Wiegers.* Amer. Mineral., 1971, 56, p. 1882.

[24] *Yu.G. Asadov, G.A. Jabrailova.* Phys. Stat. Sol., 1972, v(a), 12, K13.

[25] *Yu.G. Asadov, G.A. Jabrailova.* J. Crystal and Tech., 1973, v.8, №4, p.499.

[26] *R.B. Baykulov, Yu.G. Asadov.* Neorganicheskie Materiali, 2005, t.41, №4, s. 407. (In Russian).

THE INFLUENCE OF TEMPERATURE AND EXCITATION LEVEL ON PHOTOLUMINESCENCE SPECTRA OF $Ca(Al_{0.1}Ga_{0.9})_2S_4$:$Eu^{2+}$

B.G. TAGIYEV[1,3], O.B. TAGIYEV[1,2], S.A. ABUSHOV[1], E.G. ASADOV[1]

[1]*National Space Academy , Bina, Baku, AZ1045,25km*
[2]*The branch of MSU named by M.V.Lomonosov, Baku*
[3]*Institute of Physics of Azerbaijan NAS , AZ1143, Baku Azerbaijan*
E-mail:elsenesedov@gmail.com

The dependences of photoluminescence (PhL) spectrum intensity of $Ca(Al_{0.1}Ga_{0.9})_2S_4$:$Eu^{2+}$ crystals on temperature and excitation power are investigated. It is shown that PhL spectrum intensity decreases with temperature increase and it linearly increases in interval 2 – 10mW/cm^2 at temperatures 22 and 300K with increase of exciting radiation power.

Keywords: solid solutions, radiation spectrum, excitation, Eu^{2+} ions, power
PACS: 76.30.,78.55.,78.60.

EXPERIMENT TECHNIQUE INTRODUCTION

The perspective of creation of new class optoelectronic devices based on semiconductors doped by europium ions stimulates the intensive work in this direction in series of semiconductor centers. That's why investigation of europium ion photoluminescence in more perspective semiconductor matrixes for optoelectronic applications is the actual problem. The efficiency of optoelectronic devices based on semiconductor matrix doped by europium is defined firstly by energy transition efficiency on semiconductor matrix charge carriers into internal europium ion 4f-shell [1].

The study of luminescent properties of rare-earth elements (REE) in semiconductors and dielectrics gives the information on REE nearest surrounding, centers of symmetry of PhL and crystal field. The ternary alkali-earth chalcogenide semiconductors of II–III$_2$–VI$_4$ (II – Ba, Sr, Ca; III – Ga, Al; VI – S, Se, O) type activated by REE ions (Eu, Ce, Er, Yb, Pr, Sm) are perspective ones for use them in the capacity of luminophors [2-5].

The tiogallates of barium, strontium and calcium activated by Eu^{2+} ions are effective luminescent materials radiating in blue-green spectrum region caused by transitions 4f^{6}5d→4f^7 [6–11]. Last time the investigations of optical properties of mixed compounds MGa_2S_4–$M'Ga_2S_4$ (M, M' = Ba, Sr, Ca are alkali-earth elements) activated by REE ions in which matrix composition variation leads to shift of luminescence spectrum in visible region are carried out [12-14]. Such mixed compounds are new ones and their luminescence properties aren't investigated enough. The obtaining of mixed compound $Ca(Al_{0.1}Ga_{0.9})_2S_4$:$Eu^{2+}$ and investigation of temperature influence and exciting radiation power on spectra of its photoluminescence are the aim of present work.

EXPERIMENT TECHNIQUE

The chalcogenide wide-band semiconductors $Ca(Al_xGa_{1-x})_2S_4$:Eu^{2+}(**x=0.1**) are obtained by solid-phase reactions from binary compounds CaS, BaS and Al_2S_3 taken in stoichiometric ratios. The activation by Eu^{2+} ions up to 7at% is carried out by introduction into EuF_3 initial batch. The initial mixture of binary components is put into quartz ampoule evacuated up to 10^{-4} millimeter of mercury. The synthesis is carried out at 1100°C during one hour with following 4-hour annealing at 800°C.

The luminescence spectra are taken on spectrometer HR-460 (Jobin-Ivon SpectrometerHR 460). The continuous argon laser with power 10mW ($\lambda_{ex.}$=488nm) is used in the capacity of exciting radiation source. The synthesized samples are subjected by X-ray diffraction investigations on X-ray diffractometer D8 Advance (Bruker). The analysis of X-ray diffraction of compound $Ca(Al_{0.1}Ga_{0.9})_2S_4$ shows that it has the orthorhombic structure with space group $D_{2h}^{24} - Fddd$.

RESULTS AND DISCUSSION

$Ca(Al_{0.1}Ga_{0.9})_2S_4$:$Eu^{2+}$:7% solid solutions doped by europium ions have the intensive luminescence in green spectral region. Its PhL spectrum measured in temperature range 10–300K presents itself the wide band including the range of wave length 525-625 nm with maximum on 556 nm (fig.1) and caused by electron transitions $4f^65d→4f^7(^8S_{7/2})$ of Eu^{2+} ion.

The intensity of PhL spectra of $Ca(Al_{0.1}Ga_{0.9})_2S_4$:$Eu^{2+}$ decreases with temperature increasing in 10-300K interval, the half-width increases om law $\Gamma(T) \sim f(T^{1/2})$. At temperature 10K the maximum of wide-band spectrum takes place at 556nm and at temperature 300K it takes place at 554nm, i.e. the spectrum maximum shifts to the short-wave region with temperature increasing.

The temperature dependence of radiation band intensity with maximum on 556nm of $Ca(Al_{0.1}Ga_{0.9})_2S_4$:Eu: 7 % crystals in coordinates lg(I) and $10^3/T$ is shown in fig.2.

It is seen that in region 10-70K the intensity weakly depends on temperature and after 70K the intensity strongly decreases. lg(I) $\sim 10^3/T$ dependence in this temperature region is linear one. The activation energy of temperature damping of PhL which is equal to 0,03eV is defined by inclination of this dependence.
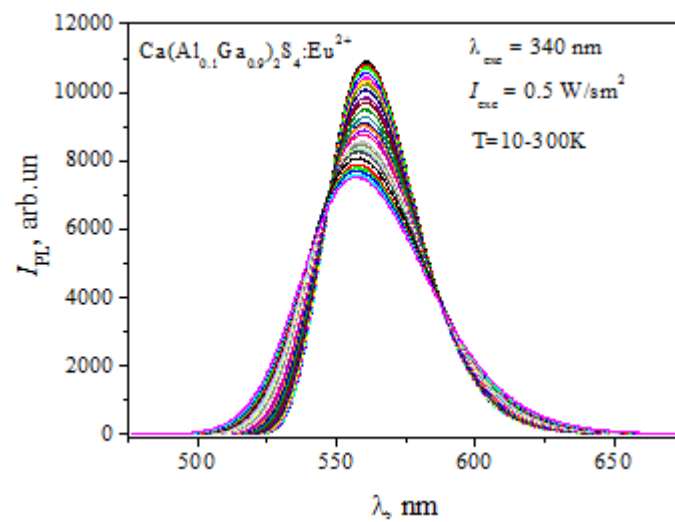
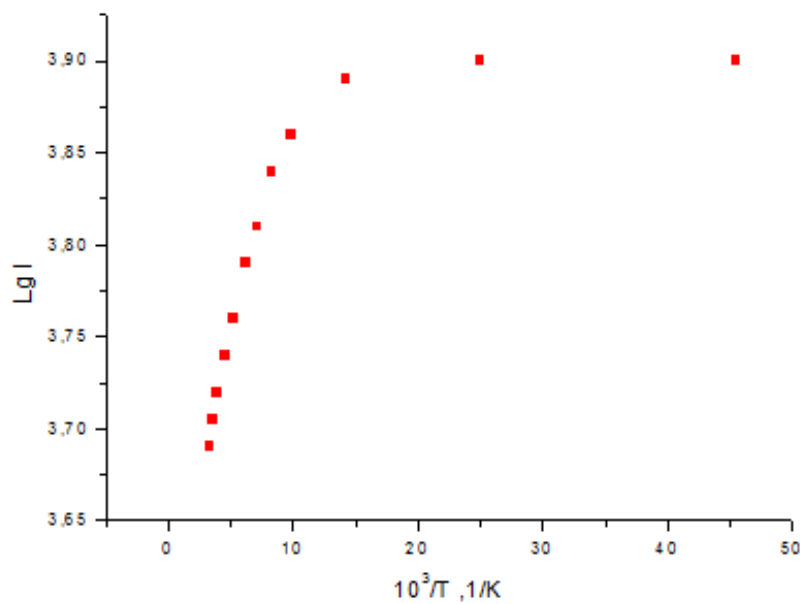*Fig. 1.* The temperature dependence of PhL spectra intensity of mixed compound $Ca(Al_{0.1}Ga_{0.9})_2S_4$:Eu^{2+}.

Fig. 2 The temperature dependence of luminescence intensity of mixed compound $Ca(Al_{0.1}Ga_{0.9})_2S_4$:Eu^{2+}.
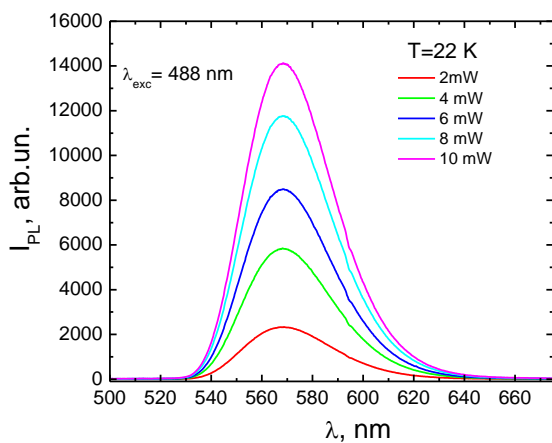

Fig.3a. The intensity dependence of PhL spectra of mixed compound $Ca(Al_{0.1}Ga_{0.9})_2S_4$:Eu^{2+} on excitation power at T=22K.
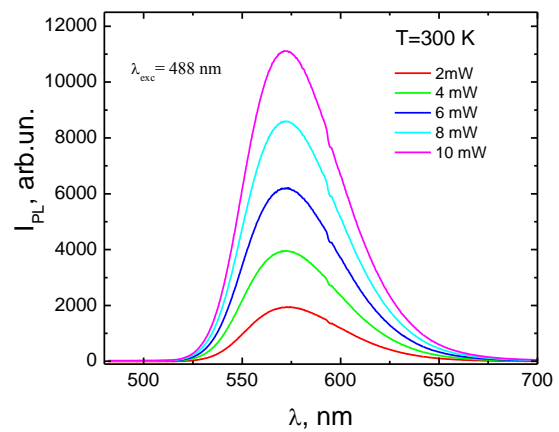
Fig. 3b. The intensity dependence of PhL spectra of mixed compound $Ca(Al_{0.1}Ga_{0.9})_2S_4$:Eu^{2+} on excitation power at T=300K.
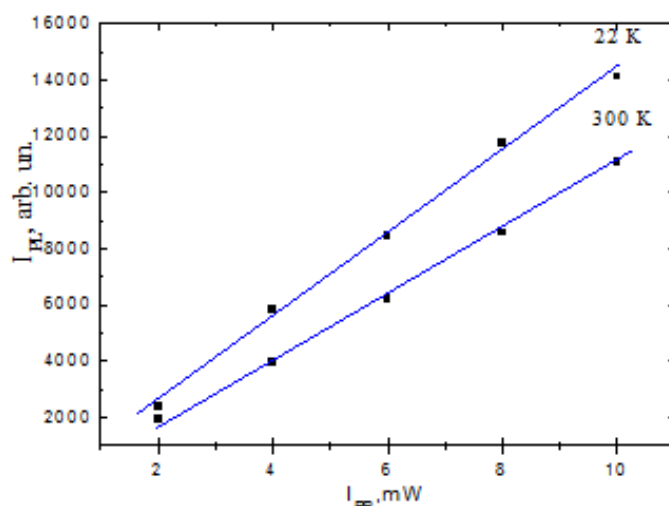
Fig. 4. The temperature dependence of luminescence intensity of $Ca(Al_{0.1}Ga_{0.9})_2S_4:Eu^{2+}$ mixed compound on excitation power.

The intensity dependences of PhL spectra on excitation luminecsence power $Ca(Al_{0.1}Ga_{0.9})_2S_4:Eu:7\%$ in 2-10mW/cm^2 are investigated at 20K and 300K temperatures. PhL spectra at 22K (fig.3a) and 300K (fig.3b) at different values of exciting radiation power are shown in fig.3. As it seen from the figure the radiation band intensities increase and energy positions of its maxima don't change at exciting radiation power increasing.

The intensity dependences of bands on exciting radiation power in double logarithmic scale is shown in fig.4. As it is seen from figure, the luminescence intensity linearly depends on excitation power [15].

CONCLUSION

The activating of mixed compound $Ca(Al_{0.1}Ga_{0.9})_2S_4$ by Eu^{2+} ions leads to wide-band intensive photoluminescence in spectrum green region which caused by transition $4f^65d\rightarrow4f^7(^8S_{7/2})$ of Eu^{2+} ion. The linear dependence of PhL spectrum intensity on excitation level is caused by thin solubility of europium ions in matrix and formation of isolated radiated centers.

_____

[1] *A.N. Qruzinchev, Q.A. Emelccchenko, Yu.V. Ermolaeva, V.M. Masalov, A.V. Tolmachev, C. Barthou.* Fizika tverdoqo tela, 2011, tom 53, vip. 9 P. 1795–1800. (In Russian).

[2] *S. Lahmann, F. Hitzel, U. Rossow, A. Hangleiter.* Phys. Stat. Sol. C. – 2003. – No. 7. – P. 2202–2205.

[3] *Akio Sasaki, Shinichiro Shibakawa, Yoichi Kawakami , et. al .* Jpn. J. Appl. Phys. – 2006. – V. 45. – No. 11. – P. 8719–8723.

[4] *E .Y. Lin , C.Y. Chen, T.S. Lay , et al .* Physica B. – 2010. – V. 405. – P. 1857–1860.

[5] *Teiji Yamamoto, Makoto Kasu, Susumu Noda , and Akio Sasaki.* J. Appl. Phys. – 1990. – V. 68. – No. 10. – P. 5318–5323.

[6] *B.G. Tagiev, O.B. Tagiev, T.Q. Naqiev, S.Q. Asadulleva, M.S. Leonenya, Q.P. Yablonskiy, S.A. Abushov.* Optika i Spektroskopiya, 2015, tom 118, № 3, s. 57–61. (In Russian).

[7] *P. Benalloul, C. Barthou, C. Foussier , A. N. Georgobiani, L.S. Lepnev, Y.N. Emirov, A. N. Gruzintsev, B.G. Tagiev, O.B. Tagiev, R. B. Jabbarov.* Journal of The Electrochemical Society, 2003, v.150, N1, pp. G62-G65.

[8] *P. Dorenbos.* J. Luminescence. 2003. V. 104. P. 239– 260.

[9] *V.Z. Zubelevich, E.V. Luchenko, A.V. Danilchik, E.V. Muravichkaya, Q.P. Yablonskiy, A.M. Pashaev, B.G. Tagiev, O.B. Tagiev, S.A. Abushov.* JPS. 2011. T. 78. № 2.S. 254–260. (In Russian).

[10] *B. Tagiev, R. Jabbarov, C. Chartier et al.* J. Phys. Chem. Sol. 2005. V. 66. № 6. P. 1049–1056.

[11] *SeishiIida, Tamao Matsumoto, Nazim T. Mamedov, GyejongAn, Yosuke Maruyama, Ayaz I. Bairamov, B.G. Tagiev, O.B. Tagiev, R.B. Dzhabbarov.* Jpn. J. Appl. Phys. 36 (1997) pp. L857-L859.

[12] *M. Nazarov, D.Y. Noh, H. Kim.* Materials Chemistry and Physics. 2008. V. 107. P. 456–464.

[13] *Ki-Young Ko, Young-Duk Huh, Young Rag Do.* Bull. Korean Chem. Soc. 2008. V. 29. P. 822–826.

[14] *Ruijin Yu, Jing Wang, Mei Zhang, Haibin Yuan, Weijia Ding, Yun An, Qiang Su.* J. Electrochem. Society. 2008. V. 155. № 10. P. J290–J292.

[15] *V.Z. Zubialevich, E.V. Lutsenko, M.S. Leanenia, G.P. Yablonskii, A.M. Pashaev, B.G. Tagiev, O.B. Tagiyev, E.V. Muravitskaya, S.A. Abushev.* Fizika, Vol. XVII, N2, p11-19 (2011).

NANOSTRUCTURED HYBRID OF PHOTOVOLTAIC SOLAR CELL WITH SUPERCAPACITOR AND ITS REALIZATION

SH.O. EMINOV[1], A.SH. ALIYEV[2], KH.D. JALILOVA[1], I. S. HASANOV[1], A.A. RAJABLI[1], N.J., ISMAYILOV[1], G.KH. MAMEDOVA[1], J.A. GULIYEV[1], I.I. GURBANOV[1]

Institute of Physics of NAS Azerbaijan[1], H.Javid ave.,33 AZ1143, Baku,Azerbaijan
Institute of Catalysis and Inorganic Chemistry of NAS Azerbaijan[2], H.Javid ave.,31, AZ1143,
Baku, Azerbaijan
e-mail shikhamirem@gmail.ru

The construction of the novel hybrid device comprises PV-cell and nanocapacitor which disposed on front and back sides on common glass substrate as well as the flow chart of the device's fabrication procedures are presented. For realizing the proposed device the anodic aluminum oxidation (AAO) nanostructures on basis of glass-ITO-Ti-Al thin film structure were synthesized . The method of electrochemical deposition of CdS thin film on ITO covered glass substrates. was developed. The optical microphotograph, SEM imaging, EDX spectra, optical transmission and Raman scattering data are presented.

1. INTRODUCTION

Solar energy represents one of the most abundant and yet least harvested sources of renewable energy. Because intermittent nature of solar energy, typical photovoltaic solar energy harvesting system includes both Photovoltaic (PV) cells which are often electrically connected and encapsulated as module and energy storage systems such as batteries or electrochemical capacitors (ECs).

In practice nearly all photovoltaic energy conversion uses semiconductor materials in the form of p-n- and hetero-junctions. Second generation solar cells are based on heterojunctions of thin layers of different semiconductor among which CdS/Cu$_2$S, CdS/CdTe, CdS/ CuInSe$_2$ (or CIS) combinations are the most promising solar cells are developed so far [1-4]. In such cells CdS -n-type semiconductor with band gap of ~2.5 eV is commonly used as a window layer, while CdTe was found to be a very suitable absorbing layer for solar cells due to its direct band gap of ~1.5 eV close to the optimum band gap for PVs. The CdS/CdTe based solar cells have reached an efficiency of 16.5% which is close to the predicted efficiency limit of 17.5%. This kind of solar cells has been used for a long time and still being widely used nowadays. However, due to a lot issues associated with the fabrication procedures of CdTe-CdS solar cells they are not much more efficient than silicon solar cells as we might expect.

Electrochemical capacitors that are also designated supercapacitors [5-9] derive their energy storage capacity from interaction between electrode and electrolyte at the interfacial region. Supercapacitors are currently a prominent area of research for energy storage devices as they have high power density, long cycling life, and short charging time [2-4]. Moreover, they have higher energy density than conventional dielectric capacitors . Supercapacitors can be used either alone as a primary power source or as an auxiliary one with rechargeable batteries for high-power applications, such as industrial mobile equipment and hybrid/electric vehicles.

In recent years, the novel characteristics of nanostructures such as nanowires, nanorods (NRs) and nanotubes (NTs) have attracted great attention from researchers in many fields such as electronics, optoelectronics and magnetism. In particular, the nanostructured PV-cells and nanocapacitor arrays have been intensively studied for the last generation of both energy harvesting and storage devices, sensors and optoelectronics [10,11].

As one of the most promising fabricating methods of nanowire arrays, the porous nanostructure templates including anodic alumina (AAO) templates are used widely. It's well known that during anodization of Al in certain acidic media (H$_2$SO$_4$, C$_2$H$_2$O$_4$ or H$_3$PO$_4$) a self organized, highly ordered array of cylindrical shaped pores can be produced in AAO film with controllable pore diameters, periodicity and ultrahigh density (~10^{10} cm^{-2}) distribution.

Vertically oriented NWs (or nanopillars, NTs) of CdS and CdTe, grown within templates of porous anodic alumina oxide (AAO) replaced the traditional thin film of those semiconductor materials in nanostructured PV-cells [12,13]

2. CONSTRUCTION AND FABRICATING STAGES OF THE HYBRID DEVICE

Almost all main fabrication steps used for manufacturing of nanostructured PV-cells and nanocapacitors are similar. Moreover, some of these steps are carried out under the same technological process conditions. Using a such a similarity of fabrication steps make we developed novel single hybrid device through combining PV-cell with the nanocapacitor by manufacturing them simultaneously on front and back sides of common glass substrate.
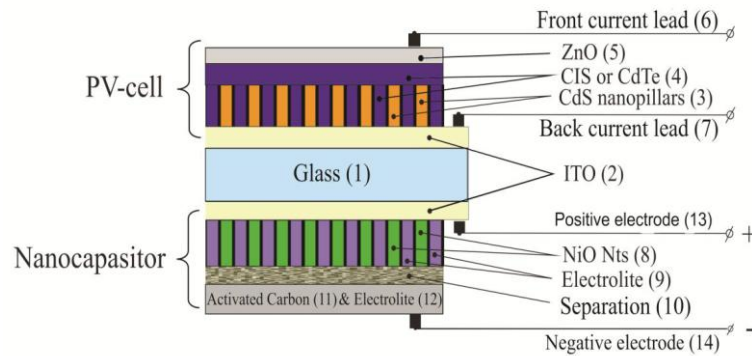
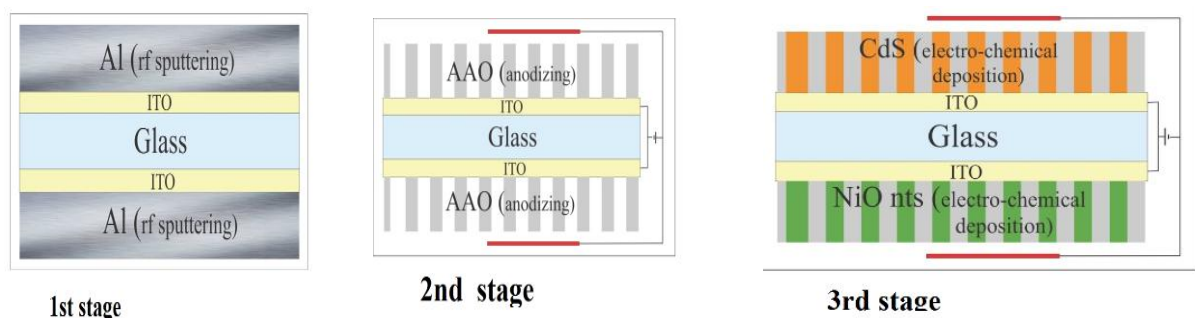*Fig. 1.* Shcheme of hybrid device.

Fig. 2. Fabrication stages of hybrid device.

The hybrid device comprises PV-cell and nanocapacitor which disposed on front and back sides on common glass substrate (1) covered with ITO layer (2) from front and back sides. The PV-cell part comprises of free standing CdS nanopillars (3) embedded in CdTe or CIS thin layer (4), transparent ZnO front layer (5), front and back current leads (6 and 7). The capacitor side comprises of free standing NiO nanotubes (positive electrode) (8) embedded in electrolyte (9), lead (10) to the positive electrode, activated carbon (negative electrode) (11) and electrolyte (12), porous separator between positive and negative electrodes (13) and lead (14) to the negative electrode. The flow chart of the device's fabrication procedures comprises the following stages: (Fig. 2, a, b, c)

Stage 1: fabrication Al-ITO-Glass-ITO-Al structure on both sides of glass wafer by magnetron sputtering.

Stage 2: Fabrication of AAO templates simultaneously on the both sides by Al anodic oxidation in electrochemical cell in oxalic or phosphorus or sulphuric acid;

The mechanism behind anodizing Al on substrates (particularly Si) is well documented. Briefly an Al-coated substrate (the anode) and an inert electrode (the cathode,e.g., Pt-mesh) are placed opposite to each other in a dilute acid and a constant electrical voltage is applied across the electrodes to effect anodization . Sulphuric,oxalic and phosphoric acids and voltages ranging from 25–200 V are routinely employed depending on the pore dimensions and spacing desired. As O_{-2} and OH_{-} ions diffuse to the Al surface, an Al_2O_3

anodization front is created. Because the Al_2O_3 at the anodization front is not perfectly smooth, the electric field in the sample concentrates at depressions in the Al_2O_3 layer. Due to higher local electric field and temperature, the Al_2O_3 formed at the depressions is preferentially dissolved resulting in the formation of pore channels as the anodization proceeds (Fig. 1(b)). When the anodization reaches the substrate, a thin inverted U-shaped barrier layer is formed (Fig. 1(c)).

Because the barrier layer is usually much thinner than the AAO pore walls, immersing the substrate in dilute phosphoric acid readily dissolves the barrier layer allowing connectivity to the substrate and also simultaneously enlarges the pore channels

Stage 3: Electrochemical growth of CdS nanorods and Ni nanotubes inside AAO templates.

Creating array of free standing CdS and Ni-nanopillars on front and back sides simultaneously by etching of AAO templates in 5% NaOH solution;.

Annealing of whole structure at 450°C in air;

Stage 4: Deposition of p-CdTe or p- CuInGaSe thin film with thickness of about 2- 5 mkm on PV-cell side either by magnetron sputtering or electrochemically for embedding CdS nano-columns within absorber layer.filing of the array of free standing NiO nanopillars (positive electrode) with electrolyte, installation of separation layer, installation of carbon nanoporous (negative) electrode and encapsulation; Deposition of ZnO front layer to to PV-cell; Fabrication of electrical contacts to the PV cell and to the electrodes of nanocapacitor;

In the PV-cell side of the proposed hybrid device the traditional thin film CdS window layer will be replaced by vertically aligned nanowire array of CdS. This array will be grown inside AAO template by electrodepositing. The positive electrode of the electrochemical capacitor will be a NiO nanostructure, whereas the negative one will be activated carbon. Non-aqueous electrolytes will chosen in order to push the range of voltage beyond 1V. This kind design of the device allows to combine several fabrication steps which usually applied for creation of an each device separately in one.

It is expected that the combination of fabrication processes steps would reduce the manufacturing costs of solar energy harvesting system. At the same time disposition of capacitor on the same substrate with PV-cell will lead to compactness of the whole system.

3. EXPERIMENTAL PROCEDURES AND CHARACTERIZATION

For realize the proposed device we synthesized AAO nanostructures on basis of glass-ITO-Ti-Al thin film structure by anodic oxidation in oxalic acid as well as developed method of electrochemical deposition of CdS thin film on ITO covered glass substrates.

Commercial glass slides covered by ITO layer sputtered by magnetron deposition used as working electrode, were ultrasonically cleaned in acetone. The electrolyte for CdS deposition was composed of 0.055M $CdCl_2$ and 0.19M elemental sulfur, dissolved in 50 mL dimethyl sulfoxide (DMSO).

The schematic diagram, optical microphotograph, plain-view SEM imaging, as well as EDX spectra of such structure are presented in Fig.3.

SEM images of a CdS thin film as well as EDX spectra of CdS deposited on the glass/ITO substrate are shown on the Fig.4a and Fig.4b, respectively. Optical analysis of CdS film samples with different thickness deposited over glass during different deposition duration was performed using optical transmittance spectra (Specord 210) at room temperature and at a the region from 1.0 to 4.0 eV.

The UV-visible spectrum and CdS thin film with thickness of 500 nm grown on glass/ITO substrate catholically deposited on glass/ITO substrate are shown in Fig. 5. We have determined the band gap of our samples by Tauc's formula to be as 2.42 eV which coincided with the dates reported earlier.

Raman spectrum of CdS thin film obtained in backscattering geometry by using confocal measurement system at room temperature [14] is shown on the Fig. 5. The sample is exhibit relatively sharp crystal-like peaks at 300 cm^{-1} and 600 cm^{-1} corresponding to the 1LO- and 2LO phonon modes ,correspondently . The FWHM (full-width half-maxima) of Raman peak at the 1 LO phonons was estimated to be 40 cm^{-1}.
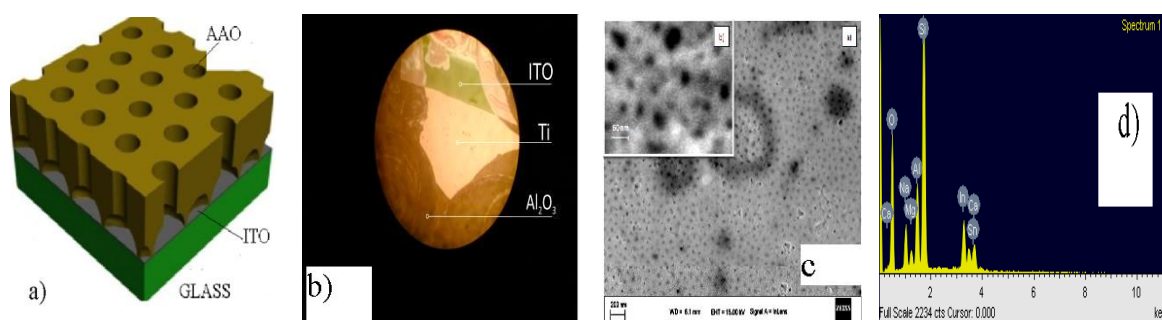

Fig. 3. The schematic diagram (a), microphotograph (b) , SEM imaging(c) and EDX spectra (d) of AAO film CdS thin films were characterized by various techniques like SEM, EDX, optical transmission and Raman spectroscopy.
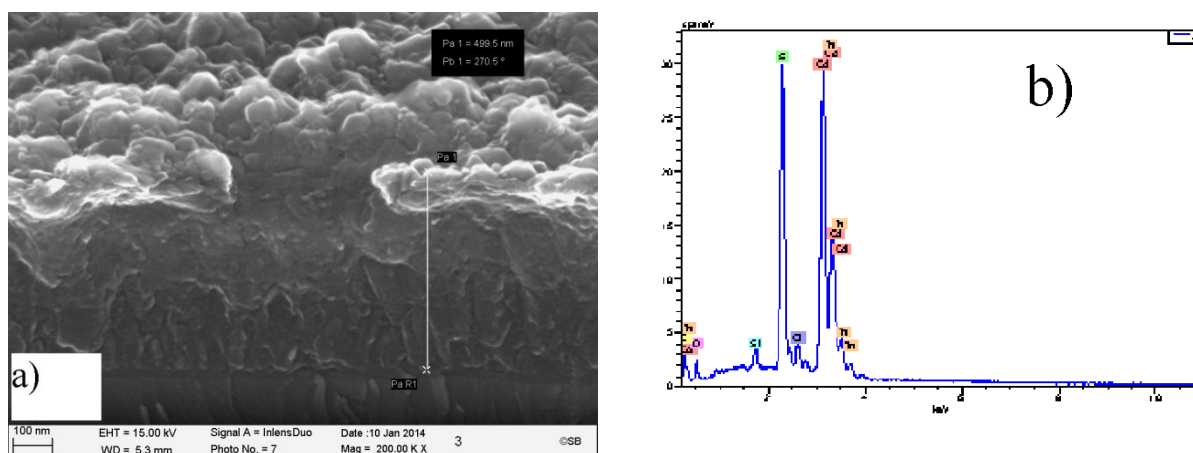

Fig. 4. SEM image of a CdS thin film cross-section (a) and EDX spectra of CdS deposited on the glass/ITO substrate (b).
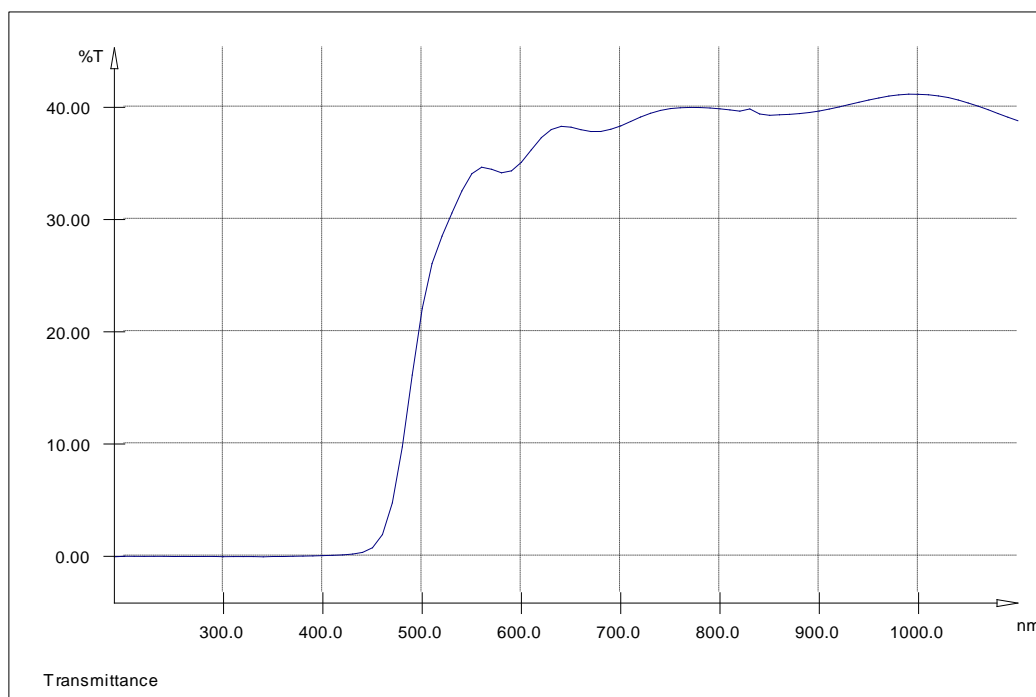
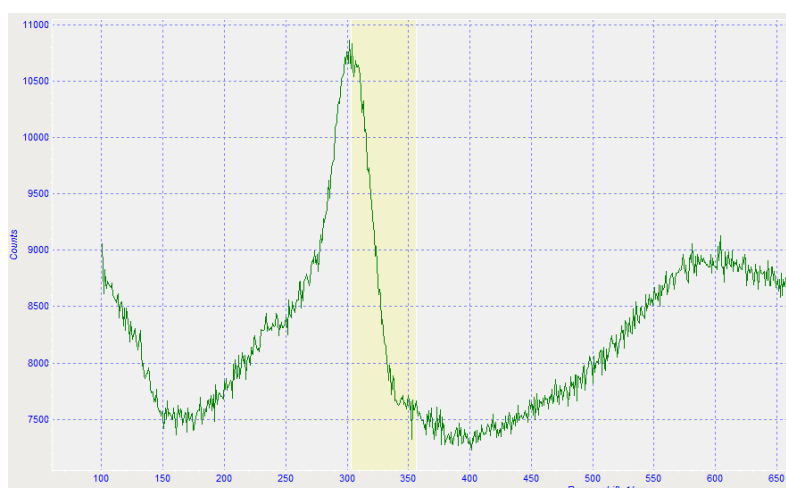*Fig 5.* The UV-visible spectrum of CdS thin film.

Fig.6. Raman scattering spectrum of CdS thin film.

4. CONCLUSION

In summary, the both proposed construction of the novel hybrid device comprises nanostructured solar cell and supercapacitor and the flow chart of the device's fabrication have been presented.

For realize the proposed device we synthesized AAO nanostructures on basis of glass-ITO-Ti-Al thin film structure by anodic oxidation in oxalic acid as well as developed the method of catholically deposition of CdS thin films on ITO covered glass substrates. The synthesized structures were characterized by using SEM, EDX, optical transmission, Raman spectroscopy .

_____

[1] *P. Jackson, et al.* New world record efficiency for $Cu(In,Ga)Se_2$ thin-film solar cells beyond 20%. Prog. Photovolt. Res. Appl. 19, 894- 897 (2011)

[2] *A Romeo, M. Terheggen* Development of Thin-film $Cu(In,Ga)Se_2$ and CdTe Solar Cells Prog. Photovolt: Res. Appl. 2004; 12:93–111.

[3] *A. Chirilă, P. Reinhard et al.* Potassium-induced surface modification of $Cu(In,Ga)Se_2$ thin films for

high-efficiency solar cells Nature Materials, 12,1107–1111 (2013).

[4] *P. Reinhard, et al.* Review of progress toward 20% efficiency flexible CIGS solar cells and manufacturing issues of solar modules. IEEE J. Photovolt. 3, 572–580 (2013) .

[5] *B.E. Conway.* Electrochemical Supercapacitors: Scientific Fundamentals and Technological Applications, Springer, 1999.

[6] *R. Kotz, M.Carlen.* Principles and applications of electrochemical capacitors Electrochimica Acta 45 (2000) 2483.

[7] *Sioe Yao Kan, M. Verwaal, H. Broekhuizen.* The use of battery-capacitor combinations in photovoltaic powered products J*ournal of Power Sources*, (2006), 162(2), 971-974.

[8] *Xu Wang, Chaoyi Yan, Afriyanti Sumboja, Pooi See.* High performance porous nickel cobalt oxide nanowires for asymmetric supercapacitor Nano Energy, 2014, 3 , 119.

[9] *F. Dar, K. Moonooswamy, M. Es-Souni.* Morphology and property control of NiO nanostructures for supercapacitor applications Nanoscale Research Letters, 2013, 8:363

[10] *T.L. Wade and J.-E. Wegrowe.* Template synthesis of nanomaterials Eur. Phys. J. Appl. Phys. (2005),29, 3.

[11] *G.E. Poinern, A. Nurshahidah, D. Fawcett.* Progress in Nano-Engineered Anodic Aliminum Oxide Membrane Development, Materials (2011), 4, 487-526.

[12] *Z. Fan, D.J. Ruebusch, A.A. Rathore, et al.* Challenges and Prospects of Nanopillar-Based Solar Cells ,Nano Research, 2009, 2, 829-843

[13] *Z. Fan, H. Razavi, J. Do, A. Moriwaki et al* Three-dimensional nanopillar-array photovoltaics on low-cost and flexible substrates, Nature Materials, 2009, 8, 648-653.

[14] *Ryo Asaba, Kazuki Wakita,Atsushi Kitano, Yong Gu Shim, Nazim Mamedov, Ayaz Bayramov, Emil Huseynov, Ilham Hasanov.* Structure and optical properties of CdS:O thin films Physica Status Solidi, C10 (2013) 1098-1101.

PHYSICAL PROCESSES IN WATER AT THERMAL AND ELECTRIC BREAKDOWN

E.J. GURBANOV

"Azersu" Open Joint Stock Company, Baku, Moscow av.67, Azerbaijan,
KurbanovEJ_mpei@mail.ru

Article to electronic and ion treatment of drinking water and sewage at impact of high-voltage pulses of various polarity and amplitudes for disinfecting from pathogenic microbes is devoted. It is shown that depending on amplitude of influencing pulse the vesiculate and electric breakdown of water with formation of high conductivity leader channels are observed. The physical processes happening in channel at its formation and collapse lead to death of bacteria and microbes containing in water medium. This technology can be partially or completely replace the existing chlorination process at inactivation of drinking water and sewage.

INTRODUCTION

Methods of electronic and ion treatment of various mediums for their activation and improvement of properties gain the highest interest in connection with the most real providing (with the smallest power losses) of the effective energy on activation processes recently. In this sense the choice of water medium has the certain advantages [1-4]. Water is the unique medium for transformation of one look in energy in another. In this context transformation of high electric energy in water in mechanical and use of this property in technologies of water purification from microorganisms is represented very tempting [5-8]. In this direction enough articles is published and uniqueness of physical processes in water at impact on medium of high voltage is shown. Application for this purpose of microsecond high voltage leads to development of various physical processes with the finishing breakdown of the medium [9-13].

The present article to the physical and mathematical description of the processes happening in water medium at influence of microsecond pulse tensions is devoted.

EXPERIMENTAL METHODS

As electrode system the "pin – plane" configuration was chosen. As the generator of pulse tensions the generator by Arkadyev-Marx's scheme with output voltage 10-100 kV was elaborated. Depending on tension amplitude, in interval between electrodes it was observed the vesiculate, thermal and electric processes of the water breakdown. Everyone them has the features and is applicable depending on characteristics of the treated medium and a problem definition. At first we will consider the physical processes happening in water at influence of microsecond pulses of low amplitude (less than 25 kV). In article will be considered discharge processes in water medium at impact on containing microorganisms by microsecond pulses. At voltage up to 25 kV, irrespective of its polarity, thermal processes, liquid boiling up, formation of gas inclusions with leader channels and thermal breakdown of discharge interval are observed. Thermal breakdown time – t_{br1} will consist of several components:

$$t_{br1} = t_d + t_i + t_l + t_f + t_r \tag{1}$$

where t_d - delay time; t_i - ionization time; t_l - leader's formation time; t_f - time of leader's final jump to opposite electrode; t_r - time of reverse discharge. As t_f and t_r are less than other parameters in (1), they can be neglected. At short interelectrode distance breakdown time only by delay time - t_d will be defined. Delay time - t_d will depend on tension polarity on potential "pin" electrode. At negative polarity and electric field intensity (< 85 kV/cm) delay time is much less than at positive one. It will be decreased from 900 μs at U=10 kV up to 2μs at U=100 kV. Change of tension polarity on potential electrode and field intensity in discharge interval influences also on leader's distribution speed. At negative polarity it is less than sound speed in water and makes ~ $5*10^4$ cm/s. By increase of field intensity (up to 350 kV/cm) at positive tension polarity on potential electrode an opposite situation is observed. The leader's distribution speed becomes more than sound speed in water and makes ~$5*10^6$ cm/s. Delay time of leaders appearance is decreased from 700 μs at U=10 kV up to 0,5 μs at U=100 kV in distance between electrodes - l=1-20 cm and radius of curvature of the "pin" electrode - r=0,2 cm.

At voltage over 25 kV thermal breakdown of water medium is replaced by electric one. At this moment spark discharge with followed leader channels and powerful mechanical compression waves are developing.

Will note that electric breakdown of water medium at both tension polarities on "pin" electrode comes to the end by crossing of leader channels the all interelectrode distance. In this case temperature and pressure in leader channel are reached up to $(3-4)\times10^4$ K and $(2 - 3)\times10^4$ atm respectively.

In technological installations better to use a positive voltage polarity on potential electrode for creation of powerful mechanical compression waves and dispersing liquid streams in water. The formula for definition of average breakdown time is given below:

$$t_{br2} = \frac{al}{(U-U_{min})^2} \tag{2}$$

where U – voltage between electrodes, a - constant coefficient (a = 3.6×10^5 V^2 s/m) on electric water conductivity - $\sigma = 2.5 \times 10^{-4}$ (Sm/cm); l - interelectrode distance (cm), $U_{min} = 18 \times 10^3 \times r \times \ln (4l/r)$ – minimum voltage, when leader is aroused and developed (kV); r - radius of curvature of "pin" electrode (mm).

Dependence of dissipated energy in discharge gap from distance between the electrodes– l is shown, that with increase in distance between electrodes the energy consumed from source is grow too.

Dependences of emitted energy in discharge gap from the radius of curvature and naked surface of potential "pin" – electrode is shown, that with increase of geometrical parameters of "pin" – electrode an emitted energy in discharge gap is grow too.

For determination of the energy losses and other parameters during breakdown process in discharge gap at positive tension polarity on the "pin" electrode the following expression is used:

$$W_l = \left[CU_1^2 \left(1 - \frac{U_{br}^2}{U_1^2}\right) \middle/ ab\omega + \frac{4\pi S}{b^2} \right]^{1/2} - 2\frac{\sqrt{\pi S}}{b} \quad (3)$$

where C – capacity of condenser battery; U_1 – charging voltage of condenser; U_{br} – breakdown voltage; S – surface of naked electrode in water; $b = 2 * 10^{-4}U_1$.

Maximal length between electrodes – l, on which the energy losses are minimal can be defined from the following expression:

$$l = 8 * 10^{-9} * U_{br}^{3/2} * \left(\frac{C}{L}\right)^{0,25} \quad (4)$$

where U_{br} – breakdown voltage, C - capacity of condenser battery, L - inductance of the discharge circuit.

RESULTS AND DISCUSSION

Thus, results of our researches testify to interference of the main parameters of high-voltage installation of technological appointment at each other. Depending on tension amplitude and intensity of electric field in discharge interval thermal and electric breakdown of water medium can be observed.

At voltage less 25 kV thermal processes, followed by boiling of water, formation of gas inclusions and leader channels there are taken place. Temperature and pressure in gas inclusions are very high and leads to their expansion and cooling. At the moment when pressure inside of inclusion is less than surrounding hydrostatic one, it collapses and promotes formation of weak mechanical compression waves in medium. Physical processes of formation and collapse of gas inclusions at influence of high pulse electric fields are repeated with a certain frequency, thereby perniciously influencing activity of microorganisms there. It should be noted, that more notable reduction of delay time at negative tension polarity on potential "pin" electrode is related with prevalence of ionization processes around it as a result of increase of electric field intensity.

At voltage over 25 kV breakdown process is also begun with water boiling up, discharges in gas inclusions and formation of the high conductivity leader channels. Difference of these processes from described above is that breakdown of discharge interval in this case happens due to short circuit of the distance between electrodes by leader channels, i.e. the spark discharge. As a result of expansion and collapse processes in gas inclusions under influence of high pressure and temperature, the powerful shock waves and a bright ultra-violet luminescence are formed in water, which are also perniciously influencing on microorganisms.

At "pin-pin" electrode system in discharge interval a crown discharge is arousing and gives rise to the origin and development of the negative high conductivity leader channel, moving to an opposite "pin" electrode. After some time at opposite "pin" electrode the positive crown discharge is arousing. Breakdown of discharge interval comes to the end with meeting of the negative leader channels and positive crown. At further increase in tension near anode positive leader channels are formed (besides a crown) and breakdown between electrodes comes to the end with a meeting of opposite directed leaders.

CONCLUSIONS

Thus, in article the physical processes happening at thermal and electric breakdown of water medium are described, the main dependence ratios of the unit electric parameters on medium characteristics and parameters of electrode system are given. It is shown, that at elaboration of high-voltage pulse installations the accounting of the pulsed generator parameters and a discharge interval is necessary.

It is revealed, that depending on pulse amplitude are possible thermal (vesiculate) or electric breakdown of the medium. In both cases there is breakdown of interelectrode distance be followed by some physical processes (formation of shock mechanical compression waves, ultra-violet radiation, thermo ionization and etc.), perniciously influencing on activity of the microorganisms containing there.

Considering that recently the huge attention to development of ecologically safe technologies, this method of disinfecting drinking water is paid and sewage can successfully replace (partially or completely) chlorination process for disinfecting of the noted mediums.

---

[1] *Yu.V. Gorin, F.H. Kulakhmetov, E.J. Gurbanov.* Modification of composite materials surface in torch discharge. Electronic Treatment of Materials, Moldova, 1991, № 3, p. 48.

[2] *E.J. Gurbanov.* The combined treatment of fiber glasses surface by no equilibrium electric discharges in fiberglass production technology. MPEI bulletin, №. 3, Moscow, 2009, p. 42-46.

[3] *E.J. Gurbanov.* Modification of fiber glasses surface in barrier electric discharge in fiberglass's production process. Electricity, Moscow, №. 2, 2009, p. 32.

[4] *Yu.N. Vershinin, A.M. Gashimov, E.D. Gurbanov.* Role of electron escape in pulsed dielectric breakdown., Surface Engineering and Applied Electrochemistry, № 6, USA, 2005. p.70-73

[5] *E.J. Gurbanov.* Environmentally clear methods of water disinfection. IJTPE, Issue 18, Vol.6, №1, 2014, p. 34-38

[6] *E.J. Gurbanov.* "Thermal and electric breakdown of water at crown and spark discharges". IJTPE, Issue 19 , Vol.6, № 2, 2014, p. 88-93

[7] *E.J. Gurbanov.* Influence of parameters of the electrode design on a luminescence form of the pulsed discharges in overvoltage gaps. IJTPE, Issue 23 , Vol.7, № 2, 2015, p. 49-54

[8] *E.J. Gurbanov.* Plasma processes in water under effect of short duration pulse discharges. The 66-th Annual Gaseous Electronics Conference GEC-2013, Princeton (USA), Vol. 58, № 8, p. 47.

[9] *E.D. Kurbanov, I.P. Kuzhekin, A.M. Hashimov, A.S. Bondyakov.* The physical processes in water by effect of high voltage short front pulses. The 5-th International conference on technical and physical problems of power engineering TPE-2009, Spain, p. 245

[10] *E.J. Gurbanov.* Water purification by influence of high voltage pulsed discharges. Materials of the 1-st International Conference on Caspian Aqua Technologies, Baku, 2013, p. 264-266.

[11] *E.J. Gurbanov.* Crown and spark discharges in water. The 9-th International conference on technical and physical problems of electrical engineering TPE-2013, Istanbul (Turkey), p. 501-503

[12] *P. Kuzhekin, E.J. Kurbanov.* Pulsed discharge in water. Problems in Power Engineering. № 1, 2008, p. 103.

[13] *P. Kuzhekin, E.J. Gurbanov.* High electric fields and pulse discharges in water Bulletin of MPEI, № 2, 2008, p. 3.

SYNTHESIS AND CHARACTERIZATION OF MULTIWALL CARBON NANOTUBE - HEXAMETHYLENEDIAMINE - MALEIC ANHYDRIDE - 1-HEPTENE NANOCOMPOSITE

E.Y. MALIKOV[*], O.H. AKPEROV, M.B. MURADOV, G.M. EYVAZOVA

Baku State University, Z.Khalilov str.,23, Baku, Azerbaijan AZ – 1148,
[*]E-mail: bsuc@hotmail.com

The multiwalled carbon nanotubes synthesized by Chemical Vapor Deposition over an Fe-Co/alumina catalyst were oxidized and grafted with maleic anhydride-1-heptene copolymer via the "grafting to" approach using hexamethylenediamine bridge. The obtained nanocomposite was characterized by Raman spectroscopy, XRD, FTIR, SEM and TEM methods. FTIR confirmed the presence of the characteristic peaks of the anticipated zwitterion and amine-amide conversion. The completion of the grafting process was also confirmed by XRD and Raman spectroscopy. Microstructure images of the nanocomposite obtained by TEM and SEM revealed that the nanotubes are uniformly covered with the polymer which shows the effectiveness of the method. Whole the process proceeds at room conditions which is the main advantage of this method.

1. INTRODUCTION

Carbon nanotubes (CNTs) have received considerable attention recently owing to their unique electronic and mechanical properties that are expected to lead to breakthrough industrial applications. They can be synthesized by chemical vapor deposition (CVD) [2-4], laser ablation [2,5-7] and d.c. arc discharge [2,6-8]. Among these techniques, CVD has inherent advantages such as better control over process parameters and good scalability [9].

CNTs exhibit a well-known tendency to form agglomerates due to van der Waals forces, which makes them extremely difficult to disperse and align in a polymer matrix. Thus, a significant challenge in developing high performance polymer/CNTs composites is to introduce the individual CNTs into a polymer matrix in order to achieve better dispersion and alignment, promote strong interfacial interactions and improve load transfer across the CNT-polymer matrix interface. The functionalization of CNTs is an effective way to prevent nanotube aggregation, which helps in dispersing and stabilizing carbon nanotubes within a polymer matrix. There are several approaches towards CNT functionalization including defect functionalization, covalent functionalization and non-covalent functionalization [10, 11].

The functionalization of carbon nanotubes can improve their solubility as well as dispersion properties in solvents and in polymers. Covalent functionalization can be carried out either by the modification of surface-bound carboxylic acid groups or by directly attacking the sidewalls of nanotubes. Usually, functional groups such as -COOH or -OH are formed on the CNTs during oxidation by oxygen, air, concentrated sulfuric acid, nitric acid or aqueous hydrogen peroxide [12,13]. Acid treated multiwall carbon nanotubes (MWCNTs) have defects in the carbon-carbon bonds. The number of functional groups on the nanotube surface depends on acid treatment temperature and time, increasing with increasing temperature [14]. Nanotube end caps can be opened as the result of oxidation process [11]. The presence of

carboxylic groups on the CNT surface is advantageous from the synthetic chemistry point of view because a variety of chemical reactions can be conducted with this group. The -COOH and -OH groups on the nanotube surface help the attachment of organic or inorganic materials, which is important for solubilizing nanotubes [15,16]. Functionalization of CNTs with polymer molecules (polymer grafting) is particularly important for obtaining polymer/CNT nanocomposites [17,18].

The two main pathways suggested for the covalent grafting of polymers to CNTs are the "grafting from" and the "grafting to" approaches. In the "grafting from" approach, the polymer is bound to the CNT surface by in-situ polymerization of monomers in the presence of reactive nanotubes or CNT-supported initiators. In this process the polymer-CNT nanocomposites can be prepared with high grafting density [11,19].

The "grafting to" approach is based on the attachment of as-prepared or commercially available polymer molecules to the CNT surface by chemical reactions, such as amidation, esterification, radical coupling, etc. The polymer macromolecule must possess adequate reactive functional groups for this approach to work [11,20,21]. This method was used in functionalization of MWCNTs with poly(vinyl alcohol) (PVA) via Fischer esterification reaction. FTIR confirmed the presence of the characteristic peaks of the anticipated ester group. The formation of polymer nanocomposites based on PVA and MWCNTs was confirmed by SEM and TEM. High resolution electron micrographs revealed that the primary binding sites for PVA grafting are the sidewall defects of the nanotubes [22].

In this paper the "grafting to" approach was used to graft maleic anhydride-1-heptene copolymer (MAHP) to oxidized-MWCNTs using hexamethylenediamine (HMDA) bridge. First of all HMDA was added to the oxidized-MWCNTs to form a salt. Then this salt was reacted with MAHP to form a grafted structure. The solubility of the MWCNTs was improved by the functionalization because, grafting MWCNTs to MAHP helps in reducing the nanotube-nanotube adhesion and the tendency to form entangled stacks, which generally make

MWCNTs unusable for manufacturing advanced plastic materials. The obtained material can be a precursor for the manufacturing the advanced plastic composite materials or an additive to construction materials for strengthening purposes.

The novelty of this work is that MAHP macromolecules are attached to oxidized-MWCNT using HMDA bridge via the "grafting to" approach for the first time at room conditions. The long copolymer chains in the resulting material are able to screen and protect the nanotubes from entanglement during dispersion.

2. EXPERIMENTAL
2.1. Materials and methods

All chemicals were of analytical reagent grades. Transmission Electron Microscopy images were taken with a FEI TECNAI G2 20 X–TWIN Transmission Electron Microscope using 200 kV acceleration voltage. The TEM specimens were prepared by dripping the droplets of sonicated solutions of the samples onto carbon coated copper grids. Scanning Electron Microscopy images were recorded using a Hitachi S-4700 SEM instrument operated at 10 kV acceleration voltage in secondary electron imaging mode. Powder XRD patterns were recorded on a Rigaku MiniFlex desktop X–ray diffractometer. X-ray diffraction measurements were performed using Cu K_α radiation (1.5418 Å). FTIR spectra were recorded on a BRUKER Vertex 70 IR spectrometer. Raman investigations were done using Thermo Scientific DXR Raman Microscope using a 532 nm laser for excitation at 10 mW laser power.

2.2. Synthesis and purification of MWCNT

MWCNTs were synthesized by the CVD method. The experimental set-up used for this process consists of a Lenton LTF 14/75/610 type horizontal furnace, a quartz tube and gas flow meters. An Fe-Co/alumina catalyst was used in the process. It was prepared from $Al(OH)_3$, $Fe(NO_3)_3$ x 9 H_2O and $Co(NO_3)_2$ x 6 H_2O and alcohol solvent under ultrasonic agitation. After the catalyst preparation the solvent was evaporated in vacuum and the catalyst was dried in air.

MWCNT synthesis on the catalyst was performed using acetylene (acetylene purity: 3.0 [>=99.9%]) (acetylene flow rate=30 ml/min) as the carbon source and nitrogen (nitrogen flow rate=300 ml/min) as inert gas. In a typical synthesis MWCNT growth was run over 1 gram of catalyst for 2 hours at 650 °C. After the synthesis, the concentration of the catalyst in the raw product powder was 2.8% (according to the EDS results). Therefore it was subjected to purification for removing the remnant catalyst particles from the system. The as-synthesized MWCNT product mixture was mixed with concentrated aqueous HCl solution (36%) and the mixture was boiled under reflux for 16 hours. The product was filtered, washed to pH 7 with deionized water and then boiled under reflux for 16

additional hours in 10 M aqueous NaOH solution. The obtained catalyst-free MWCNT product was then filtered, washed to pH 7 again and dried in air.

2.3. Oxidation of MWCNTs

Since our chosen purification procedure did not involve any oxidizing agents (e.g. nitric acid), it was necessary to add an additional oxidation step to initiate the formation of –COOH functionalities on the MWCNTs surface. Purified MWCNTs were mixed with 0.1 M aqueous $KMnO_4$ solution and stirred at 80 °C for 3 hours. Oxygen bubble formation observable throughout the process confirmed the progress of the reaction. The final product was a mixture of MWCNTs with diverse oxygen-containing functionalities (carboxyl, hydroxyl, aldehyde, anhydride etc.) dominated by –COOH groups.

2.4. Formation of the HMDA salt of oxidized-MWCNT (ox-MWCNT-HMDA).

0.3 g (0.0025 mol) HMDA was added to the 100 ml solvent in a beaker and mixed on a magnetic stirrer for 15 minutes. The solvent used in this process is the mixture of ethanol and water in 3:1 ratio, respectively. Then 0.24 g (0.005 mol) oxidized MWCNTs were added to the solution and homogenized by stirring 15 more minutes. This process is exothermic and does not need the external energy. It proceeds without heating with release of the heat which can be observed with warming of the beaker during the last stage of the process. The beaker was placed into the refrigerator and cooled to temperatures under zero for 30 minutes in order to accelerate the process. Then the product was precipitated, washed and filtered. Scheme 1 represents this process.
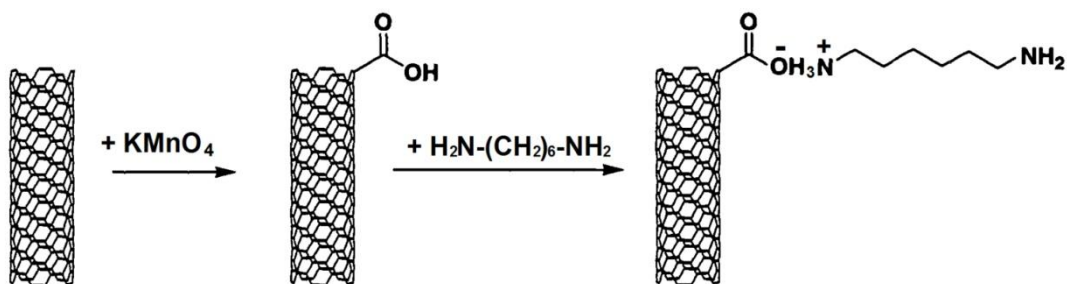
2.5. Grafting of the ox-MWCNT-HMDA to MAHP.

0.024 g MAHP was dissolved in dimethylformamide on a magnetic stirrer. Then 0.04 g ox-MWCNT-HMDA was added to the solution and stirred for 15 minutes. The obtained mixture was washed, filtered and dried. The final product is the MAHP grafted ox-MWCNT-MAHP (ox-MWCNT-HMDA-MAHP). This process proceeds at room conditions because the amine groups easily brakes the anhydride group cycle at room conditions. This process can be visually shown by the scheme 2.
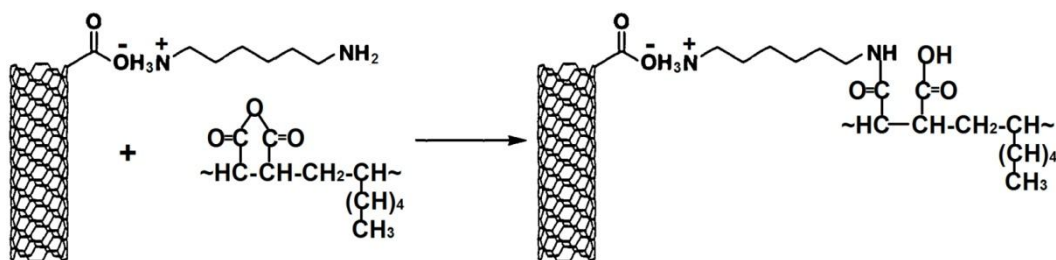
3. RESULTS AND DISCUSSION
3.1. FTIR investigation

FTIR spectra of pristine-MWCNT (a), oxidized-MWCNT (b), ox-MWCNT-HMDA (c) and ox-MWCNT-HMDA-MAHP (d) samples are shown in fig. 1. The aromatic C=C stretching peaks at 1539 cm^{-1}, 1541 cm^{-1} and 1558 cm^{-1} as well as C-C vibrations at 1456 cm^{-1} and 1506 cm^{-1} characterize the pristine MWCNTs [23-25]. The same peaks can be observed in the spectrum of oxidized MWCNT (fig.1b) sample, however, the

Scheme 1. Formation of the ox-MWCNT-HMDA .

Scheme 2. Grafting of the ox-MWCNT-HMDA to maleic anhydride-1-heptene copolymer.
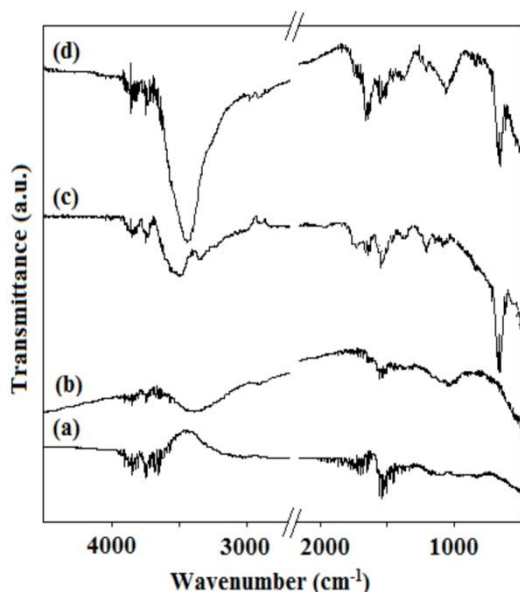

Fig. 1. FTIR spectra of pristine-MWCNT (a), oxidized-MWCNT (b), ox-MWCNT-HMDA (c) and ox-MWCNT-HMDA-MAHP (d) samples.
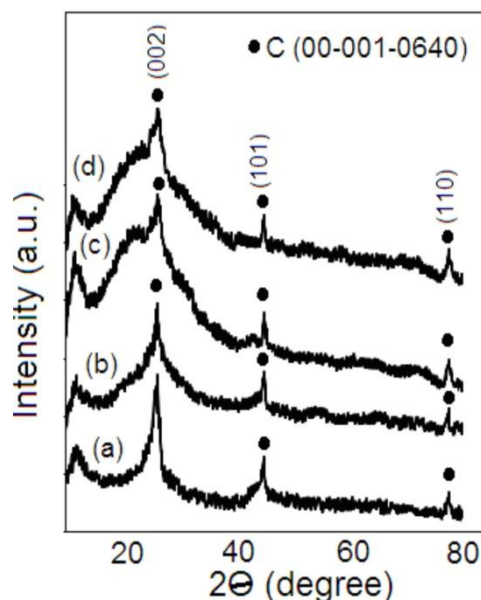

Fig. 2. XRD patterns of pristine-MWCNT (a), oxidized-MWCNT (b), ox-MWCNT-HMDA (c) and ox-MWCNT-HMDA-MAHP (d) samples.

decreased intensities of the C=C peaks at 1539 cm^{-1}, 1541 cm^{-1} and 1558 cm^{-1} indicate defect formation via oxidation. Oxidation is also confirmed by the appearance of the C=O (at 1635 cm^{-1} and 1697 cm^{-1}) and C-O (at 1163 cm^{-1} and 1295 cm^{-1}) bands. The broad band with a maximum at 3381 cm^{-1} can be assigned as the O-H stretching peak of the carboxylic group formed by the oxidative treatment [26].

The spectrum changes considerably upon addition of HMDA and MAHP copolymer addition. The addition of the HMDA causes the appearance of new characteristic peaks of amine groups at 1353 cm^{-1} and 3180-3676 cm^{-1} region. Moreover, the peak at 1525 cm^{-1} assigned to zwitterions also appears with this addition (fig. 1c). We can see the peak of Amine groups at 1359 cm^{-1} and the

peak of the zwitterions at 1525 cm^{-1} even after the addition of the MAHP copolymer to the system. In addition to these peaks the peak at 1643 cm^{-1} is appeared which can be assigned to N-H bend of amide groups (fig. 1d). The broad peak at 3055-3676 cm^{-1} region is the asymmetric and symmetric (associated) N-H stretching. This peak is the mixed peak of amide and amine groups [27,28].

3.2. XRD

Fig. 2 shows the X-ray diffraction patterns of pristine-MWCNT (a), oxidized-MWCNT (b), ox-MWCNT-HMDA (c) and ox-MWCNT-HMDA-MAHP

(d) samples. The peaks at 26.34°, 44.82° and 77.58° can be assigned to reflections from the (002), (101) and (110) crystallographic planes of multiwall carbon nanotubes, respectively (PDF no: 00-001-0640). These peaks are observable in the patterns of the other three samples as well. However, slight differences in peak widths and intensities indicate that the oxidation and functionalization processes have affected the ordering of the graphitic layers to some extent.

The average coherence length (L_c) or mean crystalline size along the c-axis (the crystallographic c-axis is the one perpendicular to the long axis of the MWCNTs) was estimated by the Scherrer`s formula [29]:

$$L_{hkl} = (0.9 \times \lambda)/(\beta \times cos\theta)$$

where λ corresponds to the X-ray wavelength, θ is the Bragg angle and β is the half-peak width in radians. The (002) Bragg peak was used to calculate L_c. The results were about 10.5 nm (pristine-MWCNT), 6.2 nm (oxidized-MWCNT), 3.4 nm (ox-MWCNT-HMDA) and 2.9 nm (ox-MWCNT-HMDA-MAHP). These values represent an average stacking height of graphitic planes in the MWCNT walls. It can be seen from the results that the value of L_c decreases from pristine MWCNT to ox-MWCNT-HMDA-MAHP. The reason behind this is that oxidation by $KMnO_4$ results in the partial loss of the outermost graphitic layers and the introduction of defects, which reduce the symmetry of the plane. Binding the HMDA and MAHP molecules to the defects amplifies this effect, resulting in the further reduction of the L_c value.

3.3. Raman spectroscopy

Raman spectra of pristine-MWCNT (1), oxidized-MWCNT (2), ox-MWCNT-HMDA (3) and ox-MWCNT-HMDA-MAHP (4) samples are depicted in fig. 3. The Raman spectrum of MWCNTs contains 3 major peaks: the D band, G band and G` band [30]. The D band which is observed at ~1342 cm^{-1} is a disorder induced peak corresponding to scattering from defects and amorphous carbon impurities present in the MWCNTs samples. The G band peak (~1579 cm^{-1}) is the result of ordered high-frequency in-plane stretching of the C-C bonds. The G` band (~2682 cm^{-1}) is the result of double resonance process. This band does not require an elastic defect-related scattering process and is observable also for defect-free sp^2 carbons. The ratio between the intensities of D and G bands (I_D/I_G) is proportional with the extent of defect concentration, thus it can be used to quantify oxidation and functionalization. As it can be seen from fig. 3, the I_D/I_G ratios for pristine MWCNTs, oxidized MWCNTs, ox-MWCNT-HMDA and ox-MWCNT-HMDA-MAHP are 0.86, 0.95, 0.87 and 0.72 respectively. An increase in the I_D/I_G ratio indicates an increase in the number of defects on the sidewalls of MWCNTs. These values suggest that while oxidation has increased the number of sidewall defects in the MWCNTs to some extent, the subsequent grafting steps did not alter the sp3/sp2 carbon ratio of the oxidized nanotube wall structure any further.

3.4. Microscopic investigations
3.4.1. TEM investigation

Fig. 4 shows the TEM images of pristine-MWCNT (a), oxidized-MWCNT (b), ox-MWCNT-HMDA (c) and ox-MWCNT-HMDA-MAHP (d) samples.

These micrographs are evidences of the completion of "grafting to" process. Pristine MWCNTs (fig. 4a) are more TEM-transparent than oxidized (fig. 4b) and grafted ones (fig. 4d). This is because the sidewalls of pristine-MWCNTs are smooth, whereas the oxidized and defected walls visible in fig. 4b-d have more electron scattering power. The outer layers of the sidewalls of these MWCNTs are exfoliated due to the strong oxidation effect of oxidation agent and have changed their shape partly to a graphene-like structure (fig. 4b). The average diameter of the pristine-MWCNTs is 16.5 ± 2.5 nm according to the fig. 4a. After the purification and oxidation processes (fig. 4b) the exfoliation of the outer layers of the MWCNTs changes the apparent diameter of the tubes to 19.8 ± 1.7 nm. The exfoliation of the outer layers of the tubes can be easily seen in fig. 4b. But the fig. 4d shows different view. In this picture the MWCNTs are arranged in ordered manner and covered by thin polymeric layers which can be seen as the shadows on the tubes. The average thickness of the copolymer cover layer is 7.8 ± 1.4 nm.

3.4.2. SEM investigation

Characteristic SEM micrographs of pristine-MWCNT (a), oxidized-MWCNT (b), ox-MWCNT-HMDA (c) and ox-MWCNT-HMDA-MAHP (d) samples
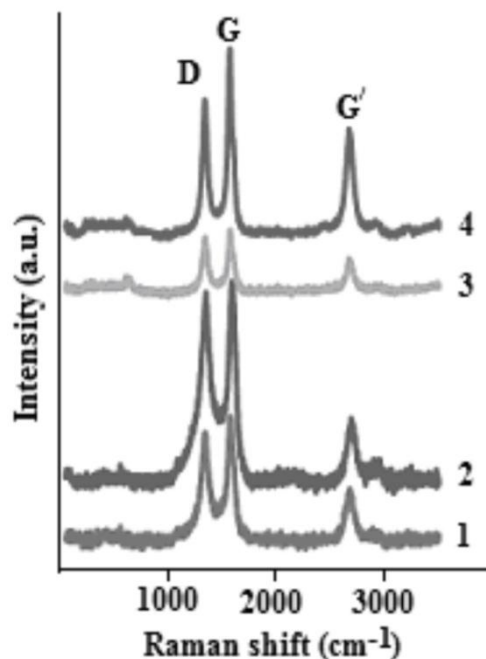

Fig. 3. Raman spectra of pristine-MWCNT (1), oxidized-MWCNT (2), ox-MWCNT-HMDA (3) and ox-MWCNT-HMDA-MAHP (4)
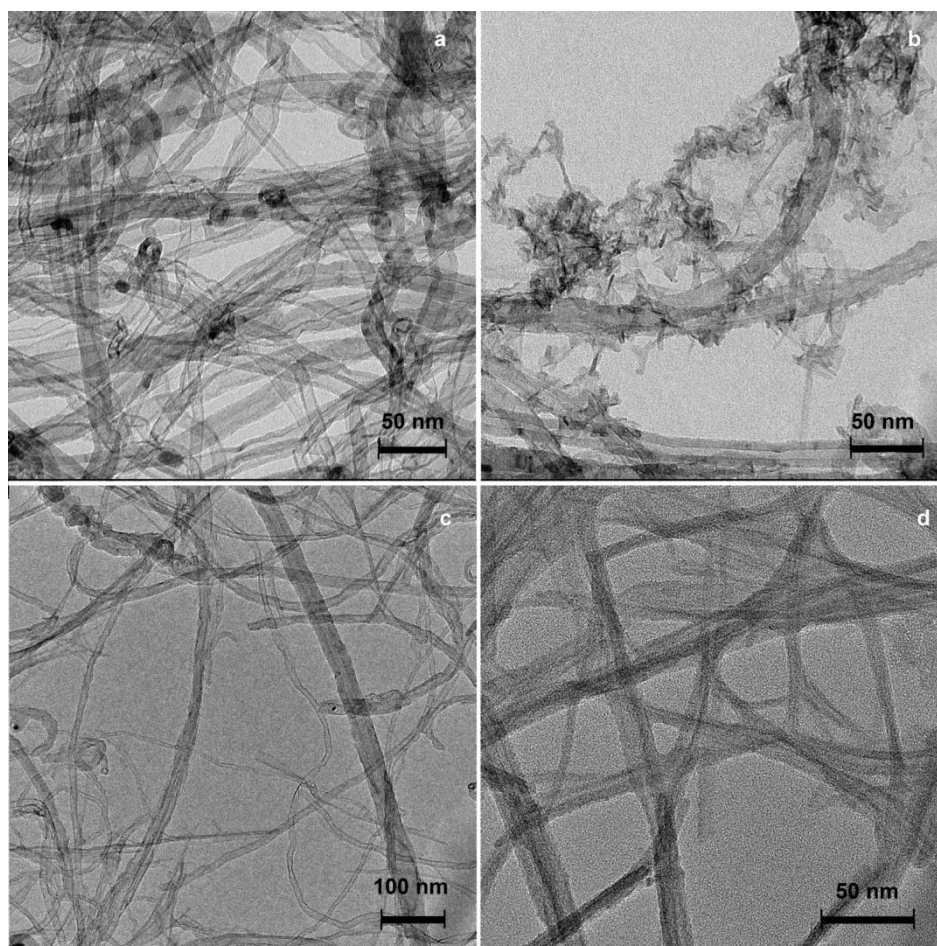
Fig. 4. TEM images of pristine-MWCNT (a), oxidized-MWCNT (b), ox-MWCNT-HMDA (c) and ox-MWCNT-HMDA-MAHP (d)
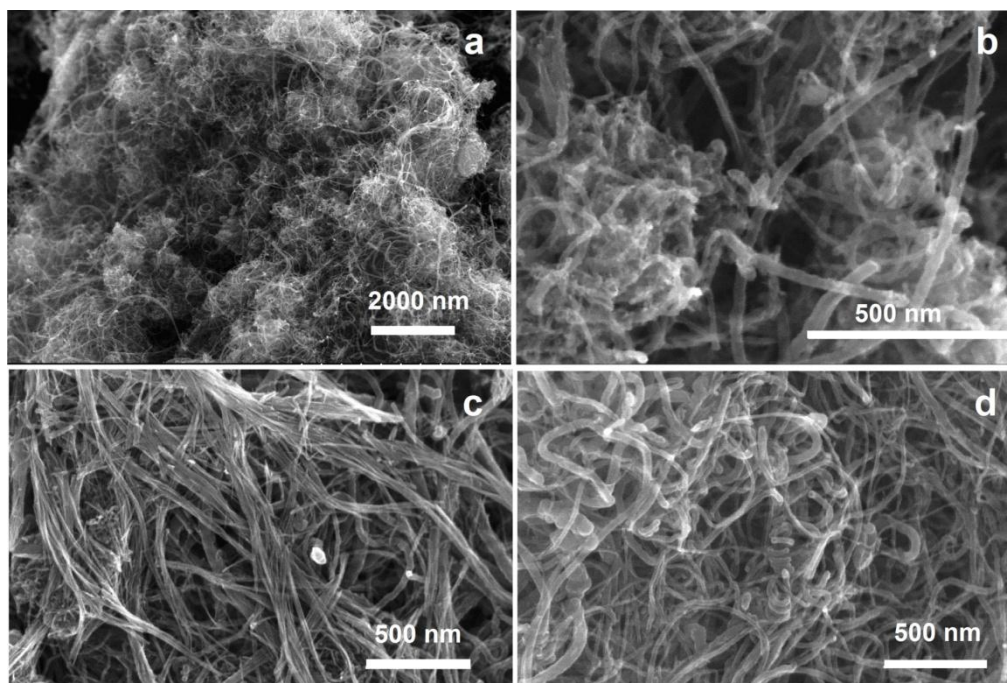

Fig. 5. SEM images of pristine-MWCNT (a), oxidized-MWCNT (b), ox-MWCNT-HMDA (c) and ox-MWCNT-HMDA-MAHP (d)

are depicted in fig. 5. The unmodified, smooth surface of pristine MWCNTs visible in fig. 5a confirms the TEM-

derived diameter estimation. In contrast, the surface of the oxidized-MWCNTs looks rough because of the defected regions created by oxidation (fig. 5b). The image of the intermediate ox-MWCNT-HMDA sample also shows the visible defects (fig. 5c). The polymer coating of the tubes can be observed in fig. 5d. The maleic anhydride–1-heptene copolymer macromolecules were attached to the defect-activated regions of the MWCNTs by the "grafting to" method using HMDA bridge and cover the whole nanotube surface. This is the surface polymer layer that keeps CNTs apart, makes them soluble in hydrophilic solvents and prevents their entanglement and agglomeration.

4. CONCLUSION

Multiwall carbon nanotubes synthesized by CVD from acetylene over an Fe,Co/alumina catalyst were oxidized by $KMnO_4$ solution to form functionalities on wall defects and end caps. The oxidized MWCNTs were grafted with maleic anhydride-1-heptene copolymer via the "grafting to" approach using hexamethylenediamine bridge. The proof of completion of the "grafting to" process was obtained by XRD, Raman and FTIR methods. FTIR also confirmed the presence of the characteristic peaks of the anticipated zwitterion and amine-amide conversion. TEM and SEM revealed that the nanotubes are uniformly covered with the polymer which shows the effectiveness of the method. The suggested process was carried out at room conditions and therefore it can be considered as a feasible alternative for carbon nanotube functionalization targeted at polymer composite applications.

_____

[1] *X. Wang, Q. Li, J. Xie, Z. Jin, J. Wang, Y. Li, K. Jiang, S.S. Fan.* Nano Lett 9 (9) (2009) 3137–3141.

[2] *M. Paradise, T. Goswami.* Mater Des 28 (2007) 1477-1489.

[3] *R. Johnson.* CVD process tames carbon nanotube growth, EE Times, 2002.

[4] *M. Gulas, C.S. Cojocaru, C.T. Fleaca, S. Farhat, P. Veis, F.L. Normand.* Eur Phys J Appl Phys 43 (2008) 353-356.

[5] *C.D. Scott, S. Arepalli, P. Nikolaev, R.E. Smalley.* Appl Phys A 74 (11) (2002) 573-580.

[6] *M.M.A. Rafique, J. Iqbal.* J Encapsul Adsorpt Sci 1 (2011) 29-34.

[7] *E.T. Thostenson, Z.F. Ren, T-W. Chou.* Compos Sci Technol 61 (2001) 1899-1912.

[8] *A.A. Hosseini, M. Allahyari, S.D. Besheli.* Int J Sci Environ Tech 1 (3) (2012) 217-229.

[9] *M. Kumar, Y. Ando.* J Nanosci Nanotechno 10 (2010) 3739-3758.

[10] *A. Hirsch.* Angew Chem Int Ed 41 (2002) 1853-1859.

[11] *N.G. Sahoo, S. Rana, J.W. Cho, L. Li, S.H. Chan.* Prog Polym Sci 35 (2010) 837-867.

[12] *J. Liu, A.G. Rinzler, H. Dai, J.H. Hafner, R.K. Bradley, P.J. Boul, A. Lu, T. Iverson, K. Shelimov, C.B. Huffman, F. Rodriguez-Macias, Y.S. Shon, T.R. Lee, D.T. Colbert, R.E. Smalley.* Science 280 (1998) 1253-1256.

[13] *X. Zhang, T.V. Sreekumar, T. Liu, S. Kumar.* J Phys Chem B 108 (2004) 16435-16440.

[14] *V. Georgakilas, K. Kordatos, M. Prato, D.M. Guldi, M. Holzinger, A. Hirsch.* J Am Chem Soc 124 (2002) 760-761.

[15] *S. Niyogi, M.A. Hamon, H. Hu, B. Zhao, P. Bhowmik, R. Sen, M.E. Itkis, R.C. Haddon.* Acc Chem Res 35 (2002) 1105-1113.

[16] *O. Zhou, R.M. Fleming, D.W. Murphy, C.H. Chen, R.C. Haddon, A.P. Ramirez, S.H. Glarum.* Science 263 (1994) 1744-1747.

[17] *J.B. Baek, C.B. Lyons, L.S. Tan.* Macromolecules 37 (2004) 8278-8285.

[18] *Z. Jin, X. Sun, G. Xu, S.H. Goh, W. Ji.* Chem Phys Lett 318 (2000) 505-510.

[19] *E.Y. Malikov, M.C. Altay, M.B. Muradov, O.H. Akperov, G.M. Eyvazova, R. Puskás, D. Madarász, Á. Kukovecz, Z. Kónya.* Physica E 69 (2015) 212-218.

[20] *K. Fu, W. Huang, Y. Lin, L.A. Riddle, D.L. Carroll, Y.P. Sun.* Nano Lett 1 (2001) 439-441.

[21] *S. Qin, D. Qin, W.T. Ford, D.E. Resasco, J.E. Herrera.* Macromolecules 37 (2004) 752-757.

[22] *E.Y. Malikov, M.B. Muradov, O.H. Akperov, G.M. Eyvazova, R. Puskás, D. Madarász, L. Nagy, Á. Kukovecz, Z. Kónya.* Physica E 61 (2014) 129-134.

[23] *A. Misra, P.K. Tyagi, M.K. Singh, D.S. Misra.* Diam Relat Mater 15 (2-3) (2006) 385-388.

[24] *Y. Rike, O. Holia, Sudirman, S. Yukie, I. Tadahisa, A. Jun-ichi.* Open Mater Sci J 5 (2011) 242-247.

[25] *M. Vesali Naseh, A.A. Khodadadi, Y. Mortazavi, O. Alizadeh Sahraei, F. Pourfayaz, S. Mosadegh Sedghi.* Int J Chem Biol Eng 2 (2) (2009) 66-68.

[26] *F.A. Abuilaiwi, T. Laoui, M. Al-Harthi, M.A. Atieh.* Arab J Sci Eng 35 (1C) (2010) 37-48.

[27] *G.M.O. Barra, J.S. Crespo, J.R. Bertolino, V. Soldi, A.T.N. Pires.* J Braz Chem Soc 10 (1) (1999) 31-34.

[28] *J.B. Lambert.* Introduction to organic spectroscopy. Macmillan, New York, 1987.

[29] *G. Maurin, I. Stepanek, P. Bernier, J.F. Colomer, J.B. Nagy, F. Henn.* Carbon 39 (2001) 1273-1278.

[30] *M.S. Dresselhaus, J. Ado, M. Hofman, G. Dresselhaus, R. Saito.* Nano Lett 10 (3) (2010) 751-758.

ELECTRON-CONFORMATIONAL PROPERTIES AND MOLECULAR DYNAMICS OF THE CREKA MOLECULE

G.D. ABBASOVA, E.Z. ALIYEV

Baku State University, Az-1148, Z. Khalilov str., 23

The spatial and electron structure of CREKA molecule, the new drug with antitumor activity was investigated by the methods of theoretical conformational analysis, quantum chemistry and molecular dynamics. The geometrical parameters and energy contributions of various types of interatomic interactions in stabilization of the molecule stable conformations are calculated, the quantitative evaluation of the change limits of dihedral angles in main and side chains of amino-acid residuals is carried out. The electron and conformational properties of CREKA molecule are studied by semi-empirical methods of quantum chemistry CNDO/2 and MNDO using AM1 and PM3 calculation schemes. The comparative analyze of the calculation results carried out by the different methods is done.

Keywords: CREKA, peptide, conformational analysis, electron structure, molecular dynamics.
PACS: 31.15; 33.15

INTRODUCTION

The investigation of processes of controlled transport of drugs and diagnostic agents realized with the help of nano-particles is the one of actual directions of nano-bio-technology. The nano-particles loaded by drug molecules, are able to deliver the chemical compounds directly to injured cells without essential influence on healthy ones of different organs and tissues. In spite of the fact that the more than thirty thousands of different drugs are registered in the world, the search of compounds having the clearly expressed selective action effect has been continued up to nowadays. The new compounds are synthesized and their modified analogues are investigated. The compound consisting on five amino-acid residuals Cys, Arg, Glu, Lys, Ala and called CREKA is related to number of such drugs applied in antitumor therapy with the use of nano-particles. CREKA drug having the antitumoral effect at prostate cancer had been firstly synthesized in 2006 by American scientists [1]. Later, its pharmacological properties had been investigated [2-7]. However, the numerical biological tests are carried out without knowing of its space structure, conformational mobility and electron properties necessary for revealing of molecular bases of drug action mechanism and intentional search of more effective analogues of CREKA molecule.

The geometric and energy parameters defining the molecule stable conformational states are calculated by theoretic methods with use of computing programs in the present work with the aim of reporting on conformational mobility and electron-conformational properties of CREKA molecule.

CALCULATION METHODS

The low-energy conformational states of CREKA molecules are found by method of theoretical conformational analysis in approximation of atom mechanic model by technique described in detail in [8]. The potential function parameters used in present work describing the different types of atom-atom interactions: electrostatic, non-valent (including hydrogen bonds forming with participation of hydrogen atom of functional groups OH, -NH and SH and oxygen heteroatom) and torsion potentials are taken from [8]. The calculations are carried out for conditions modeling the water surrounding and dielectric constant value is taken equal to 10.

Electron structure of CREKA molecule is investigated by semi-empirical methods of quantum chemistry CNDO/2 and MNDO with the use of parameterized calculation schemes AM1 and PM3.

The demonstrated version of **HyperChem 7.5** program of site of corporation **Hypercube** (http://www.hyper.com/) is used for calculation. The equilibrium nuclear configurations corresponding to geometry of low-energy conformations calculated by method of theoretical conformational analysis are taken in the capacity of zero approximations at optimization of molecule electron energy. It is known that these semi-empirical methods decrease the barrier value of peptide bond rotation that's why the structure correction by molecular dynamics method is carried out before calculation beginning.

The calculations by molecular dynamics method are carried out under conditions of implicit water molecules with medium dielectric constant (ε) under consideration. It is known that change of dielectric constant influences on balance of functional groups of amino-acid residuals in peptide molecules and essentially influences on formation of hydrogen bonds and its number. In all cases, the calculated equilibrium geometry is used in the capacity of initial one for molecular-dynamic calculation carried out in potentials of semi-empirical method MM+ without taking into consideration the symmetry. The optimization of molecule geometry is carried out with convergence parameter 0.01.

RESULTS AND DISCUSSION

The stable conformational states of CREKA molecule are obtained on the base of stage-by-stage approach including the calculation of fragment low-energy states according to scheme given in fig.1. The acceptable values of dihedral angles in main and side chains of amino-acid residuals including in CREKA molecule composition are used in the capacity of zero approximations. 800 starting conformations included in

procedure of minimization of total conformation energy being the additive sum of energy depositions of non-valent, electrostatic, torsion interactions and energy of hydrogen bond formation, are chosen.
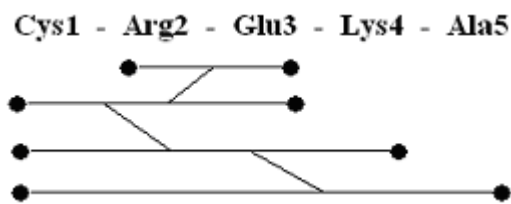

Fig.1. The scheme of step-by-step calculation of CREKA molecule.

The calculation results are generalized in tables 1-3 and in fig.2 where the low-energy conformational states of CREKA molecule are given. According to investigation results, the peptide molecule can realize 12 stable conformational states divided by not high potential barrier. The conformations with both unfolded form of main chain (conformations 1,5-11, fig.2) and conformation with folded form of peptide frame (conformations 2-4 and 12, fig.2) are related to them. The conformation 3, in which the distance between C^α-atoms of first and last residuals is minimum one and it is equal to 4.5Å, is the more compact one. The tail residuals in 3,4 and 12 conformations (table 1) are space-conciliated. The difference in conformational energy value of calculated structures doesn't exceed 3,4 kcal/mol (table 1), i.e. the molecule is conformationally mobile and the choice of concrete structure will depend on real surrounding of peptide molecule. The interactions of valence-unbound atoms make the main stabilizing contribution into energy of calculated structures. The destabilizing contribution of electric interactions varies in limits 2.6÷8.4 kcal/mol.

Table 1.

The contributions of different interaction types in low-energy conformation CREKA molecule (kcal/mol).

Conformation	E_{nv}	E_{el}	E_{tors}	E_{tot}	E_{rel}	Distance between C^α-atoms of Cys1 and Ala5 (Å) residuals
1	-16.0	2.8	1.9	-11.3	0.0	11.1
2	-17.4	4.8	2.5	-10.0	0.3	9.5
3	-17.1	4.1	2.0	-10.9	0.3	4.5
4	-16.5	2.6	3.1	-10.7	0.5	6.0
5	-15.6	2.9	2.3	-10.4	0.9	6.1
6	-19.8	7.4	2.2	-10.2	1.0	12.3
7	-18.6	5.6	2.7	-10.2	1.1	8.5
8	-20.5	8.4	2.1	-10.0	1.2	11.4
9	-14.8	2.8	2.0	-9.8	1.5	11.3
10	-17.4	6.3	2.6	-8.5	2.8	11.0
11	-17.9	7.7	1.9	-8.4	2.2	12.2
12	-15.6	4.3	3.4	-7.8	3.4	6.4

Table 2.

Hydrogen bonds in low-energy conformations of CREKA molecule.

*Conformation	Hydrogen bond	Hydrogen bond length, Å	Hydrogen bond energy, kcal/mol
1	$N^\delta H(Arg2)…COO(Glu3)$	2.7	-0.18
2	NH (Glu3)…COO(Glu3) CO(Glu3)…NH(Ala5)	2.5 2.7	-0.34 -0.18
3	$N^\delta H(Arg2)…COO(Glu3)$	2.3	-0.54
4	$N^\delta H(Arg2)…COO(Glu3)$	2.9	-0.11
5	$N^\delta H(Arg2)…COO(Glu3)$	2.8	-0.15
6	NH(Cys1)…COO(Glu3) NH(Arg2)…COO(Glu3)	1.9 2.2	-1.25 -0.76
7	NH(Cys1)…COO(Glu3)	2.1	-1.05
8	NH(Cys1)…COO(Glu3) NH(Arg2)…COO(Glu3)	2.1 2.0	-1.05 -0.94
9	$N^\delta H(Arg2)…COO(Glu3)$	2.4	-0.42
11	NH(Arg2)…COO(Glu3)	2.3	-0.50

*Note: Conformation numbers correspond to table 1.

Table 3.

Dihedral angles in low-energy conformations of CREKA molecule on data of conformational analysis.

Conformation	Amino-acid residuals				
	Cys1	Arg2	Glu3	Lys4	Ala5
1	-73,-55,180,176	-104,-59,178,177,185,176,181	-99,137,185,-54,-69,166	-117,-61,181,-61,179,179,179,180	-88,-52,178,180
2	-76,-52,180,179	-92,-56,178,178,182,178,181	-147,173,180,43,60,67	-90,95,180,-60,181,181,181,180	-84,-55,179,180
3	-83,72,181,178	-116,-63,177,175,187,171,180	-96,-52,183,-55,-66,154	-114,123,175,180,179,180,180,180	-83,-54,180,181
4	-83,76,181,180	-119,-63,179,179,185,177,181	-94,140,187,-56,-70,167	54,65,184,-57,179,181,180,180	50,56,188,-59
5	-77,-57,179,176	-108,-61,178,177,183,177,181	-98,143,186,-55,-70,168	55,68,181,-57,180,180,180,180	-113,141,183,61
6	-87,-62,180,-57	-136,-63,180,-67,179,182,179	53,62,183,-60,75,228	-117,96,182,-57,179,182,180,180	-89,-56,180,180
7	-88,-63,180,-62	-137,-62,180,-72,181,180,180	53,68,183,-61,74,230	60,68,183,-54,179,181,179,180	-111,141,177,59
8	-89,-62,180,-63	-138,-63,179,-67,179,182,179	53,59,183,-60,74,234	-113,-61,182,-58,179,182,180,180	-86,-54,179,180
9	-82,179,181,85	-105,-62,179,176,186,174,181	-98,139,188,-56,-68,163	-116,-60,181,-59,179,180,180,180	-87,-52,178,180
10	-79,181,181,84	-103,101,181,-61,179,180,179	-107,167,189,-51,-56,124	-83,-53,177,-60,179,181,179,180	-83,-53,176,180
11	-79,180,181,83	-113,-62,180,-60,178,182,178	50,62,179,-62,72,234	-120,94,181,-120,-57,179,182,180	-89,-56,180,180
12	-80,-58,180,-58	-113,-58,178,183,183,179,180	-104,-74,190,-57,-71,173	-128,-68,193,-60,180,180,180,180	-89,-51,189,-51

*Note: The values of dihedral angles are given in consistency: φ, ψ, ω (main chain, upper line), χ_1, χ_2, χ_3, χ_4, χ_5 (side chain, low line).

The low-energy conformation are stabilized by hydrogen bonds in formation of which the side chains of residuals with opposite charged functional groups Arg2 and Glu3 (table 2) take part. The hydrogen atoms of peptide groups (NH) of main chain Cys1, carboxyl group of side chain of glutaminic acid (Glu3) and atoms of peptide group in main chains of Glu3 and Ala5 residuals also take part in formation of hydrogen bonds.

According to calculation results, glutaminic acid plays the essential role in formation of stabilizing contacts as takes part in both non-valent interactions and electrostatic contacts with neighboring residuals in chains. The values of dihedral angles of 12 low-energy conformational states of CREKA molecule, which can be used for study of its structure analogs and conformational dynamics.

CALCULATION OF ELECTRON STRUCTURE OF CREKA MOLECULE

The electron structure of CREKA molecule is investigated with the help of semi-empirical quantum-chemical methods CNDO/2 and MNDO with use of parameterized calculation schemes AM1 and PM3 widely developed and well enough approved at investigations of electron-conformational properties of biological molecules. The wide choice of quantum-chemical methods based on different approximations is caused by necessity of objective analysis of obtained results. The revealing of general elements of spatial and electron structures of CREKA molecule supposedly responsible for unique pharmacological effects of investigated compound is the aim of such investigations.

At calculation of parameters defining the electron structure of peptide molecule the atom coordinates belong to equilibrium nuclear configurations in twelve low-energy conformational states of molecule calculated by method of conformational analysis (tables 1 and 3) are used. In all methods only the atom orbitals with principal quantum number corresponding to highest orbitals of isolated atoms populated by electrons and valent electrons are taken into consideration. The equation solution of self-consistent field with convergence parameter 10^{-8} can be obtained at maximum number of cycles, which is not more than 500.
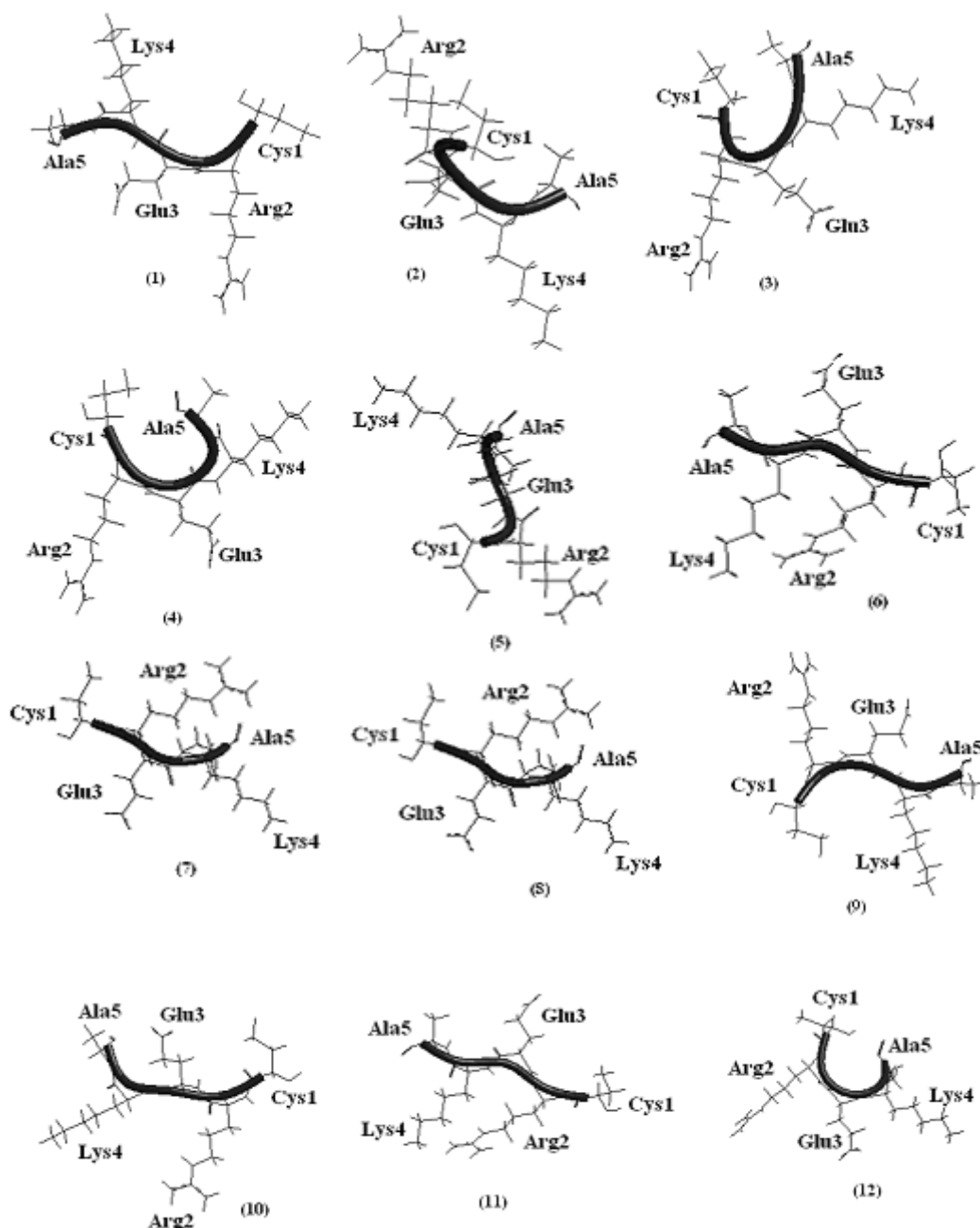
Fig. 2. Low-energy conformation states of CREKA molecule on data of theoretic conformational analysis.

The difference of total energy on previous and following iteration step is the main parameter of convergence criterion.

The least activation energy value of nuclear repulsion is realized in structure 1, table 1. Such clear correspondence isn't observed for electron energy. As it is seen from table 4 the state with energy global minimum (conformation 1, table 1) dominates in comparison with total electron energy values. The lowest value of total electron energy is caused by well energy balance of electron cloud stabilization and repulsion of atom residuals. In spite of the fact that electron energy value of this structure is less than other configuration ones. The faborable localization of atom nuclears compensates this fact. Finally, conformation 1 has the biggest bond energy value, which is the main criterion of stability. The following four conformations with relative energy

0.3-0.9 kcal/mol on bond energy value are lower than conformation 1 as inter-frame repulsions increase more essentially than stabilizing electron contributions. The most value of electron energy is observed in conformation 7, which is also characterized by more strong repulsion of atom frames. The opposite picture is revealed for conformation 9, in which the minimum value of nuclear repulsion energy is compensated by most value of molecule electron energy. Thus, one can conclude that between conformations being in the relative energy interval 0-5 kcal/mol the essential divergence of differentiation character of low-energy states isn't observed at calculations of molecular mechanics and CNDO/2 method. In spite of the difference in absolute value of calculated parameters of electron structure, the analogous picture is observed for other quantum-chemical calculation methods.

_____

[1] *O.C. Farokhzad, J.J. Cheng, B.A. Teply, I. Sherifi, S. Jon, P.W. Kantoff, J.P. Ritchie, R. Langer.* 2006. Targeted nanoparticles–aptamer bioconjugates for cancer chemotherapy in vivo. *Proc. Nat. Acad. Sci.* **103,** 6315-6320.

[2] *A. Fleischmann, U. Laderach, H. Friess, M.W. Buechler, J.C. Reubi.* 2000. Bombensin receptors in distinct tissue compartments of human pancreatic diseases. *Laboratory Investigation*, **80**, 1807-1817.

[3] *X. Montet, R. Weissleder, L. Josephson.* 2006. Imaging pancreatic cancer with a peptide–nanoparticle conjugate targeted to normal pancreas. *Bioconjugate Chemistry*. **17**, 905-911.

[4] *P. Couvreur, C. Vauthier.* Nanotechnology: intelligent design to treat complex disease. Pharm.Res., 2006. **23** (7), 1417-1450.

[5] *C.J. Sunderland, M. Steiert, J.E. Talmadge, A.M. Derfus, S.E. Barry.* Targeted nanoparticles for detecting and treating cancer. Drug Development Res.**7**, 2006.70-93.

[6] *T.C. Yih, M. Al-Fandi.* Journal of Cellular Biochemistry. **97**, 2006. 184-1190.

[7] *D. Simberg, T. Duza, J.H. Park, M. Essler, J. Pilch, L. Zhang, A.M. Derfus, M. Yang, R.M. Hoffman, S. Bhatia, M.J. Sailor, E. Ruoslahti.* 2007.Biomimetic amplification of nanoparticle homing to tumors. *PNAS*. **104** (3), 932-936.

[8] *F.A. Momany, R.F. McGuire, A.W. Burgess, H.A. Scheraga*. Energy parameters in polypeptides: Geometric parameters, partial atomic charges, non-bonded interaction for naturally occuring amino acid. *Phys. Chem.*, 1975, **79,** 2361-2381.

CONTENTS